



Norwegian University of
Science and Technology

Control System for ROV Minerva 2

Erik Bjørklund Holven

Marine Technology

Submission date: June 2018

Supervisor: Martin Ludvigsen, IMT

Norwegian University of Science and Technology
Department of Marine Technology



Norwegian University of
Science and Technology

Master thesis in Marine Subsea Engineering
Spring 2016
for
Stud.Tech **Erik Bjørklund Holven**

Title: Control System for ROV Minerva II
Kontrollsystem for ROV Minerva II

Work Description

Remotely Operated Vehicles (ROV) are used gradually more, and for more complex operations. By applying motion control system for these vessels a better performance can be obtained, resulting in missions with higher accuracy and that are less time and energy consuming and will result in safer underwater operations. The main goal of the thesis is to develop the ROV control system to a state where it can be used on the ROV Minerva 2. This will be done by developing the controller and thrust allocator for the new ROV system. In addition to this smaller modifications will be made to the existing control system and simulator, so that they can be used for the ROV Minerva 2. High performing motion control systems are based on an accurate mathematical model of the system. To establish an accurate mathematical model of Minerva 2 an analysis will be performed to identify the hydrodynamics parameters of the ROV. This thesis will also explore the feasibility of applying system identification as a tool to calculate the mathematical model of the ROV.

Supervisor: Martin Ludvigsen

Preface

This thesis is based on a project carried out during the spring 2018. The project considered the Development of a control system for the ROV Minerva 2, and the work is carried out at the department of Marine Technology at the Norwegian University of Science and Technology. The main topics of this thesis is the control system, and also a hydrodynamic analysis of the ROV. Part of this master thesis is directly based on the work that was done in a preparation project during the autumn of 2017. It is assumed that the reader of this thesis will have fundamental knowledge of marine engineering and control systems.

Acknowledgment

In the work on this thesis I have received good help, inspiration and input from my supervisor Professor Martin Ludvisgen. He have provided great feedback and ideas for the development of the control system, and for this i would like to thank him. I would also like to thank Ph.D candidate Stein M. Nornes. During the work on the control system he have been the person in charge of the ROV control system. He have both been providing invaluable input, and helped resolved technical challenges. Furthermore he have also directly contributed by developing the software. Without the guidance and input from him, this thesis would not have been possible.

I would also like to thank the Ph.D candidates Øystein Sture and Ole A. Eidsvik. They have both provided ideas, input and tips to how challenges could be solved. For the experimental test performed in this thesis assistance and guidance were received from Torgeir Wahl. I would like to thank him for this help. In addition to this huge thank is directed to Ole-Erik Vinje and Marcus Almehagen who created parts of the mounting rig, and helped set up the experiment. The model of the ROV was created by the technicians at the workshop at the department. I would like to thank Kristian Minde and Niklas J. Hall for their work on creating the scale model of the ROV.

In addition to this three fellow master students have been working on the same topic of the ROV control system, but with a different task. We have had several joint tests, and many meetings together where ideas on how the ROV control system can be formed have been discussed. They have also provided help and supported me during the work on my master thesis. I would like to thank Einar N. Agdestein, Tsz K. Chiu and Libo Xue for this. I would also like to thank my fellow students at marine technology with. Together we have discussed our theses, and supported and motivated each other. I would like to extend my greatest gratitude to my fellow students and friends at marine technology.

Trondheim, June 18, 2018



Erik Bjørklund Holven

Abstract

This thesis cover the development of the motion control system for a Remotely Operated Vehicle (ROV). The Norwegian University of Science and Technology are receiving a new ROV, Minerva 2, which is the topic of this thesis. Three aspects of the ROV system is focused on in this thesis. This is: the mathematical modelling of the vessel, the control system of the ROV, and an evaluation of the feasibility of applying system identification to the ROV is considered.

The mathematical model of the ROV is derived by considering a 6 Degree Of Freedom(DOF) model for a marine vessel. The rigid body motion can be derived on the basis of the mass properties of the ROV. The hydrodynamic parameters have been established for the ROV, to account for the effect of the ROV being submerged in water. This is done by applying computational tools. The added mass is determined by using a tool based on potential theory and radiation and diffraction methodology. The damping on the ROV will be dominated by viscous effect, that are neglected in potential theory. For this reason Computational Fluid Dynamics (CFD) is applied to a model of the ROV, to determine the damping coefficients. The result was verified by considering a simple geometry reference object that was analysed both with computational tools and with empirical estimated. The result for the added mass gave results that are in accordance with expectations. For the damping, the linear term seem to have been underestimate, while the quadratic term of the damping function might be too large. An experimental test was designed to test a scale model of the ROV, and estimate the hydrodynamic parameters of the ROV experimentally. Problems in the experiment related to the sensor alignment and motions on the mounting bracket made introduced inaccuracies in the measurement. The calculated damping was found to be in the same order of magnitude as for the CFD analysis. Due to inaccuracies in the measurements, the quality of the data was not sufficiently good for the added mass to be calculated.

The control system is based on an existing control system developed for the former ROV's at NTNU. Since the new ROV is controlled in 6 DOF's, compared to 4 for the old ROV's, the controller have been expanded to account for roll and pitch motion. Minerva 2 is also an over actuated ROV, meaning that there are more thrusters than DOF's. This result in a system where there are infinitely many combinations of thruster speeds that can result in one desired output. A new thrust allocator was developed to determine the optimal combination of the thruster speeds corresponding to a desired output. This was done by defining an optimisation target of minimizing the total propulsion energy, and solving the thrust allocation problem as an optimisation problem. A secondary objective for the thrust allocator was to limit water from being flushed in front of the cameras, when it was possible to avoid it.

This was achieved by giving energy associated to thrust causing water to be flushed in front of the ROV a large weight. Development have also been made in the autonomy part of the control system. The purpose of this was to allow for separate programs performing sonar and camera tracking, to relay this information to the autonomy system in form of way points. This was tested with a virtual integration of the ROV control system, in a simulation of an inspection mission.

A system identification function have also been evaluated. This involves calculating the mathematical model of the vessel based on the response of the ROV, i.e the motion of the ROV, and the control input. Both simple simulations and simulations using Hardware In the Loop (HIL) simulators was used to evaluate the feasibility of such a system. The result of these simulation showed promising result. These test show that with a sufficiently large sample of measurement, the system identification is able to create a mathematical model of the system, with a high level of accuracy.

Sammen drag

Denne oppgaven dekker utviklingen av bevegelseskontrollsystemet for et fjernstyrt undervanns fartøy. Norges teknisk-naturvitenskapelige universitet mottar en ny ROV, Minerva 2, som er temaet for denne oppgaven. Denne oppgaven fokuserer på tre aspekter av ROV-systemet. Dette er: den matematiske modellen av fartøyet, styringssystemet til fartøyet, og en evaluering av muligheten for å anvende systemidentifikasjon til fartøyet vill bli gjennomført.

Den matematiske modellen til fartøyet er utledet ved å vurdere en modell med 6 frihetsgraders for et marinefartøy. Stivt legeme bevegelsen kan utledes på bakgrunn av massen til ROV. De hydrodynamiske parameterne er blitt etablert for ROV, for å redegjøre for effekten av at fartøyet er nedsenket i vann. Dette gjøres ved å bruke beregningsverktøy. Den hydrodynamiske tillegsmassen bestemmes ved å bruke et verktøy basert på potensial teori og diffraksjon og radiasjons metodologi. Dempingen på fartøyet vil bli dominert av viskøse krefter, som neglisjeres i potensial teori. Av denne grunn brukes verktøy for numeriske strømnings beregning på en modell av fartøyet for å bestemme dempningskoeffisientene. Resultatet ble verifisert ved å vurdere et referanseobjekt med enkelt geometri som ble analysert både med beregningsverktøy og empiriske estimat. Resultatet for den hydrodynamiske tillegsmassen ga resultater som er i samsvar med forventningene. For dempingen tyder det på at den lineære delen er underestimert, mens den kvadratiske dele til dempingsfunksjonen er noe overestimert. En eksperimentell test ble designet for å teste en skala modell av ROV, og estimere de hydrodynamiske parameterne til ROV eksperimentelt. Problemer i forsøket knyttet til sensorjusteringen og bevegelsene på monteringsriggen gjorde at feil ble introduserte i målingen. Den beregnede dempingen ble funnet å være i samme størrelsesorden som for CFD-analysene. På grunn av unøyaktigheter i målingene var kvaliteten på dataene ikke tilstrekkelig gode nokk for at den hydrodynamiske tillegsmassen kunne bli beregnet med en akseptabel nøyaktighet.

Kontrollsystemet er basert på et eksisterende kontrollsystem utviklet for tidligere undervanns fartøy ved NTNU. Siden det nye fartøyet er kontrollert i 6 frihetsgrader, sammenlignet med 4 for de gamle fartøyene, har kontrolleren blitt utvidet for å ta hensyn til rulle- og stamp bevegelser. Minerva 2 er også en overaktuert ROV, noe som betyr at det er flere thrustere enn frihetsgrader. Dette resulterer i et system hvor det er ubegrenset mange kombinasjoner av thruster-hastigheter som kan resultere i en ønsket resultat. En ny thrust allokering ble utviklet for å bestemme den optimale kombinasjonen av thrusterhastighetene som tilsvarer en ønsket resultat. Dette ble gjort ved å definere et optimaliseringsmål for å minimere total fremdriftsenergi og løse thrust allokering problemet som et optimeringsproblem. Et sekundært mål

for thrust allokeringens problemet var å begrense vann fra å bli spylt foran kameraene, når det er mulig å unngå dette. Dette ble oppnådd ved å gi energi forbundet med thruster hastighet som forårsaker at vann blir spylt foran ROV en stor vekt. Utviklingen har også blitt gjort i autonomi-delen av kontrollsystemet. Hensikten med dette var å tillate separate programmer som utførte sonar- og kamerasporing, å videreformidle denne informasjonen til autonomisystemet i form av veipunkter. Dette ble testet med en virtuell integrering av ROV-kontrollsystemet, i en simulering av et inspeksjonsoppdrag.

En systemidentifikasjonsfunksjon har også blitt evaluert. Dette innebærer å beregne den matematiske modellen til fartøyet basert på responsen til fartøyet, dvs. dens bevegelser, og kontroll signalene. Både enkle simuleringer og simuleringer ved hjelp av prosessor i loop simuleringer ble brukt for å evaluere muligheten for et slikt system. Resultatet av disse simuleringen viste lovende resultat. Disse testene viser at med en tilstrekkelig stor måleprøve er systemidentifikasjonen i stand til å lage en matematisk modell av systemet med høy nøyaktighet.

Contents

Preface	I
Acknowledgment	III
Abstract	III
Sammendrag	VII
List of Figures, Tables and Abbreviations	XI
1 Introduction	1
1.1 Background	1
1.2 Project Outline	2
1.3 Literature Review	3
1.4 Minerva 2	7
1.5 Report Structure	9
2 Theory	11
2.1 ROV's	11
2.2 Mathematical Modelling	11
2.2.1 Rigid Body Motion	13
2.2.2 Hydrodynamics	14
2.2.3 Combined Model	18
2.2.4 Establishing Hydrodynamic Coefficient	19
2.3 Control Systems	24
2.3.1 Controller	24
2.3.2 Observer	25
2.3.3 Guidance System	26
2.3.4 Autonomous System	26
2.3.5 HIL Simulator	27
2.3.6 Thrust Allocation	28
2.4 System Identification	34
3 Method	39
3.1 Establishing Hydrodynamic Coefficients	39
3.1.1 Numerical	39
3.1.2 Experimental Test	45
3.2 System Identification	51
3.3 Development of the ROV Control System	52
3.3.1 Control System	52

3.3.2	HIL	55
3.3.3	GUI and Autonomy	55
3.4	Testing of Control System	55
4	Result	59
4.1	Hydrodynamic	59
4.1.1	Numerical Calculations	59
4.1.2	Experimental Test	64
4.2	Control System	69
4.2.1	Thrust Allocation	69
4.2.2	HIL Simulation 1	74
4.2.3	HIL Simulation 2	79
4.2.4	HIL Magnetometer Error Test	83
4.2.5	Joint Autonomy Simulation / Virtual Integration Test	86
4.3	System Identification	90
4.3.1	Simulation A	90
4.3.2	Simulation B	91
4.3.3	Simulation C (HIL)	92
5	Discussion	95
5.1	Hydrodynamic	95
5.1.1	Added Mass	95
5.1.2	Damping	97
5.1.3	Experimental Test	99
5.2	Control System	101
5.2.1	Thrust Allocation	101
5.2.2	HIL Simulation 1	102
5.2.3	HIL Simulation 2	103
5.2.4	Magnetometer Error Test	104
5.2.5	Joint Autonomy Simulation / Virtual Integration Test	105
5.3	System Identification	107
6	Conclusion	111
6.1	Further Work	112
	References	114
	Appendix	A-1
	Appendix A: Table of Added mass coefficients	A-1
	Appendix B: Additional Result from System Identification, Simulation A	A-5
	Appendix C: Additional Result from System Identification, Simulation B	A-7
	Appendix D: Additional Result from System Identification, Simulation C (HIL)	A-9
	Appendix E: Illustration of effect of magnetometer calibration error	A-11
	Appendix F: Damping for ROV Minerva	A-13
	Appendix G: Additional plots from the Experimental test	A-15
	Appendix F: System identification code	A-17

List of Figures

1.4.1	Illustration of the Minerva 2 ROV	7
1.4.2	Sketch of the layout of the thruster of the ROV. The figure show the x-z plane	8
1.4.3	Sketch of the layout of the thruster of the ROV. The figure show the x-y plane	8
1.4.4	Sketch of the layout of the thruster of the ROV. The figure show the y-z plane	9
2.3.1	An overview of the control system for Minerva 1 and the most important components of the system, [4]	24
2.4.1	Generic flow chart of the process of system identification, [23]	35
3.1.1	CAD model of the real ROV.	40
3.1.2	Simplified CAD model of the ROV, used for the hydrodynamic computations.	41
3.1.3	Model of the ROV that have been meshed using GeniE.	42
3.1.4	Illustration of the flow lines around the flotation block from a current flowing from above.	43
3.1.5	Flowchart of the hydrodynamic analysis	44
3.1.6	Reference cube meshed in GeniE.	45
3.1.7	Flow around the reference cylinder /rod.	45
3.1.8	Picture of the scale model of the ROV used for the experiment. . . .	46
3.1.9	Picture of the mounting bracket, [13]	47
3.1.10	The experimental setup of the test performed in the MC-Lab.	48
3.1.11	Towing test preformed on the mounting bracket as a reference for the experiment.	49
3.1.12	The experimental setup of the test performed in the MC-Lab.	50
3.3.1	Flowchart illustrating the simulation of the thrust allocation.	54
3.4.1	Graphical user interface of the control system, "Frigg".	56
3.4.2	Interface of the autonomy system.	56
3.4.3	Front panel of the control system, "Njord".	57
3.4.4	Front panel of the HIL simulator, "Verdandi".	57
4.1.1	Plot the damping function for the translational degrees of freedom along with the measurements from the CFD analysis.	61
4.1.2	Plot the damping function for the rotational degrees of freedom along with the measurements from the CFD analysis.	62
4.1.3	Plot of the negative par of the damping functions for low velocities, together with the measurements from the CFD analysis.	63
4.1.4	Plot of the forces measured for sensor 1 and 2, when the model of the ROV was towed in surge direction at a velocity of $0.7[m/s]$	65

4.1.5	Plot of the velocity of the towing cart when the model of the ROV is towed at a velocity of $0.7[m/s]$ in surge.	65
4.1.6	Plot of the forces measured for sensor 1 and 2, when the model of the ROV was towed in sway direction at a velocity of $1.2[m/s]$	66
4.1.7	Plot of the velocity of the towing cart when the model of the ROV is towed at a velocity of $1.2[m/s]$ in sway.	66
4.1.8	Plot of the forces when the mounting rig and when the ROV is towed with the mounting rig alone. In addition to this the net force on the model of the ROV is calculated and presented.	67
4.1.9	The figure presents the scaled average sway force and corresponding velocities found from the experimental test, together with the calculated damping function.	68
4.1.10	The figure presents the scaled average yaw moment and corresponding velocities found from the experimental test, together with the calculated damping function.	68
4.2.1	Desired sway force for the simulation of the thrust allocation.	69
4.2.2	Error in the calculated thrust for the simulation of the thrust allocation	70
4.2.3	Thruster speeds for the simulation of the thrust allocation, using method 1	70
4.2.4	Thruster speeds for the simulation of the thrust allocation, using method 2 with high values for S	71
4.2.5	Thruster speeds for the simulation of the thrust allocation, using method 2 with slightly larger values for S	72
4.2.6	Thruster speeds for the simulation of the thrust allocation, using method 2 without increasing the values for S	72
4.2.7	Thruster speeds for the simulation of the thrust allocation, using method 3	73
4.2.8	Comparison of the energy for the simulation of the thrust allocation	73
4.2.9	Comparison of the performance indicator for the simulation of the thrust allocation	74
4.2.10	Development motion of the ROV in North-East plane for the HIL simulation. The estimated states is presented together with the desired states and the measurements. The position in the figure is given in the UTM coordinate system.	75
4.2.11	Development motion of the ROV in North direction for the HIL simulation. The estimated states is presented together with the desired states and the measurements. The position in the figure is given in the UTM coordinate system.	76
4.2.12	Development motion of the ROV in East direction for the HIL simulation. The estimated states is presented together with the desired states and the measurements. The position in the figure is given in the UTM coordinate system.	76
4.2.13	Development vertical depth motion of the ROV for the HIL simulation. The estimated states is presented together with the desired states and the measurements. The position in the figure is given in the UTM coordinate system.	77

4.2.14	A 3 dimensional representation of the motion of the ROV during the tracking mission simulated with the HIL simulator. The position in the figure is given in the UTM coordinate system.	78
4.2.15	Development of the Roll, Pitch and yaw motion for the ROV during the HIL simulation. The estimated states is presented together with the desired states and the measurements.	79
4.2.16	Development of the motion in the North-East plane for the ROV during the HIL simulation with environmental disturbances. The estimated states is presented together with the desired states and the measurements, and the position is given in the UTM coordinate system.	80
4.2.17	Development of the motion in the North direction for the ROV during the HIL simulation with environmental disturbances. The estimated states is presented together with the desired states and the measurements, and the position is given in the UTM coordinate system.	81
4.2.18	Development of the motion in the East direction for the ROV during the HIL simulation with environmental disturbances. The estimated states is presented together with the desired states and the measurements, and the position is given in the UTM coordinate system.	81
4.2.19	Development of the motion in the vertical direction for the ROV during the HIL simulation with environmental disturbances. The estimated states is presented together with the desired states and the measurements, and the position is given in the UTM coordinate system.	82
4.2.20	Development of the Roll, Pitch and yaw motion for the ROV during the HIL simulation with environmental disturbances.	83
4.2.21	Plot of the motion of the ROV in a 3D figure for the HIL simulation with environmental disturbances. The estimated states is presented together with the desired states and the measurements, and the position is given in the UTM coordinate system.	83
4.2.22	Motion of the ROV in the North-East plane, for the HIL observer test. The position in the figure is given in the UTM coordinate system.	84
4.2.23	Development of the motion in North direction, for the HIL observer test. The position in the figure is given in the UTM coordinate system.	85
4.2.24	Development of the motion in East direction, for the HIL observer test. The position in the figure is given in the UTM coordinate system.	85
4.2.25	Development of the rotational DOF's in East direction, for the HIL observer test	86
4.2.26	Motion of the ROV in the North-East plane, for the Virtual integration test. The position in the figure is given in the UTM coordinate system.	87
4.2.27	Development of the motion in the North direction for the Virtual integration test. The estimated states is presented together with the desired states and the measurements. The position in the figure is given in the UTM coordinate system.	87

4.2.28	Development of the motion in the East direction for the Virtual integration test. The estimated states is presented together with the desired states and the measurements. The position in the figure is given in the UTM coordinate system.	88
4.2.29	Development of the motion in the vertical direction for the Virtual integration test. The estimated states is presented together with the desired states and the measurements.	89
4.2.30	Development of the Roll, Pitch and yaw motion for the ROV during the Virtual integration test.	89
4.2.31	Plot of the motion of the ROV in a 3D figure for the Virtual integration test. The estimated states is presented together with the desired states and the measurements. The position in the figure is given in the UTM coordinate system.	90
A1	Analytical added mass coefficient for two-dimensional bodies, i.e. long cylinders in infinite fluid (far from boundaries). Added mass (per unit length) is $A_{ij} = \rho C_A A_R$ [kg/m] where A_R [m^2] is the reference area, [39]	A-2
A2	Analytical added mass coefficient for three-dimensional bodies in infinite fluid (far from boundaries). Added mass is $A_{ij} = \rho C_A V_R$ [kg] where V_R [m^3] is reference volume, [39]	A-3
A3	Illustration of the effect of a small heading angle with respect to cross track error Δy and alongtrack error Δx	A-11
A4	Figure of the sensor measurements during yaw motion of the model of the ROV. The figure shows substantial level of noise, compared to the magnitude of the average value of the force.	A-15

List of Tables

1.1.1 ROV classes according to [26]	2
1.4.1 Angle of the thrusters for the ROV	9
1.4.2 Position of the thruster relative to ROV centre of gravity, given in the ROV coordinate system	9
2.2.1 Scaling factor for different parameters for a model test where Reynolds scaling is used.	23
2.3.1 Levels of autonomy defined according to [29]	27
3.4.1 Phases of the mission simulated in the virtual integration test	58
4.1.1 Comparison of drag coefficient found from empirical analysis and from CFD result	64
4.1.2 Table of the damping coefficient for the surge motion.	67
4.1.3 Table of the damping coefficient for the swat and yaw motion.	69
4.3.1 Performance of the system identification for the damping matrices in simulation B	91
4.3.2 Relative error in the diagonal terms in the quadratic damping D_Q . .	93

List of Abbreviation

<i>AROV</i>	Autonomous Remotely Operated Vehicle
<i>AUR-labb</i>	Applied Underwater Robotics Laboratory
<i>AUV</i>	Autonomous Underwater Vehicle
<i>CAD</i>	Computer aided design
<i>CFD</i>	Computational Fluid Dynamics
<i>COB</i>	Centre of Buoyancy
<i>COG</i>	Centre of Gravity
<i>DOF</i>	Degree of Freedom
<i>DVL</i>	Doppler Velocity Log
<i>DP</i>	Dynamic Positioning
<i>EKF</i>	Extended Kalman Filter
<i>FPGA</i>	Field-programmable gate array
<i>FVM</i>	Finite Volume Method
<i>GUI</i>	Graphical user interface
<i>HMD</i>	Head Mounted Display
<i>HIL</i>	Hardware In the Loop
<i>KF</i>	Kalman Filter
<i>LQR</i>	Linear Quadratic Regulator
<i>MC-labb</i>	Marine cybernetics laboratory
<i>NED</i>	North-East-Down
<i>NTNU</i>	Norwegian University of Science and Technology
<i>OOI</i>	Object Of Interest
<i>PI</i>	Performance Indicator
<i>PID</i>	Proportional-Integral-Derivative
<i>ROV</i>	Remotely Operated Vehicle
<i>RPM</i>	Rotations Per Minute
<i>TCP</i>	Transmission Control Protocol
<i>UDP</i>	User Datagram Protocol
<i>USBL</i>	Ultra Short Base Line
<i>UUV</i>	Unmanned Underwater Vehicle
<i>UUUV</i>	Unmanned Untethered Underwater Vehicle

Chapter 1

Introduction

This thesis cover the remotely operated vehicle (ROV) Minerva 2. The work include developing and adapting the control system, and in doing so establishing the hydrodynamics of the vessel. In addition to this development in the control system have been made so that the autonomy functions of the ROV can be used. The work on the control system was initiated in a project work the autumn of 2017, and part of this thesis, such as the parts regarding the thrust allocator, is directly based on and is an extension of the work done on this project.

1.1 Background

For underwater applications, unmanned underwater vehicles (UUV) are commonly used. The applications range from offshore oil and gas industry, subsea mineral extraction, installation of offshore infrastructure, science and research such as marine biology, seabed mapping, oceanographic research and marine archaeology, and military purposes, for example mine detection [11]. It is common to distinguish between two types of UUV's, the ROV and the autonomous underwater vehicle (AUV). One other method of distinguish UUV's is by whether they are tethered or not. Unmanned untethered underwater vehicles (UUUV) does not require any umbilical to provide power or communication. Most AUV's are also UUUV's. The advantage of the AUV's and UUUV's are that they are usually better suited to survey larger areas. This is because they are not connected to any surface vessel or fixed installations. Tethered underwater vehicles is usually controlled through the tether and is therefore considered as ROV's. For ROV's the size of the survey area is usually smaller than for the AUV's, since it must operate together with a surface vessel. On the other hand the spacial resolution of these vehicles usually allow the to performer more detailed surveys than the AUV's, [24]. AUV's are therefore more suited for simple surveys operations, as they are not limited by the need to receive communication and power from an external vessel. In order to increase efficiency, safety and precision of ROV operations motion control systems have been developed for ROV's.

Advanced control systems incorporation autonomous functions allow the ROV to perform missions autonomously. These ROV's are sometimes called autonomous ROV's (AROV), [32]. ROV's are usually designed so that they are very slightly positive buoyant so that little energy have to be used to stay submerged, but in case of any accidents or loss of power, the ROV will rise to the surface. The AUV's is

also designed to be positive buoyant. However since AUV's are usually not directly controlled in all degrees of freedom (DOF), the AUV needs to keep a forward velocity to keep its depth. For this reason there is usually a lower limit for the velocity of AUV's underwater, as they cannot hold position. Therefore it is difficult to obtain a video of an object of interest (OOI). This can be done for some AUV's, but usually with reduced resolution compared with an ROV. ROV's on the other hand are often used for more detailed inspections, subsea installation and maintenance. ROV's and AUV's therefore have complementary properties, and which one is best suited is always depended on the mission. It is useful to distinguish between ROV's according to their purpose. From [26] three classes of ROV's are defined. The three classes is presented in table 1.1.1.

Table 1.1.1: ROV classes according to [26]

Class 1	- Pure observation
Class 2	- Observation class
Class 2 A	Observation class vehicle with payload option
Class 2 B	Observation class vehicle with light intervention, survey and construction capabilities
Class 3	- Work class
Class 3 A	Work class vehicles typical $< 100kW$
Class 3 B	Work class vehicles typical $> 100kW$

The marine environment offers many opportunities as presented earlier, and for this reason the use of UUV's are increasing. However the marine environment also create some significant challenges. Two important effects that must be addressed when designing a marine control system is the effect of moving through water will have on the vessel. Secondly in the marine environment currents and waves will act on both surface and subsurface vessels. This can cause challenges that must be addressed. The study of hydrodynamics provide usefull tools to model and account for these effects. This field of research have developed, and especially the improved capacity of computer aided numerical analysis have become an ever more important part of hydrodynamic. This allows for study of the hydrodynamic properties of complex shapes such as many underwater vehicles.

1.2 Project Outline

This thesis will considered the development of the control system for the ROV Minerva 2. In doing this two main areas will be covered. The hydrodynamics of the ROV and the control system itself. The overall goal of the thesis is to develop the control system for Minerva 2 to a state where it can be tested and used for the Minerva 2.

As a preparation study for the master thesis a project work was performed considering the thrust allocator for the ROV. This control system have been developed and implemented in matlab for testing. In order for this to be used at Minerva 2 this

thrust allocator must be implemented in LabVIEW, which is used to develop the control system. There exist three main programs developed in LabVIEW for the control system. The Frigg and Njord programs constitute the graphical user interface (GUI) and control system respectively. Lastly a hardware in the loop (HIL) simulator called Verdandi is used to test the control system. To perform verification and validation of the implementation of the thrust allocator the system must be tested using the HIL simulator. To achieve this the necessary modification to the simulator must be made allowing for this testing. This will include updating the model in the HIL simulator and to adapt the communication between the controller and the HIL simulator.

The new ROV have the ability to be controlled in both roll and pitch, meaning two more DOF's than the existing system can handle. Necessary modification and extensions to the controller will be made to accommodate this. This will primarily include extending the control algorithm and allow for the input of the desired roll and pitch.

In order for the ROV control system to achieve an acceptable performance it is important that the mathematical model of the vessel that the control system is based upon accurately describe the motion of the ROV. To achieve this the rigid body mass, Coriolis force and the restoring forces must be found. In addition to this the hydrodynamic coefficients must be accurately determined. This will be done by using numerical computational tools and experimental tests. Verification of these results can be performed using empirical method. The mathematical model of the system can also be determined by the recorded data from the motion of the ROV using method from system identification. In this thesis an evaluation of the feasibility of applying system identification in the control system to calculate the model parameter to improve the performance of the system, will be carried out.

1.3 Literature Review

In the past couple of years the development of control systems for underwater vehicles have been an subject of increasing amount of research. One of the reasons for this is that underwater vehicles are used for more complex underwater operations and more demand to efficient use of these vessels are requiring more advanced control systems. In the following section a brief review of the most relevant literature for the topics covered in this thesis will be presented.

There are three doctoral theses that are covering the current ROV control system developed at NTNU. In [11] an assessment of hydrodynamic modelling for ROV applications is presented. Both mathematical models of the vessel dynamics and discussion regarding identifying hydrodynamics is treated here. This thesis also include a description and analysis of the control system for the NTNU operated ROV's. The development of this ROV control system is further detailed and expanded, as presented in [16] and [4]. In addition to these, [18] provide an overview of control, guidance and navigation, relevant for underwater vehicles.

The motion control system is presented in [11], where the modes of operation and the

base modules of the control system is presented. In this thesis focus is also directed at the observer for the control system. Advanced model based observers where there are interconnections between the translation observer and the attitude observer is considered, and the implementation tested. Result shows that the interconnections enhanced the performance of the control system. In [16] path generation and reference models are treated. The controller and observer is also considered. Thrust allocation is also evaluated for the ROV Minerva. Implementation and experiments results are evaluated and show that the accuracy of the parameters in the control plant model have a high positive impact. This implies that the hydrodynamic coefficients must be established with sufficient accuracy. The need for improved thruster modeling and control is also underlined. The reference models generated paths that favoured energy saving while moving, and resulted in higher overall tracking accuracy. In addition to this the tracking had a finite convergence time, but without the tracking time being optimal. Path planing and replanning systems and automatic mapping and planning is covered in [4]. here path planing using Voronoi diagram, which later is made smooth by Dubins path and Fermat spirals. This topic is also treated in [6]. Here Voronoi diagrams is used for path planning, and Fermat spirals is used to modify the path such that it becomes flyable for underwater vehicles. After a path is generated the clearance of the path is checked with the obstacles, and if the safety threshold is not met an alternative path is used. When there are multiple paths that satisfy the constrains a Dijkstra's algorithm is used to determine the shortest path. In [28] the thrust allocation / control allocation problem discussed. Here a thrust allocation for a 4 DOF UUV using 4 thrusters are covered. The thrust allocation problem is also covered in [37]

A Dynamic Positioning (DP) system for an ROV is developed and presented in [38]. A description of the control system along with along with experimental result is presented here. Test carried out of the station keeping resulted in a maximum measured deviation from the desired position of 9 [cm]. Work in [21] cover's techniques for detecting and removing outlier measurement from acoustic positioning. In the signal processing unit a method of determining if a measurement was an outlier based on a measurement-by-measurement implementation of a χ^2 test. A defined threshold separate outliers from measurement that is allowed to enter the Extended Kalman filter. A comparison of four different observers for a control system for an ROV is presented in [7]. The linear Kalman filter, extended Kalman filter, adaptive Kalman filter and nonlinear passive observer was tested in a full scale test in the Trondheim fjord, for a square shape path test. In [5] a hybrid control system using a multi-objective observer is considered. This work include a high-level supervisory system, determining which of the observer that will be used, and a set of different observers. Simulation result presented in this paper. A system using a head mounted display is presented in [8]. The work on HMD was intended to increase the efficiency of ROV teleoperation and telepresence. The control system developed for the NTNU ROV Minerva is also presented in [12]. Here the control system architecture is presented, and the modules is presented. Results from two observers, a sector heading Kalman filter and an extended Kalman filter is presented and compared. A modified heading observer is presented as well. The result shows that the extended Kalman filter performed best. It is desirable to orient an underwater vehicle so that it is moving with the sensors orthogonal to the seafloor. If this is not achieved both camera and

sonar imagery can become blurred. [27] consider the developed of a control strategy for achieving this. Experimental test where the heading and distance to the steep seafloor result shows promising results.

A method for designing a thrust allocation for over actuated ROV's is presented in [28]. The method is based on establishing a linear equation for each DOF of. These equations for the thrust in each DOF is dependent on the on the thruster speed. For a system with six DOF's and seven thruster, these equation represents six seven dimensional planes. The seven dimensional line that intersect all the hyper planes is will contain all the solution to the thrust allocation problem. The optimal solution can be determined by applying a optimisation routine on the set of possible solutions. In [28] thruster fault diagnosis and fault accommodation systems are also described. One challenging ROV operation is seabed mapping of underwater walls. To ensure that the sensors are used to their best effect, and the mission result is optimal, it would be desirable that the ROV would move with an orientation equal to the subsea wall. This is the topic in [27]. Here a guidance system is proposed, based on using Doppler velocity log measurement to estimate the gradient of the seabed / underwater wall. On the basis of this a guidance system is proposed to automatically adjust the orientation of the ROV, so that the orientation mach that of the seafloor.

It is expected that autonomous system will allow for more efficient and safer operations. For this reason much effort is put into development of autonomous marine operations. One of the benefit of applying autonomy for marine system is that this allows fewer people to be offshore at exposed location avoiding potentially dangerous situation. There are several different definitions of what constitute and autonomous system, and how it is classified. One way this can be done is according to [29]. Here four levels of autonomy are defined as; 1. Automatic operations, 2. Management by consent, 3. Management by exception and 4. Highly autonomous. The last represent a level of autonomy where the human is out of the loop and the system makes decisions independent of humans. A proposed architecture for autonomous system using a bottom up design approach, consisting of three levels of control. The top level involves mission planing and provide input for the guidance and optimisation layer. The remaining layer of control is the control execution level, where the control signals are calculated, [24]. The autonomy layer provide input to all of the three layers. The autonomous control system can be designed based on a hybrid control architecture containing both a deliberative layer and a reactive layer, [32]. An autonomy layer have been developed for the NTNU developed ROV control system in [32].

Most control systems are developed on the basis of a model of the system. To achieve good performance of a motion control system it is necessary that the model of the system accurately describe the real system. A model is usually established on the basis of physical relations, such as Newtons laws of motion. For practical purposes mathematical models of real systems are usually simplified. Identifying these model is an important aspect of the development of motion control systems. The field of System identification provide use full tools for control systems. In essence system identification aims to build mathematical model of the systems, [23]. Here methods on how mathematical models can be established on the basis of a sett of measure-

ment and input to the system. One strong approach presented here is using least square regression to establish models based on measurement and input. [23] outlines three basic requirements to establish a mathematical model of a system; 1. a data set, 2. A set of candidate model structures and 3. a defined rule that can be used to assess candidate models. The procedure of system identification should according to [23] involve first an experimental test to gather data from the system. Then system identification can be applied to determine a mathematical model of the system. Lastly all models should be tested against a separate data-set from the one used in the system identification. This aims to serve as a verification of the established model. If the model is accurate the result from the model and the verification test should be close to identical. System identification was used as a tool for the AUV Hugin, where ballasting errors were identified, [22]. This system worked by calculating the ballasting errors after the AUV was on a mission, and from this providing feedback to how the ballasting of the vessel should be changed before the next mission. Applications of system identification to determine the hydrodynamic parameters is presented in [30]. The hydrodynamic parameters were determined using the least square method. The results from system identification were compared to planar motion mechanism. [30] found that the result from system identification was larger errors associated with them compared to the result from planar motion mechanism.

Identification of hydrodynamic coefficients

An important topic for this thesis is to establish hydrodynamic parameters for the new ROV. There are several methods this can be done. In [13] three methods are described and compared. Computational Fluid Dynamics (CFD) based on potential flow theory and empirical estimates are compared for a selection of ROVs, and for two ROVs some experimental results are also presented and compared. In this thesis CFD is mainly used as a tool to verify the two methods by comparing the results with the ones produced by Wadam. The results show that the empirical methods generally provided estimations with fairly good accuracy, but there is a tendency for the empirical methods to underestimate the added mass in the rotational degrees of freedom. The damping is also estimated with fairly good accuracy, but tends to be overestimated. Advantages and disadvantages between the three methods are presented. The empirical methods and Wadam corresponded well, with a relative difference of 10 to 20% for the translational DOFs. The relative difference for the rotational DOFs were around 30 to 100%. A rough estimation of the hydrodynamic parameter can be performed by considering the ROV as a rectangular box. This can be done using 2D strip theory covered in [15]. In addition to this estimation can be made on the basis of empirical 3D data. A method of deriving the hydrodynamic coefficient using free decay test is presented in [33]. Here a procedure which applies differentiator filters to estimate the unknown velocities and acceleration is used, in the processing of the result from the free decay test, to calculate the hydrodynamic coefficient.

Empirical methods can be applied to determine the hydrodynamic coefficients for simple geometries. These are presented in [15] and [31]. These books provide tools for determining the added mass and damping for simple geometries. A procedure

to determine the hydrodynamic using both empirical and experimental analysis is presented in [14].

1.4 Minerva 2

The Applied underwater robotics laboratory (AUR-labb) at NTNU is a research centre for underwater robotics, [2]. The research application at this centre varies from biological surveys using underwater vehicles, evaluation of feasibility of sub-sea mining operations and the study of the underwater vehicle them selves. The AUR-labb is equipped with, along other things, ROV's and AUV's. A new ROV is acuiered by the AUR-labb to increase the range of possible underwater operation the lab can perform, and to be able to face more advanced challenges in the field of underwater robotics.

The new ROV NTNU is acquiring will be called Minerva 2. The new ROV will be equipped with seven thrusters. Four of these thrusters are placed in the horizontal plane. The remaining three thruster are position in a vertical direction. To avoid water being flushed through the ROV, these thrusters are tilted slightly. All of the thruster will have a fixed orientation. Minerva 2, will have substantially more propulsion power than the previous ROV's at NTNU. ROV's are often considered to be passively stable in roll and pitch, something that is used as an argument to disregard these DOF's. For Minerva 2 the thruster will introduce a large roll and pitch moments, so that roll and pitch motion must be accounted for in the control system and the thrust allocation. Figure 1.4.1 illustrate a ROV, on the basis of a computer model of the vessel.

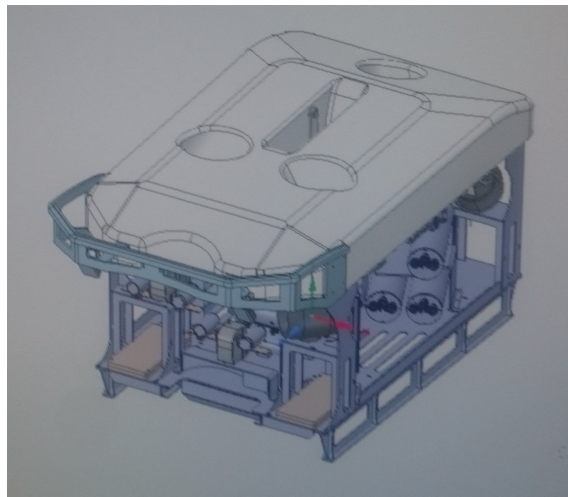


Figure 1.4.1: Illustration of the Minerva 2 ROV

The geometry of the thrusters are presented in the simplified drawings presented in figure 1.4.2, 1.4.3 and 1.4.4. These figures show the thruster geometries in the three planes xy -plane, xz -plane and yx -plane. The coordinate system in these drawing is the same as the coordinate system in the computer aided design (CAD) file of the ROV. For this reason the z-axis is forward, x- axis is directed to port and

the y axis is pointing upwards. This coordinate system will be used when defining the thrust allocation. For the control system the standard coordinate system for underwater vehicles will be used. Here x is forward, z is down and y is directed port. The angles specified in the figures are defined in table 1.4.1, and the thruster position is defined by table 1.4.2.

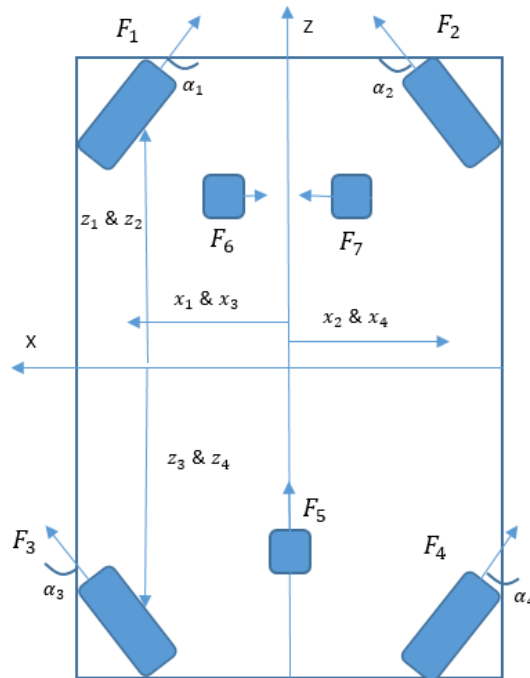


Figure 1.4.2: Sketch of the layout of the thruster of the ROV. The figure show the x-z plane

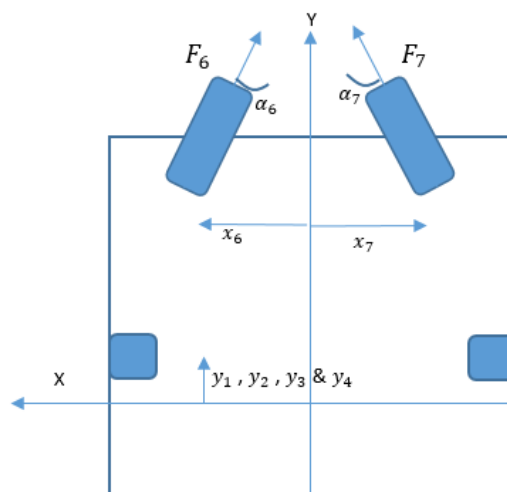


Figure 1.4.3: Sketch of the layout of the thruster of the ROV. The figure show the x-y plane

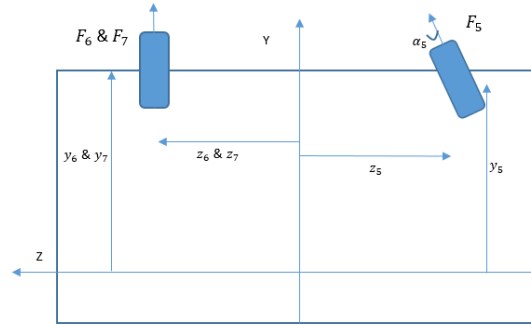


Figure 1.4.4: Sketch of the layout of the thruster of the ROV. The figure show the y-z plane

Table 1.4.1: Angle of the thrusters for the ROV

Thruster nr.	Symbol	Angle [Deg]
1	α_1	45
2	α_2	-45
3	α_3	-45
4	α_4	45
5	α_5	15
6	α_6	-30
7	α_7	30

Table 1.4.2: Position of the thruster relative to ROV centre of gravity, given in the ROV coordinate system

Thruster nr.	X [mm]	Y [mm]	Z [mm]
1	520	165	920
2	-520	165	920
3	520	165	-920
4	-520	165	-920
5	0.00	231.37	-940.19
6	575.705	284.68	550
7	-575.705	284.68	550

1.5 Report Structure

The first part of this thesis will present the theoretical background relevant to the thesis. Firstly mathematical modelling of the ROV will be presented in chapter 2 including both rigid body kinetics and hydrodynamics. The remaining part of chapter 2 will consider control systems. Here the different components of the control system will be presented. Lastly a method to apply system identification for an ROV will be covered. Chapter 3 will presented how the hydrodynamic coefficients was determined, and the process involving this. This chapter will also present the implementation of the thrust allocator and other relevant changes in the control system, including the system identification function. The result from the hydrodynamic analysis and mathematical modelling is presented in chapter 4. Result

from simulations of the control system and test of individual components will be presented later in chapter 4. The performance of the system identification will be presented before result from the test of the control system on the ROV is presented. This will be followed by a discussion of the result and the methods used, in chapter 5. Concluding remarks and further works will be presented in chapter 6.

Chapter 2

Theory

2.1 ROV's

Underwater vehicles are used for a variety of applications. The subtype ROV's can be useful for offshore work, subsea mining, archaeological and biological surveys. In order to reduce the energy required to keep the ROV submerged, the ROV's are usually designed to be neutrally buoyant, or slightly positively buoyant to ensure that the ROV float to the surface in the event of an accident. The ROV is equipped with a set of thrusters that is used to manoeuvre the ROV. The number and power of the thruster will vary for different types of ROV's. ROV's serve first and foremost as a sensor platform. The most common equipment on an ROV is cameras, that is used for subsea inspection. Many ROV's are also equipped with manipulator arms, or tools that can be used for subsea work. Sonars, and sensors that measure parameters in the water column. One particular common sensor is the Doppler velocity log (DVL), which is a sensor used to calculate the relative velocity of the sonar relative to the seabed. ROV's must often operate from a surface vessel. These can be installed with hydroacoustics positioning systems. The research vessel at NTNU, R/V Gunnerus is equipped with a Ultra Short Base Line (USBL) system of type HiPap 500, [1]. Most ROV's propulsion systems are either electrically or hydraulically powered. In order to control the motion of an ROV, a control system can be developed. This will be the focus of the remainder of this chapter. In order to obtain good performance of a ROV motion control system, the control system is based on a mathematical model of the ROV. This chapter will also cover the topic of establishing this model. Both directly, and using methods from system identification.

2.2 Mathematical Modelling

The study of motion and forces is the foundation for a model of an ROV. A motion control system aims to control the motion of a specific vessel, but to do this the relationship between forces and motion must be understood. The relationship between forces and motion is in the fundamental form described by Newton's second law of motion presented in equation 2.2.1. The mathematical model of the ROV will be based on this equation.

$$F = ma \quad (2.2.1)$$

An ROV can move in a three dimensional environment. This means that it has 3 directions of translation, along the axis, and 3 directions of rotation, rotation about the axis. The motion of the ROV is thus described in 6 degrees of freedom. For compact notation vector form is used. In marine engineering it is common practice to define the translations in a global reference frame as the vector $\boldsymbol{\eta}$, according to 2.2.2. Bold text indicate vector. The velocities is commonly described in a body fixed reference frame, and are called $\boldsymbol{\nu}$, according to 2.2.3

$$\boldsymbol{\eta} = [x, y, z, \phi, \theta, \psi]^T \quad (2.2.2)$$

$$\boldsymbol{\nu} = [u, v, w, p, q, r]^T \quad (2.2.3)$$

The position vector $\boldsymbol{\eta}$ is commonly defined in a global coordinate system, often the NED (North-East-Down) system. The ned reference frame is denoted $\{n\}$ and is defined relative to the Earth's reference ellipsoid [18]. The axis of the system is aligned in the North East and Down direction for the first, second and third axis respectively. A second reference that will be introduced in this thesis is the BODY frame. This frame is denoted $\{b\}$ and is fixed to the vessel, with first axis in the forward direction, second axis is in the port-starboard direction and third axis is in top bottom direction of the vessel. The velocity's $\boldsymbol{\nu}$ of the vessel is described in this frame.

Relationships between the ned position $\boldsymbol{\eta}$ and the body velocities $\boldsymbol{\nu}$ must be established for the mathematical model. The relation between the derivative of the position $\dot{\boldsymbol{\eta}}$ in ned frame and the body velocity $\boldsymbol{\nu}$ is found from trigonometry as equation 2.2.4

$$\dot{\boldsymbol{\eta}} = \boldsymbol{J}(\boldsymbol{\eta})\boldsymbol{\nu} \quad (2.2.4)$$

The Rotation transformation matrix $\boldsymbol{J}(\boldsymbol{\eta})$ is defined according to [18] in equation 2.2.5, where the Euler angles $\boldsymbol{\Theta} = [\psi, \theta, \phi]^T$ is used. The matrix $\boldsymbol{R}_b^n(\boldsymbol{\eta})$ is the rotation matrix from body frame to ned frame. This matrix contain the trigonometric relationship between the coordinate systems. The $\boldsymbol{T}_{\boldsymbol{\Theta}}$ matrix is a transformation matrix that relate the body fixed angular velocities $\boldsymbol{\omega} = [p, q, r]$ and the Euler angle $\boldsymbol{\Theta}$.

$$\boldsymbol{J}(\boldsymbol{\eta}) = \begin{bmatrix} \boldsymbol{R}_b^n(\boldsymbol{\Theta}) & \mathbf{0}_{3 \times 3} \\ \mathbf{0}_{3 \times 3} & \boldsymbol{T}_{\boldsymbol{\Theta}}(\boldsymbol{\Theta}) \end{bmatrix} \quad (2.2.5)$$

In the following section a mathematical model of an ROV will be established. This will be done by evaluating the different contribution to the forces and mass of the vessel. First, the rigid body motion of the ROV will be presented. This is can be considered as the forces acting on the vessel, if the vessel were to move in vacuum. Later the hydrodynamics of the ROV will be treated. In doing this the hydrodynamic forces acting on the ROV and the hydrodynamic coefficients will be defined.

On the basis of this a complete model of an under water vehicle will be established at the end of the section.

2.2.1 Rigid Body Motion

The study of kinetics is the study and forces and the motion this causes. When analysing the motion of an vessel it is use full to assume that it can be considered as a rigid body. This implies that it will not be deformed due to the forces acting on it. In the application of underwater vehicles this is a very reasonable assumption, and provide a use full tool for a kinetic analysis. The forces acting on the rigid body can be defined as $\boldsymbol{\tau}_{RB} = [X_{RB}, Y_{RB}, Z_{RB}, K_{RB}, M_{RB}, N_{RB}]^T$. From equation 2.2.1 the force due to the acceleration of the rigid body mass of the vessel can be found. In addition to this force, a rigid body Coriolis force \mathbf{C}_{RB} will act on the vessel due to the rotation of the earth. This result in the equation for the rigid body kinetics as 2.2.6, according to [17].

$$\boldsymbol{\tau}_{RB} = \mathbf{M}_{RB}\dot{\boldsymbol{\nu}} + \mathbf{C}_{RB}(\boldsymbol{\nu})\boldsymbol{\nu} \quad (2.2.6)$$

In equation 2.2.7 the rigid body mass is expressed as the matrix \mathbf{M}_{RB} . This matrix is often called the rigid body system inertia matrix, where $\mathbf{M}_{RB} \in \mathbb{R}^{6 \times 6}$. The mass of the body is denoted m . $\mathbf{r}_g^b = [x_g, y_g, z_g]$ is a vector from the origin to the centre of gravity (COG) in the body frame, and \mathbf{I}_b is the inertia matrix. From this the rigid body mass is determined from classic mechanics as 2.2.7 according to [18]

$$\mathbf{M}_{RB} = \begin{bmatrix} m\mathbf{I}_{3 \times 3} & -m\mathbf{S}(\mathbf{r}_g^b) \\ m\mathbf{S}(\mathbf{r}_g^b) & \mathbf{I}_b \end{bmatrix} = \begin{bmatrix} m & 0 & 0 & 0 & mz_g & -my_g \\ 0 & m & 0 & -mz_g & 0 & mx_g \\ 0 & 0 & m & my_g & -mx_g & 0 \\ 0 & -mz_g & my_g & I_x & -I_{xy} & -I_{xz} \\ mz_g & 0 & -mx_g & -I_{yx} & I_y & -I_{yz} \\ -my_g & mx_g & 0 & -I_{zx} & -I_{zy} & I_z \end{bmatrix} \quad (2.2.7)$$

The terms I_{ij} in the \mathbf{M}_{RB} matrix is the moment of inertia about the origin. The rigid body Coriolis and centripetal force $\mathbf{F}_{C_{RB}}$ can be derived according to [18], and is described by equation 2.2.8. The rigid body Coriolis and centripetal force is given by equation 2.2.9. This is an inertial force due to the rotation of the ROV reference frame relative to a global frame, [18].

$$\mathbf{F}_{C_{RB}} = \mathbf{C}_{RB}(\boldsymbol{\nu})\boldsymbol{\nu} \quad (2.2.8)$$

$$\mathbf{C}_{RB}(\boldsymbol{\nu}) = \begin{bmatrix} 0 & 0 & 0 & m(y_gq + z_gr) & -m(x_gq - w) & -m(x_gr + v) \\ 0 & 0 & 0 & -m(y_gp + w) & m(z_gr + x_gp) & -m(y_gr - u) \\ 0 & 0 & 0 & -m(z_gp - v) & -m(z_gq + u) & m(x_gp + y_gq) \\ -m(y_gq + z_gr) & m(x_gq - w) & m(x_gr + v) & 0 & -I_{yzq} - I_{xzp} + I_zr & I_{yzt} + I_{xyp} - I_{yq} \\ m(y_gp + w) & -m(z_gr + x_gp) & m(y_gr - u) & I_{yzq} + I_{xzp} - I_zr & 0 & -I_{xzt} - I_{xyq} + I_{xp} \\ m(z_gp - v) & m(z_gq + u) & -m(x_gp + y_gq) & -I_{yzt} - I_{xyp} + I_{yq} & I_{xzt} + I_{xyq} - I_{xp} & 0 \end{bmatrix} \quad (2.2.9)$$

For a body partly or fully submerged in any fluid there will exist a buoyancy because of the displaced fluid. This will act as a restoring force in the vertical direction

relative to the sea surface. In addition to the buoyancy force, gravity will act on the body in the same direction. The buoyancy force will act in the centre of buoyancy (COB), which is the centre of mass of the displaced fluid. This point might not coincide with the centre of gravity, where the mass force act, something that give rise to moments. A body is naturally stable if the centre of buoyancy is above the centre of gravity. This is because the buoyancy force is acting upwards, where as the weight is acting downwards. Any perturbations from this state will result in an lever arm between the forces that generate a moment that counteract the displacement. The net force and moment due to gravity and buoyancy $\mathbf{g}(\boldsymbol{\eta})$ can be derived generically according to [18], as presented in equation 2.2.10. The force vector become a function of the Euler angles, the weight of the body \mathbf{W} the buoyancy of the body \mathbf{B} , and the position of COG $[x_g, y_g, z_g]$ and COB $[x_b, y_b, z_b]$.

$$\mathbf{g}(\boldsymbol{\eta}) = \begin{bmatrix} (W - B)\sin(\theta) \\ -(W - B)\cos(\theta)\sin(\psi) \\ -(W - B)\cos(\theta)\cos(\phi) \\ -(y_g W - y_b B)\cos(\theta)\cos(\phi) + (z_g W - z_b B)\cos(\theta)\sin(\phi) \\ (z_g W - z_b B)\sin(\theta) + (x_g W - z_x B)\cos(\theta)\cos(\phi) \\ -(x_g W - x_b B)\cos(\theta)\cos(\phi) - (y_g W - y_b B)\sin(\theta) \end{bmatrix} \quad (2.2.10)$$

On the basis of the above terms presented a model a model of ROV's motion can be established when hydrodynamic forces are neglected. This is presented in equation 2.2.11.

$$\mathbf{M}_{RB}\dot{\boldsymbol{\nu}} + \mathbf{C}_{RB}(\boldsymbol{\nu})\boldsymbol{\nu} + \mathbf{g}(\boldsymbol{\eta}) = \boldsymbol{\tau}_{RB} \quad (2.2.11)$$

2.2.2 Hydrodynamics

Vessels moving in water is exposed to forces from the water. The study of hydrodynamics allows these forces to be quantified and accounted for. According to [15] the problem of identifying the hydrodynamic forces is usually dealt with by dividing the problems in two sub problems. These are the diffraction problem and the radiation problem. In the radiation problem the forces effecting the body when it oscillates is established. In the diffraction problem, the body is fixed, and the forces acting on the body due to incident waves if found. The total hydrodynamic force is then the sum of the radiation and diffraction problem, as presented in equation 2.2.12. For underwater vehicles it is important to establish the hydrodynamic properties to obtain acceptable performance for a motion control system for such a vessel. In the following section the most important hydrodynamic effects will be presented.

$$\mathbf{F}_{hydrodynamic} = \mathbf{F}_{diffraction} + \mathbf{F}_{radiation} \quad (2.2.12)$$

In the radiation problem the oscillating body will generate waves with a a velocity potential ϕ , associated with the forces in the radiated waves. It can be shown that these forces will have a term proportional to vessel acceleration and velocity. These terms are known as added mass and damping [15], and the general form is presented in equation 2.2.13. The term A_{kj} is the added mass coefficient in direction "k" due to motion in direction "j", similarly the term B_{kj} is the damping. In addition to the added mass and damping, restoring forces will affect the vessel. These forces

originate from the buoyancy and displacement of water of the vessel.

$$F_k^{rad} = -A_{kj} \frac{d^2 \eta_j}{dt^2} - B_{kj} \frac{d\eta_j}{dt} \quad (2.2.13)$$

The diffraction problem deals with the forces associated with the loads from the incident waves on the body. The diffraction force can be determined by integrating the dynamic pressure from the incident waves over the surface of the body. The dynamic pressure can according to [15] be expressed as $p_{dyn} = \rho \frac{\partial \phi_D}{\partial t}$. The excitation loads described by equation

$$F_{diff} = - \int_S \rho \frac{\partial \phi_D}{\partial t} n_k dS \quad (2.2.14)$$

For underwater applications deep water effect of waves are negligible, this implies that diffraction force can be ignored. This assumption is valid for most of the ROV operating condition, with exception for launch and recovery, and for motion in shallow waters.

Added mass

The added mass causes a load that is proportional to the acceleration of the body. The force appears as surrounding water particles are accelerated when a body is moving in the water. The radiation force can formally be written as equation 2.2.15, where the force is obtained by integrating the pressure over the surface of the body S , with the surface normal n_k . From this it clear that the added mass is depended on the body shape and size. The added mass is also dependent on the frequency of oscillation, and thus the frequency of the radiated waves. Underwater vehicles often operated at a depth deeper than the wave affected zone often defined by $d = \lambda/2$. Since the vehicles are not affected by waves at this depth the added mass and damping can be considered as independent of the wave frequency, [18]. For this reason the added mass of interest for underwater vehicles is at the frequency $\omega = \infty$

$$F_{rad} = - \int_S \rho \frac{\partial \phi_{rad}}{\partial t} n_k dS \quad (2.2.15)$$

When the radiated wave potential ϕ_{rad} is known the added mass and potential damping can be found from equation 2.2.15. The added mass is the term in equation 2.2.13 proportional to the acceleration $\left(\frac{\partial^2 \eta_j}{\partial t^2}\right)$, and with the notation from control theory the added mass force can be written as 2.2.16.

$$\mathbf{F}_{M_A} = \mathbf{M}_A \dot{\mathbf{v}} \quad (2.2.16)$$

The matrix \mathbf{M}_A is the added mass matrix, containing the added mass coefficient, which for an underwater vehicle moving in 6 DOF, will become a 6×6 matrix. One typical representation of this matrix is presented in equation 2.2.17, according to [37]

$$\mathbf{M}_A = \begin{bmatrix} X_{\dot{u}} & X_{\dot{v}} & X_{\dot{w}} & X_{\dot{p}} & X_{\dot{q}} & X_{\dot{r}} \\ Y_{\dot{u}} & Y_{\dot{v}} & Y_{\dot{w}} & Y_{\dot{p}} & Y_{\dot{q}} & Y_{\dot{r}} \\ Z_{\dot{u}} & Z_{\dot{v}} & Z_{\dot{w}} & Z_{\dot{p}} & Z_{\dot{q}} & Z_{\dot{r}} \\ K_{\dot{u}} & K_{\dot{v}} & K_{\dot{w}} & K_{\dot{p}} & K_{\dot{q}} & K_{\dot{r}} \\ M_{\dot{u}} & M_{\dot{v}} & M_{\dot{w}} & M_{\dot{p}} & M_{\dot{q}} & M_{\dot{r}} \\ N_{\dot{u}} & N_{\dot{v}} & N_{\dot{w}} & N_{\dot{p}} & N_{\dot{q}} & N_{\dot{r}} \end{bmatrix} \quad (2.2.17)$$

As mentioned can the added mass be seen as the additional mass of fluid that must be moved when the body is moving. This will have one additional effect that must be accounted for. The Coriolis and centripetal forces from added mass must be established. This is a term proportional to the velocities $\boldsymbol{\nu}$, as presented in equation 2.2.18. The Coriolis and centripetal force will act on the added mass similarly as for the rigid body described earlier. For underwater vehicles operating at low speeds the effect of the Coriolis force will be small, and can in some cases be ignored.

$$\mathbf{F}_{C_A} = \mathbf{C}_A(\boldsymbol{\nu})\boldsymbol{\nu} \quad (2.2.18)$$

In order to calculate the Coriolis and centripetal force on the underwater vehicle the Coriolis and centripetal matrix for added mass \mathbf{C}_A must be established. It can be shown that the Coriolis and centripetal matrix can always be parameterized as a skew-symmetric matrix [18]. Furthermore, this matrix is the forces due to the movement of the added mass of the vessel in the body frame which is rotating about the inertial NED frame. The matrix can therefore be determined from the added mass matrix, and the velocity vector $\boldsymbol{\nu}$. The Coriolis and centripetal matrix can be derived according to [37], and become equation 2.2.19.

$$\mathbf{C}_A = \begin{bmatrix} 0 & 0 & 0 & 0 & -a_3 & a_2 \\ 0 & 0 & 0 & a_3 & 0 & -a_1 \\ 0 & 0 & 0 & -a_2 & a_1 & 0 \\ 0 & -a_3 & a_2 & 0 & -b_3 & b_2 \\ a_3 & 0 & -a_1 & b_3 & 0 & -b_1 \\ -a_2 & a_1 & 0 & -b_2 & b_1 & 0 \end{bmatrix} \quad (2.2.19)$$

Where the parameters in 2.2.19 are defined by equation 2.2.20, according to [37].

$$\begin{aligned} a_1 &= X_{\dot{u}}u + X_{\dot{v}}v + X_{\dot{w}}w + X_{\dot{p}}p + X_{\dot{q}}q + X_{\dot{r}}r \\ a_2 &= Y_{\dot{u}}u + Y_{\dot{v}}v + Y_{\dot{w}}w + Y_{\dot{p}}p + Y_{\dot{q}}q + Y_{\dot{r}}r \\ a_3 &= Z_{\dot{u}}u + Z_{\dot{v}}v + Z_{\dot{w}}w + Z_{\dot{p}}p + Z_{\dot{q}}q + Z_{\dot{r}}r \\ b_1 &= K_{\dot{u}}u + K_{\dot{v}}v + K_{\dot{w}}w + K_{\dot{p}}p + K_{\dot{q}}q + K_{\dot{r}}r \\ b_2 &= M_{\dot{u}}u + M_{\dot{v}}v + M_{\dot{w}}w + M_{\dot{p}}p + M_{\dot{q}}q + M_{\dot{r}}r \\ b_3 &= N_{\dot{u}}u + N_{\dot{v}}v + N_{\dot{w}}w + N_{\dot{p}}p + N_{\dot{q}}q + N_{\dot{r}}r \end{aligned} \quad (2.2.20)$$

Strip theory can be used to calculate the added mass of a body on the basis of a two dimensional added mass coefficient. The two dimensional added mass coefficient represent the added mass for a cross section of the body. When strip theory is used it is assumed that the variation in the flow in the cross-section plane is much larger

than the variation of the flow in the longitudinal direction, [15]. Strip theory involves dividing the body into a finite number of strips in the longitudinal direction. The added mass and damping is then found using a two dimensional coefficient and integration along the length of the body, determining the total added mass and damping. The added mass in surge can be represented by equation 2.2.21. The reader is referred to [15], [31] and [18] for a more detailed description of the strip theory.

$$A_{11} = \int_{-L/2}^{L/2} A_{11}^{2D} dx \quad (2.2.21)$$

The values of the added mass coefficients can be found analytically by solving equation 2.2.15. When the added mass is found the corresponding Coriolis and centripetal added mass coefficient can be determined from equation 2.2.19. For many real applications it is not practically to solve equation 2.2.15 manually. Computational tools using numerical methods have been developed to calculate the hydrodynamic coefficients such as the added mass. In addition to this experimental test can be used to identify the added mass of a vessel. From studies of added mass from simple shapes added mass coefficients for these simple shapes can be found. These can be used in an empirical estimated of the added mass. This will be further detailed later in this chapter.

Damping

The damping forces are identified as the forces proportional to the velocities $\left(\frac{\partial \eta_j}{\partial t}\right)$ in equation 2.2.13, with the damping coefficient \mathbf{B} . The damping forces can be calculated from potential theory with equation 2.2.15. The damping force is associated with energy being transported away from the body. The damping force is, similar to the added mass, frequency depended. For high frequent waves the the body will be able to dissipate energy through waves. For this reason the damping coefficients B_{ij} will approach zero as the frequency increase towards infinity, thus $\lim_{\omega \rightarrow \infty} B_{ij} = 0$ for all values "i" and "j". In hydrodynamic literature the damping terms are commonly denoted \mathbf{B} , whereas it is more common to denote the damping as \mathbf{D} in control literature. From this point on the control convention for notation will be used for damping. Aside from the potential damping there will also be damping from effects that are not accounted for in potential theory. These will often have an important contribution. For underwater vehicles operating in deep water, where there will be no wave, these effects will constitute the entire damping. Theses damping effects are; damping due to vortex shedding D_S , damping due to skin friction D_M and wave drift damping D_W , [13]. When establishing damping from model experiments scaling effect must be accounted for such as for skin friction which is more important in model tests, [15]. The damping matrix can be divided into one linear part and one nonlinear part according to equation 2.2.22, [37] & [18]

$$\mathbf{D}(\boldsymbol{\nu}) = \mathbf{D}_L(\boldsymbol{\nu}) + \mathbf{d}_{NL}(\boldsymbol{\nu}) \quad (2.2.22)$$

In the representation in 2.2.22 The linear damping term D_L arise from potential

damping and linear skin friction. The damping force due to vortex shedding can be modelled from the drag part of the Morrison equation 2.2.23 and together with nonlinear skin friction are modelled as \mathbf{d}_{NL} . Equation 2.2.23 present the drag part of the Morrison equation, which is also the generic equation for drag force, given a drag coefficient.

$$F_{D,Vortex}(u) = -\frac{1}{2}\rho C_D(R_n)A|u|u \quad (2.2.23)$$

In the Morrison equation, the drag coefficient C_D is dependent on the Reynolds number R_n given by equation 2.2.24. Here u is the flow velocity, L is the length along the flow, and ν is the kinematic viscosity.

$$R_n = \frac{uL}{\nu} \quad (2.2.24)$$

The skin friction damping can as previously mentioned be divided into a linear part and a nonlinear part. The nonlinear part is typically quadratic. From the Morrison equation it can be seen that the drag due to vortex shedding can be modelled as quadratic as well. For this reason the representation in 2.2.25 is used for the hydrodynamic damping on the ROV. The damping is modelled as a sum of a linear term \mathbf{D}_L and a quadratic term \mathbf{D}_q . The damping function $\mathbf{D}(\boldsymbol{\nu})$ described by 2.2.25 must be strictly positive to be of physically meaning. This is because energy is removed from the system through damping, [11].

$$\mathbf{D}(\boldsymbol{\nu}) = \mathbf{D}_L\boldsymbol{\nu} + \mathbf{D}_q\boldsymbol{\nu}|\boldsymbol{\nu}| \quad (2.2.25)$$

For ROV's the damping matrices can be simplified as a diagonal matrix. This is a common assumption, since the diagonal terms will be dominating [11], and establishing the off diagonal terms will be a complex and difficult process that will not be of great importance.

The paragraphs above outline a theoretical approach to determining added mass and damping for and underwater vehicle. However since underwater vehicles often have complex shapes analytically solutions might be very difficult to obtain, if at all possible for this reason several alternative approaches can be used to identify the added mass and damping for the ROV. This will be covered later in this section

2.2.3 Combined Model

On the basis of the sections above a model for the motion of an underwater vehicle can be established. A complete model of the motion of the vessel will contain both the rigid body kinetics presented in section 2.2.1 and the hydrodynamics presented in section 2.2.2. The combined equation of motion for the vessel is presented in equation 2.2.26 and is identified as a mass spring damper system.

$$(\mathbf{M}_{RB} + \mathbf{M}_A)\dot{\boldsymbol{\nu}} + (\mathbf{C}_{RB}(\boldsymbol{\nu}) + \mathbf{C}_A(\boldsymbol{\nu}))\boldsymbol{\nu} + \mathbf{D}(\boldsymbol{\nu}) + \mathbf{g}\boldsymbol{\eta} = \boldsymbol{\tau} \quad (2.2.26)$$

The terms in equation 2.2.26 is defined in the two previous section. The forces vector $\boldsymbol{\tau}$ is a vector containing all forces acting on the vessel. This include the rigid body forces, the hydrodynamic forces, the thruster forces and any other external force

acting on the vessel. The hydrodynamic contribution can be formulated according to 2.2.27. The total forces acting on the vessel is the hydrodynamic forces, the forces acting on the rigid body, and external forces: $\boldsymbol{\tau} = \boldsymbol{\tau}_{Hydrodynamic} + \boldsymbol{\tau}_{RB} + \boldsymbol{\tau}_{ext}$. The external forces can originate from current or from other forces that are not accounted for in this model. The excitation forces presented in equation 2.2.27 is the wave excitation forces, and account for all the forces in the diffraction problem. This is forces associated with the forces acting on the vessel from incident waves, [15], and consist of the wave diffraction forces and Froude-Kriloff forces.

$$\boldsymbol{\tau}_{hydrodynamic} = -M_A \dot{\boldsymbol{\nu}} - C_A \boldsymbol{\nu} - (D_L + D_q |\boldsymbol{\nu}|) \boldsymbol{\nu} + \boldsymbol{\tau}_{excitation} \quad (2.2.27)$$

2.2.4 Establishing Hydrodynamic Coefficient

In order to accurately model the motion of the vessel with equation 2.2.26 the hydrodynamic coefficients for added mass and damping must be determined. This can be found in several different methods. The first method that will be considered is an analytically approach. This method will give the most accurate result, but is severely limited by how complicated a geometry can be before it cannot be solved. For complicated geometries computer programs using numerical methods can be used. These provide some use full tools in hydrodynamic analysis, but the result should always be verified to ensure the quality is sufficiently good. For many simple geometries experimental test have been performed, and empirical data is available on the basis of these result. These result is typically parametric in terms of the geometry. This data can be used to find the hydrodynamic coefficient for some geometries. When possible experimental can be performed. This gives a possibility to measure the added mass and damping. In the following section these methods will covered.

Analytically methods

The added mass and damping can be found analytically by solving the equation radiation problem given by equation 2.2.15. This require knowledge of the radiated wave potential ϕ_{rad} . This information is often not available. One method to determine the added mass analytically is by using strip theory. Here the two dimensional added mass and damping coefficient combined with strip theory can be used to find an approximation to the added mass and damping, [15]. One important limitation with the strip theory is that the theory is bases on the assumption that variation in flow is much larger in the cross sectional plane than in the longitudinal direction, [15]. This assumption will not be accurate at the end of the the body. For this reason strip theory is more accurate for longer and slender bodies, where this effect is smaller. This method is based on knowledge of the two dimensional added mass. For some geometries this vales are known or can be found analytically.

Numerical analysis

Many structures, objects and vessels have a complex geometry. For these cases the added mass and damping can be difficult or impossible to determine. One common numerical method used computer software to calculate the added mass and damping is panel methods. In these methods flow separation is neglected and potential

theory is used. One common application of panel models are in conjunction with a source-sink approach, [15]. This involve placing sources and sinks along the surface of the body. From the distribution of the sources and sinks and the boundary conditions, such as the boundary condition on the mean wetted body given, the added mass and damping is determined.

One software that use this is the DNV-GL developed Wadam / HydroD, a part of the SASAM software package. This software use methods based on radiation and diffraction methodology and panel models [34], as presented in section 2.2.2. Since this program is based on the potential theory, viscous effects are ignored. For added mass this will not have significant consequences, however underwater vehicles at deep water the damping from potential theory will be zero. To determine the damping, programs accounting for viscous and nonlinear effect must be used. This means that CFD program must be used to determine the damping.

CFD is a numerical tools that solve the Navier-Stokes equation, given by equation 2.2.28, and the continuity equation 2.2.29, [40]. The analysis is performed over a defined volume with a specified boundary conditions, and where the interactions between the body and fluid is calculated. There exist several CFD tools, with can be suitable for different purposes. One such tool is Solidworks Flow simulator. This is a program is a part of the Solidworks Computer aided design (CAD) tool. This allows for easy mode ling in CAD, and analysis of the model in the CFD Flow Simulator. CFD programs can be based on different methods for solving the governing differential equations. One such method is the Finite Volume Method (FVM), [35]. This method have similarities with the Finite element method, where the system is discretized and meshed. The finite volume refers to the volume surrounding each node in the mesh. This method is applied in Solidworks flow simulator.

$$\rho \frac{D\mathbf{V}}{Dt} = \rho \mathbf{g} - \nabla p + \mu \nabla^2 \mathbf{V} \quad (2.2.28)$$

$$\text{div} \mathbf{V} = 0 \quad (2.2.29)$$

Empirical analysis

The added mass and damping can also be determined empirical data. Data exist for many simple geometries as function of the geometrical parameters. Empirical data is typical found by performing many experimental test and recording the result for some general shape with different parameters. This can for example be a box with different side length and thickness. Data for three dimensional added mass and two dimensional added mass is found in [39], and is presented in appendix A.

The hydrodynamic data can in principle be determined for the ROV from empirical data. However due to the complex geometry, this is not practical. Instead empirical methods can serve as a check on the hydrodynamic data calculated with one of the other mentioned method. This can be achieved by performing an added mass analysis with numerical tools presented above, for a simple geometry. The result can be checked and verified against empirical data. The empirical added mass will then

be found by determining the two and three dimensional added mass using table in figure A1 and table in figure A2 in the appendix. For the three translational DOF's the three dimensional added mass can be computed directly using the added mass coefficient C_A from table in figure A2, and equation 2.2.30

$$A_{ij} = \rho C_A V_R \quad (2.2.30)$$

In equation 2.2.30 the water density is ρ and the volume of the object is V_R . The rotational added mass cannot be directly determined from the 3D added mass coefficient, and must be determined from strip theory. The result using the 3D added mass and using 2D added mass with strip theory will not be identical. To account for this the added mass for the translational degrees of freedom can be used to calculate the difference between the two approaches, and a scaling factor λ can be determined [13]. This scaling factor can be determined with equation 2.2.31 and the added mass from strip theory can be determined using the approach in equation 2.2.21

$$\lambda = \frac{A_{ii}^{empirical\ 3D}}{A_{ii}^{Strip-Theory}} \quad (2.2.31)$$

On the basis of this the result using strip theory on the rotational degrees of freedom can be determined by scaling the result using λ as presented in equation 2.2.32. In this equation it is assumed that the added mass coefficient is constant along the length of the body, which implies that the geometry is constant.

$$A_{ii} = \int_{-L/2}^{L/2} A_{ii}^{2D} dx * \lambda \quad (2.2.32)$$

The damping forces can be calculated as the drag forces on a body. For some simple geometries, the drag coefficient C_D can be found for different Reynolds numbers defined by 2.2.24. Table values for the drag coefficient can be found in [3] for both 2D and 3D objects of some geometries. With the drag coefficient, the drag force can be determined with equation 2.2.23. This drag force can then be compared for values calculated with numerical tools. If the use of the numerical tool is correct, and the CFD analysis is accurate, the difference should be small.

Experimental analysis

The added mass and damping can as mentioned also be determined from experimental analysis. This is a very valuable tool, as the data acquired is from a physical system, and not an modelled system where some physical properties are neglected. Because of this the result from the experimental test can be directly linked to the added mass and damping of the vessel. The accuracy of the experimental test are however limited by a couple of factors. Firstly, how accurate the instruments measuring the forces are. The accuracy of these sensors will directly effect the calculated added mass and damping. The accuracy of the sensors is also affected by the installation of the sensors. Furthermore, experimental test to determine the hydrodynamic properties is often performed in towing tanks. Since these are tanks where the sides are a finite distance from the tested body, effect from the sides can affect the measurement. This can for example be reflected waves. Lastly one

important consideration that must be made is the difference in scale of the tested object relative to the real object. If a test is performed on a model of an underwater vehicles the hydrodynamic properties will be different from the real vehicles due to the size. The hydrodynamic properties will also have the properties that all effect does not scale in the same way. This give rise to scale effect that must be accounted for.

Hydrodynamic coefficients can be determined from experimental test by performing several towing test, while measuring velocity, acceleration and force on the vessel. By performing a towing test with a constant velocity $\boldsymbol{\nu}$ the accelration becomes $\dot{\boldsymbol{\nu}} = 0$. Then equation 2.2.26 become the simplified 2.2.33. The rigid body and added mass Coriolis and centripetal matrix \mathbf{C}_{RB} and \mathbf{C}_A can be for a scale model, moving at low velocities can be neglected. The restoring forces can also be established from equation 2.2.10. The unknown parameters that must be calculated is the two damping coefficients \mathbf{D}_L and \mathbf{D}_q .

$$(\mathbf{D}_L + \mathbf{D}_q|\boldsymbol{\nu}|)\boldsymbol{\nu} + \mathbf{g}(\boldsymbol{\eta}) = \boldsymbol{\tau} \quad (2.2.33)$$

Equation 2.2.33 can be rewritten in the form in equation 2.2.34 where the unknown terms are gathered on one side.

$$(\mathbf{D}_L + \mathbf{D}_q|\boldsymbol{\nu}|)\boldsymbol{\nu} = \boldsymbol{\tau} - \mathbf{g}(\boldsymbol{\eta}) \quad (2.2.34)$$

With the measured forces $\boldsymbol{\tau}$, for different constant velocities, equation 2.2.34 can be solved as a set of equation with three unknown. These unknown are matrices in dimension $\mathbb{R}^{6 \times 6}$. When these tree matrices are established new test can be performed, with an acceleration. This implies that the added mass term does not vanish in equation 2.2.26, and the added mass matrix can be determined.

Not all laboratory setups allow for towing at exact zero acceleration. This implies that there will be added mass forces acting on the vessel. One way this can be solved is in equation 2.2.34, to put the added mass on the left hand side, and solve for all four matrices \mathbf{M}_A , \mathbf{C}_A , \mathbf{D}_L and \mathbf{D}_Q . This is however not desired as this is more prone to errors. The measurement of the acceleration can be challenging, and an inaccurate measurement will with this approach also affect the damping matrices and the Coriolis added mass. When towing with an acceleration, sensors to measure the acceleration should be used to obtain satisfactory result, if possible,[13].

For practical purposes many experiments cannot be performed on full size vessels. For this reason scale models of the vessels are often used. One challenging aspect of performing model test is the scaling of the forces and mass. The viscous forces and gravity forces does not scale equally. The ratio between the gravity forces and the inertia forces are described by the froude number, defined by equation 2.2.35. In this equation U is the flow velocity, g is the acceleration of gravity and L is the characteristic length of the object. If a scale model and a full size model have the same froude number, the gravity forces will be scaled correctly. Surface waves are gravity driven. For this reason it is important for vessels where the hydrodynamic forces are dominated by wave effects, that the froude number is the same. The ratio of the length of the scale model and the real vessel is the scale of the ROV.

$$F_N = \frac{U}{\sqrt{gL}} \quad (2.2.35)$$

The ratio of the inertia forces and the viscous forces on the ROV is described by the Reynolds number presented in equation 2.2.24. For the viscous forces to be scaled correctly the Reynolds number must be identical. The challenge of the scaling problem is that it is difficult to be able to scale the viscous and gravity forces together. For this reason one of the two must be chosen. There exist other scaling laws, but the two most used is Reynolds scaling, i.e scaling the viscous forces, and Froude scaling, i.e scaling the gravity forces. For deeply submerged ROV's the viscous effects will be the primary contributor to the force. This is because the ROV will largely operate at a depth so that the effect of waves can be neglected. For this reason a Reynolds scaling can be used for ROV's. For studies of ROV in the launch and descent phase and during motion at shallow water the effect of waves will become more important, and a Froude scaling can become more relevant.

When the viscous forces are important, an experiment can be performed by applying Reynolds scaling. The Reynolds number is kept constant between the model scale, marked by subscript m , and the full scale body, marked by subscript f . If the velocity the full scale body can be expected to move with is known, the velocities for the experiments can be calculated by equation 2.2.36. The scaling factor is defined as $\lambda = \frac{L_f}{L_m}$, where L is the characteristic length of the body.

$$\begin{aligned} \frac{u_m L_m}{\nu} &= \frac{u_f L_f}{\nu} \\ &\implies \\ u_m &= \lambda u_f \end{aligned} \quad (2.2.36)$$

The scaling of forces and masses can be derived from physical units, and are presented in table 2.2.1. The multiplication factor is in this table derived by analysis of the dimensions of the parameters. This is based on a similar process done for Froude scaling presented in [36].

Table 2.2.1: Scaling factor for different parameters for a model test where Reynolds scaing is used.

Parameter	Unit	Multiplication Factor
Length	m	λ
Velocity	$\frac{m}{s}$	$\frac{1}{\lambda}$
Acceleration	$\frac{m}{s^2}$	$\frac{1}{\lambda^3}$
Time	s	$\frac{1}{\lambda^2}$
Mass	kg	λ^3
Force	N	1
Moment	Nm	λ

2.3 Control Systems

The ROV control system consist of several modules. The existing control system developed at NTNU is primarily covered in [11], [16] and [4]. In the following a general overview of control system related to underwater vehicles will be given. The aim is to give the reader a overview of all the modules, and not go into detail on all parts of the control system. Instead more attention will be given to the parts of the control system which have been developed in this thesis, such as the thrust allocator. The most important modules are presented in figure 2.3.1, and are: the signal processing, the state estimator or observer, the controller, the thrust allocator and the guidance system. In addition to this a graphical user interface is necessary to provide user commands to the guidance system. The modules will each be presented in the sections below.

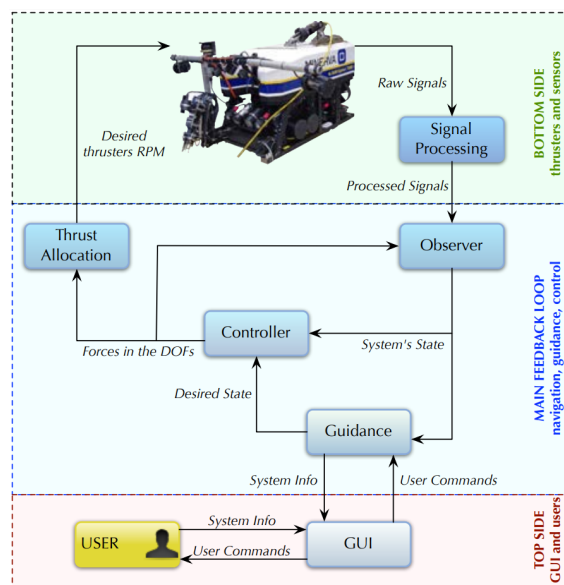


Figure 2.3.1: An overview of the control system for Minerva 1 and the most important components of the system, [4]

2.3.1 Controller

The aim of the controller is to provide a control input τ_c , calculated on the basis of the estimated and the offset between them and the desired position. The controller provide the necessary thrust for each degree of freedom. The controller receive the estimated states as input from the observer module, and the desired states as input from a guidance system or reference generator. There are several different types of controllers, but the most commonly used are the linear-quadratic-regulator (LQR) type and the proportional-integral-derivative (PID). The LQR controller determine the control action by solving an optimality criteria [18]. The PID type controller calculate three gains, one proportional to the error, the second based on the time integral of the error, and the third based on the derivative of the error. The PID type and LQR are the most commonly used controller. Aside from these two, controllers can also be designed with other methods such as feedback linearization or backstepping. For nonlinear systems feedback linearization have the advantage

that nonlinear terms can be canceled, and the system can be brought to a linear form, and the origin can be stabilized [20]. Backstepping is another approach to design controllers for nonlinear systems. This approach have a recursive form, and although have many similarities with feedback linearization, backstepping is more flexible, and allows for stabilizing terms to be retained. This means that controller energy is not wasted on canceling terms that are stabilizing the system [20]. The controller that is implemented on the ROV control system is a nonlinear PID. This is a common choice for the controller due to their good performance, relatively simple implementation and their flexibility. The nonlinear PID controller is given by equation 2.3.1,[11]

$$\tau_c = -\mathbf{J}^\top(\boldsymbol{\eta}) \left(\mathbf{K}_p \tilde{\boldsymbol{\eta}} + \mathbf{K}_d \mathbf{J}(\boldsymbol{\eta}) \boldsymbol{\nu} + \mathbf{K}_i \int_0^t \tilde{\boldsymbol{\eta}}(\tau) d\tau \right) \quad (2.3.1)$$

The gains \mathbf{K}_p , \mathbf{K}_i and \mathbf{K}_d is the proportional, integral and derivative gain respectively. By tuning these the gains the desired behaviour of the system can be included. In the ROV control system an anti-windup scheme is included to prevent the integral term from winding up.

2.3.2 Observer

On the basis of the measurements the states of the system can be estimated by an state estimator or observer. The observer use a mathematical model of the system along with the measurements and the control input to provide measurement of the sates of the system, even the states that are unmeasured. There are many different types of state estimators, with different strength and weaknesses. One commonly used observer is the Kalman filter (KF). When measurement noise and process noise is Gaussian distributed white noise, the noise co variances are known and the system linear and the state space model is known exactly, the Kalman filter can be shown to be optimal [25]. An extended Kalman filter (EKF) can be used for nonlinear system. The NTNU developed control system implemented on the ROV use an EKF. A discrete EKF is given according [18] as equation 2.3.2, 2.3.3 and 2.3.4.

$$\begin{aligned} \bar{\mathbf{x}}_{k=0} &= \mathbf{x}_0 \\ \bar{\mathbf{P}}_{k=0} &= \mathbf{P}_0 \end{aligned} \quad (2.3.2)$$

$$\begin{aligned} \mathbf{K}_k &= \bar{\mathbf{P}}_k \mathbf{H}^\top \left[\mathbf{H} \bar{\mathbf{P}}_k \mathbf{H}^\top + \mathbf{R} \right]^{-1} \\ \bar{\mathbf{P}}_{k=k} &= (\mathbf{I} - \mathbf{K}_k \mathbf{H}) \bar{\mathbf{P}}_k = (\mathbf{I} - \mathbf{K}_k \mathbf{H})^\top + \mathbf{K}_k \mathbf{R} \mathbf{K}_k^\top \\ \hat{\mathbf{x}}_{k=k} &= \bar{\mathbf{x}}_k + \mathbf{K}_k (\mathbf{y}_k - \mathbf{H} \bar{\mathbf{x}}_k) \end{aligned} \quad (2.3.3)$$

$$\begin{aligned} \bar{\mathbf{x}}_{k+1} &= \mathbf{f}_k(\hat{\mathbf{x}}_k, \mathbf{u}_k) \\ \bar{\mathbf{P}}_{k+1} &= \bar{\boldsymbol{\Phi}}_k \hat{\mathbf{P}}_k \bar{\boldsymbol{\Phi}}_k^\top + \boldsymbol{\Gamma}_k \mathbf{Q} \boldsymbol{\Gamma}_k^\top \end{aligned} \quad (2.3.4)$$

Equation 2.3.2 provide the initial values, at $k = 0$, for the EKF. The initial states \mathbf{x}_0 and the initial covariance propagation matrix \mathbf{P}_0 is used to initial the Kalman filter. The corrector step is presented in equation 2.3.3. The Kalman filter gain \mathbf{K}_k is calculated for each time step k . The \mathbf{R} matrix is the measurement noise covariance matrix. The estimated state $\hat{\mathbf{x}}$ is calculated in this step. Equation 2.3.4 is the predictor step of the EKF, and in this step the error covariance matrix for the next step $\bar{\mathbf{P}}_{k+1}$ is calculated, along with $\bar{\mathbf{x}}_{k+1}$. The terms $\bar{\boldsymbol{\Phi}}$ and $\boldsymbol{\Gamma}$ are obtained

by discretization the continuous time state space model. The equations above is designed for the continuous time state space system presented in equation 2.3.5.

$$\begin{aligned}\dot{\mathbf{x}} &= \mathbf{f}(\mathbf{x}) + \mathbf{B}\mathbf{u} + \mathbf{E}\mathbf{w} \\ \mathbf{y} &= \mathbf{H}\mathbf{x} + \mathbf{v}\end{aligned}\tag{2.3.5}$$

For many control systems it is common to linearize the rotation matrix into a set of sectors, usually 36 sectors of 10° . This is done to save computational resources. For underwater applications this process is usually done only for the heading of the vessel, as the roll and pitch motion is usually passively stable. The roll and pitch motion is commonly linearized around 0° in the interval $[-5^\circ, 5^\circ]$. The observer is based on measurement from the sensors together with calculations made on the basis of mathematical model of the ROV.

2.3.3 Guidance System

The guidance module provide the desired values for the controller. This is the position, velocities or orientation the controller will force the vessel toward. In order to have a good control system performance, it is desired that the change of these states are smooth and continuous. For this reason the guidance system often include a model of the physical system, such as a mass-spring-damper, to generate a trajectory for the desired states. For DP operations the desired states will be constant, where as for a tracking mission, the desired state will change. Without a reference generator, the change in set points will cause jerk on the vessel, and performance can be reduced. When the control system is operating with a human in the loop, the guidance system translate the input from the operator to desired states for the control system.

2.3.4 Autonomous System

Autonomy is an ever developing field of research. Autonomy can be introduced as a part of the control systems. There are multiple definitions of autonomy. One definition according to [29] where four levels of autonomy is defined as presented in table 2.3.1. There are different approaches to designing autonomous systems. A deliberate architecture is an approach that are dependent on knowledge of systems [32]. This architecture generally follows the structure sense, plan act. By defining a set of scenarios for the system, the deliberative architecture allow for planning and modelling of the mission based on a model of the system, [32]. A system based on reactive architecture is a system where reactive behaviour is desired. The sensors provide input, that are used to determine a reaction from the system. The behaviour of the system is determined by a set of blocks defining a reaction to a certain stimulus, [19].

A hybrid architecture combining both reactive and deliberate layers. The deliberative layer takes care of the mission planing. The reactive layer will deal with situations that are not a part of the mission plan. In order to combine the two architecture a control executive layer is used as a logic switch between the two. This layer will act as the supervisor for the deliberative and reactive layer [19]. This can be done by defining states of there system, and recognisable parameters for this state. From this it can be determined whether or not a given state have been

Table 2.3.1: Levels of autonomy defined according to [29]

Level of Autonomy	Definition
1. Automatic Operation:	The vessel moves autonomous, but there is a human operator with direct control of mission function.
2. Autonomous by consent:	The system performs the defined task and propose recommendations for mission actions that the operator will chose from.
3. Autonomous by exception:	The system automatically performs mission related function when the reaction time is to small. The operator is informed about the mission progress and exceptions to the mission are brought fort to the operator that makes a decision.
4. Highly autonomous:	The system performs all mission related functions. The operator is informed about mission progress.

reached. Furthermore safe state condition should be defined. Where the deliberative layer will check whether a certain state of the mission have been reach, for example distinguishing between the launch phase and the descent phase of an ROV mission, the reactive layer continuously listen to sensor input for example to determine if there is any obstacles in the way. If there is an obstacle detected by the reactive layer the behaviour of the vessel should be changed. To achieve this the reactive layer is given priority over the deliberative layer in the control executive layer, [32]. There exist different approaches to achieve an autonomous or partly autonomous system.

2.3.5 HIL Simulator

It is use full to test control system to verify that the control system operates as it is supposed. One practical way this can be done is using hardware inn the loop (HIL) simulators. This have also been introduced into rules and regulations for ships as a requirement for testing of marine control systems, [38]. HIL simulations involve testing the control system with a simulator of the ship environment. The same control system can be plugged into a HIL simulator and a real system. The aim of the HIL testing is to filter out bugs and errors in the code and to ensure that the system is performing as desired.

The HIL simulator is a simulator that provide states as input for the control system, and receives the control signals from the controller. To achieves this the HIL simulator contain a mathematical model of the system. This model will for an underwater vehicle be on the form presented in equation 2.2.26. Usually a version of this equation will be used, where noise and disturbances are modelled. This is important to test the control systems sensitivity to process disturbances and measurement noise. HIL simulators are often developed to include simulations of the

measurement systems and will thus provide realistic input to the control system.

2.3.6 Thrust Allocation

The thrust allocator is the module that convert desired thruster forces in degrees of freedom to a sett of speeds for each individual thruster. The generic formulation of the thrust allocation problem is described by equation 2.3.6 below. The thrust notation for the thrust allocation will be kept according to [18]. The general procedure for solving a thrust allocation can be found in [18]. In addition to this [28], provide useful tools and methods that are used to solve over actuated systems.

$$\boldsymbol{\tau}_c = \mathbf{T}_{conf} \mathbf{T}_d \quad (2.3.6)$$

in equation 2.3.6 $\boldsymbol{\tau}_c = \mathbb{R}^{6 \times 1}$ is the control vector from the control system with forces in 6 DOF. $\mathbf{T}_d = \mathbb{R}^{7 \times 1}$ is the thruster vector that contains the thrust for each of the seven thrusters, and $\mathbf{T}_{conf} = \mathbb{R}^{6 \times 7}$ is the thrust configuration matrix. Using notation defined in [18] we can write.

$$\boldsymbol{\tau}_c = [X, Y, Z, K, M, N]^\top \quad (2.3.7)$$

And

$$\mathbf{T}_d = [F_1, F_2, F_3, F_4, F_5, F_6, F_7]^\top \quad (2.3.8)$$

Where F_i is the thrust for each of the seven thrusters. The thruster configuration matrix is given from the geometry, and presented below in equation 2.3.9. The values used to generate this matrix are found from the geometry presented in figure 1.4.2, 1.4.3 and 1.4.4. The lengths x_i , y_i and z_i are presented in table 1.4.2.

$$\mathbf{T}_{conf} = \begin{bmatrix} \frac{\sqrt{2}}{2} & \frac{\sqrt{2}}{2} & \frac{\sqrt{2}}{2} & \frac{\sqrt{2}}{2} & \frac{\sqrt{6}-\sqrt{2}}{4} & 0 & 0 \\ \frac{\sqrt{2}}{2} & -\frac{\sqrt{2}}{2} & -\frac{\sqrt{2}}{2} & \frac{\sqrt{2}}{2} & 0 & -\frac{1}{2} & \frac{1}{2} \\ 0 & 0 & 0 & 0 & \frac{\sqrt{6}+\sqrt{2}}{4} & \frac{\sqrt{3}}{2} & \frac{\sqrt{3}}{2} \\ \frac{\sqrt{2}}{2} y_1 & -\frac{\sqrt{2}}{2} y_2 & -\frac{\sqrt{2}}{2} y_3 & \frac{\sqrt{2}}{2} y_4 & 0 & -\frac{1}{2} x_6 + \frac{\sqrt{3}}{2} y_6 & \frac{1}{2} x_7 - \frac{\sqrt{3}}{2} y_7 \\ \frac{\sqrt{2}}{2} y_1 & \frac{\sqrt{2}}{2} y_2 & \frac{\sqrt{2}}{2} y_3 & \frac{\sqrt{2}}{2} y_4 & \frac{\sqrt{6}+\sqrt{2}}{4} z_5 + \frac{\sqrt{6}-\sqrt{2}}{4} y_5 & -\frac{\sqrt{3}}{2} z_6 & -\frac{\sqrt{3}}{2} z_7 \\ -\frac{\sqrt{2}}{2} [x_1 + z_1] & -\frac{\sqrt{2}}{2} [x_2 - z_2] & -\frac{\sqrt{2}}{2} [x_3 - z_3] & -\frac{\sqrt{2}}{2} [x_4 + z_4] & 0 & -\frac{1}{2} z_6 & \frac{1}{2} z_7 \end{bmatrix} \quad (2.3.9)$$

In the matrix above the thruster position and angle relative to the x-axis is represented by $(x_i, y_i, z_i, \alpha_i)$. The trust allocation problem is to find the required forces from each actuator based on the total required force in the system DOF's, which is equal to finding \mathbf{T}_d . This is presented in equation 2.3.10 below.

$$\mathbf{T}_d = \mathbf{T}_{conf}^\dagger \boldsymbol{\tau}_c \quad (2.3.10)$$

$\mathbf{T}_{conf}^\dagger$ represent the pseudo inverse of the previously mentioned thruster configuration matrix. The input to the thrusters on the ROV are the thruster speed \mathbf{u} , and can be found from the relation $\boldsymbol{\tau} = \mathbf{T}_{conf} * \mathbf{T}_d = \mathbf{T}_{conf} * \mathbf{K} * \mathbf{u}$. Where \mathbf{u} is defined as in equation 2.3.11

$$\mathbf{u} = [u_1, u_2, u_3, u_4, u_5, u_6, u_7]^\top \quad (2.3.11)$$

In equation 2.3.11, u_i represent the thruster speed for each of the seven thrusters. The relation between the force and the speed is also used, and the \mathbf{B} matrix is

defined as 2.3.12.

$$\begin{aligned}
 \boldsymbol{\tau}_c &= \mathbf{T}_{conf} * \mathbf{T}_d \\
 \boldsymbol{\tau}_c &= \mathbf{T}_{conf} * \mathbf{K} * \mathbf{u} \\
 \mathbf{B} &= \mathbf{T}_{conf} \mathbf{K}
 \end{aligned} \tag{2.3.12}$$

The thrust allocation algorithm will be on a similar form as presented in [28]. The \mathbf{K} is defined in 2.3.13. The different K_i is used to map the thrust to a given speed is used to formulate the a set of equation relating the forces and moments to the thruster speed, based on the thruster configuration. This is presented in equation 2.3.14.

$$\mathbf{K} = \begin{bmatrix} K_1 & 0 & 0 & 0 & 0 & 0 & 0 \\ 0 & K_2 & 0 & 0 & 0 & 0 & 0 \\ 0 & 0 & K_3 & 0 & 0 & 0 & 0 \\ 0 & 0 & 0 & K_4 & 0 & 0 & 0 \\ 0 & 0 & 0 & 0 & K_5 & 0 & 0 \\ 0 & 0 & 0 & 0 & 0 & K_6 & 0 \\ 0 & 0 & 0 & 0 & 0 & 0 & K_7 \end{bmatrix} \tag{2.3.13}$$

$$\begin{bmatrix} \tau_x \\ \tau_y \\ \tau_z \\ \tau_k \\ \tau_m \\ \tau_n \end{bmatrix} = \begin{bmatrix} \frac{\sqrt{2}}{2} K_1 & \frac{\sqrt{2}}{2} K_2 & \frac{\sqrt{2}}{2} K_3 & \frac{\sqrt{2}}{2} K_4 & \frac{\sqrt{6-\sqrt{2}}}{4} K_5 & 0 & 0 \\ \frac{\sqrt{2}}{2} K_1 & -\frac{\sqrt{2}}{2} K_2 & -\frac{\sqrt{2}}{2} K_3 & \frac{\sqrt{2}}{2} K_4 & 0 & -\frac{1}{2} K_5 & \frac{1}{2} K_6 \\ 0 & 0 & 0 & 0 & \frac{\sqrt{6+\sqrt{2}}}{4} K_5 & \frac{\sqrt{3}}{2} K_6 & \frac{\sqrt{3}}{2} K_7 \\ \frac{\sqrt{2}}{2} y_1 K_1 & -\frac{\sqrt{2}}{2} y_2 K_2 & -\frac{\sqrt{2}}{2} y_3 K_3 & \frac{\sqrt{2}}{2} y_4 K_4 & 0 & \left(-\frac{1}{2} x_6 + \frac{\sqrt{3}}{2} y_6\right) K_6 & \left(\frac{1}{2} x_7 - \frac{\sqrt{3}}{2} y_7\right) K_7 \\ \frac{\sqrt{2}}{2} y_1 K_1 & \frac{\sqrt{2}}{2} y_2 K_2 & \frac{\sqrt{2}}{2} y_3 K_3 & \frac{\sqrt{2}}{2} y_4 K_4 & \left(\frac{\sqrt{6+\sqrt{2}}}{4} z_5 + \frac{\sqrt{6-\sqrt{2}}}{4} y_5\right) K_5 & -\frac{\sqrt{3}}{2} z_6 K_6 & -\frac{\sqrt{3}}{2} z_7 K_7 \\ -\frac{\sqrt{2}}{2} [x_1 + z_1] K_1 & -\frac{\sqrt{2}}{2} [x_2 - z_2] K_2 & -\frac{\sqrt{2}}{2} [x_3 - z_3] K_3 & -\frac{\sqrt{2}}{2} [x_4 + z_4] K_4 & 0 & -\frac{1}{2} z_6 K_6 & \frac{1}{2} z_7 K_7 \end{bmatrix} * \begin{bmatrix} u_1 \\ u_2 \\ u_3 \\ u_4 \\ u_5 \\ u_6 \\ u_7 \end{bmatrix} \tag{2.3.14}$$

On the basis of equation 2.3.14 the \mathbf{B}_e matrix is established in equation as 2.3.15 from linear algebra, and becomes 2.3.16.

$$\mathbf{B}_e = [\mathbf{T}_{conf}, \boldsymbol{\tau}] \tag{2.3.15}$$

$$\mathbf{B}_e = \begin{bmatrix} \frac{\sqrt{2}}{2} K_1 & \frac{\sqrt{2}}{2} K_2 & \frac{\sqrt{2}}{2} K_3 & \frac{\sqrt{2}}{2} K_4 & \frac{\sqrt{6-\sqrt{2}}}{4} K_5 & 0 & 0 & \tau_x \\ \frac{\sqrt{2}}{2} K_1 & -\frac{\sqrt{2}}{2} K_2 & -\frac{\sqrt{2}}{2} K_3 & \frac{\sqrt{2}}{2} K_4 & 0 & -\frac{1}{2} K_5 & \frac{1}{2} K_6 & \tau_y \\ 0 & 0 & 0 & 0 & \frac{\sqrt{6+\sqrt{2}}}{4} K_5 & \frac{\sqrt{3}}{2} K_6 & \frac{\sqrt{3}}{2} K_7 & \tau_z \\ \frac{\sqrt{2}}{2} y_1 K_1 & -\frac{\sqrt{2}}{2} y_2 K_2 & -\frac{\sqrt{2}}{2} y_3 K_3 & \frac{\sqrt{2}}{2} y_4 K_4 & 0 & \left(-\frac{1}{2} x_6 + \frac{\sqrt{3}}{2} y_6\right) K_6 & \left(\frac{1}{2} x_7 - \frac{\sqrt{3}}{2} y_7\right) K_7 & \tau_k \\ \frac{\sqrt{2}}{2} y_1 K_1 & \frac{\sqrt{2}}{2} y_2 K_2 & \frac{\sqrt{2}}{2} y_3 K_3 & \frac{\sqrt{2}}{2} y_4 K_4 & \left(\frac{\sqrt{6+\sqrt{2}}}{4} z_5 + \frac{\sqrt{6-\sqrt{2}}}{4} y_5\right) K_5 & -\frac{\sqrt{3}}{2} z_6 K_6 & -\frac{\sqrt{3}}{2} z_7 K_7 & \tau_m \\ -\frac{\sqrt{2}}{2} [x_1 + z_1] K_1 & -\frac{\sqrt{2}}{2} [x_2 - z_2] K_2 & -\frac{\sqrt{2}}{2} [x_3 - z_3] K_3 & -\frac{\sqrt{2}}{2} [x_4 + z_4] K_4 & 0 & -\frac{1}{2} z_6 K_6 & \frac{1}{2} z_7 K_7 & \tau_n \end{bmatrix} \tag{2.3.16}$$

On the basis of the above equation 2.3.16 and 2.3.12, formulate the equation of six hyper planes in seven dimensions. Each of these planes represent the equation for each of the thrust degree of freedom X , Y , Z , K , M , & N . These planes contains the solution of each equation as a functions of the thruster speed u_i where $i \in [1, 2, 3, 4, 5, 6, 7]$. The solution of the thrust allocation problem is at the intersection of these six hyper planes, [28]. This intersection is a set of solutions, \mathfrak{R} , that solve the thrust allocation problem. These planes are defined inn equation 2.3.17-2.3.22.

$$\pi_x : \quad \tau_x = \frac{\sqrt{2}}{2} u_1 K_1 + \frac{\sqrt{2}}{2} u_2 K_2 + \frac{\sqrt{2}}{2} u_3 K_3 + \frac{\sqrt{2}}{2} u_4 K_4 + \frac{\sqrt{6-\sqrt{2}}}{4} u_5 K_5 \tag{2.3.17}$$

$$\pi_y : \quad \tau_y = \frac{\sqrt{2}}{2}u_1K_1 - \frac{\sqrt{2}}{2}u_2K_2 - \frac{\sqrt{2}}{2}u_3K_3 + \frac{\sqrt{2}}{2}u_4K_4 - \frac{1}{2}u_6K_6 + \frac{1}{2}u_7K_7 \quad (2.3.18)$$

$$\pi_z : \quad \tau_z = \frac{\sqrt{6} + \sqrt{2}}{4}u_5K_5 + \frac{\sqrt{3}}{2}u_6K_6 + \frac{\sqrt{3}}{2}u_7K_7 \quad (2.3.19)$$

$$\begin{aligned} \pi_k : \quad \tau_k = & \frac{\sqrt{2}}{2}y_1u_1K_2 - \frac{\sqrt{2}}{2}y_2u_2K_3 - \frac{\sqrt{2}}{2}y_3u_3K_4 + \frac{\sqrt{2}}{2}y_4u_4K_5 \\ & - \left(-\frac{1}{2}x_6 + \frac{\sqrt{3}}{2}y_6 \right) K_6u_6 + \left(\frac{1}{2}x_7 - \frac{\sqrt{3}}{2}y_7 \right) K_7u_7 \end{aligned} \quad (2.3.20)$$

$$\begin{aligned} \pi_m : \quad \tau_m = & \frac{\sqrt{2}}{2}y_1u_1K_2 - \frac{\sqrt{2}}{2}y_2u_2K_3 - \frac{\sqrt{2}}{2}y_3u_3K_4 + \frac{\sqrt{2}}{2}y_4u_4K_5 \\ & + \left(\frac{\sqrt{6} + \sqrt{2}}{4}z_5 + \frac{\sqrt{6} - \sqrt{2}}{4}y_5 \right) K_5u_5 - \frac{1}{2}u_6K_6 + \frac{1}{2}u_7K_7 \end{aligned} \quad (2.3.21)$$

$$\begin{aligned} \pi_n : \quad \tau_n = & -\frac{\sqrt{2}}{2}[x_1 + z_1]u_1K_1 - \frac{\sqrt{2}}{2}[x_2 + z_2]u_2K_2 - \frac{\sqrt{2}}{2}[x_3 + z_3]u_3K_3 \\ & - \frac{\sqrt{2}}{2}[x_4 + z_4]u_4K_4 - \frac{1}{2}z_6u_6K_6 + \frac{1}{2}z_7u_7K_7 \end{aligned} \quad (2.3.22)$$

The set \mathfrak{N} contains all solution of \mathbf{u} that solve the problem $\mathbf{B} * \mathbf{u} = \boldsymbol{\tau}$ [28], which is the intersection between the six hyperplanes. We can now apply the saturation constraint, to define a constrained control subset Ω defined in equation 2.3.23.

$$\Omega = \left\{ \mathbf{u} \in \mathfrak{R}^7 \mid \|\mathbf{u}\|_\infty \leq u_{max} \mid \min(\mathbf{u}) \geq u_{min} \right\} \quad (2.3.23)$$

There exist three and only three possible cases. 1: Ω is empty, and there is no exact solution to the trust allocation problem. 2: Ω have exactly one element, which is thus the only and optimal solution to the thrust allocation problem. and 3: Ω have more than one element, and there is thus many \mathbf{u} that solve the thrust allocation problem. For the later case the optimal solution must be determined. This is the topic for the rest of this section . There are multiple methods that can be used to obtain the set of solution to the trust allocation problem \mathfrak{N} . An analytically and generic solution would allow the thrust allocation algorithm to operate for all possible input thrust, and would create a foundation for a fast and computational inexpensive solution. Motivated by this the method presented in section below was developed.

Solving the thrust allocation problem

In order to find the thruster speed \mathbf{u} six linear equations 2.3.17-2.3.23 must be solved together. The system is reduced on the form in equation 2.3.24. As can be seen from the equation there is a free variable. This is a result of the system being over

actuated. The solution can be obtained by a parametrization of the system based in terms of the free variable.

$$\mathbf{R}_e = \begin{bmatrix} 1 & A_1 & B_1 & C_1 & D_1 & E_1 & F_1 & X_1 \\ 0 & 1 & B_2 & C_2 & D_2 & E_2 & F_2 & X_2 \\ 0 & 0 & 1 & C_3 & D_3 & E_3 & F_3 & X_3 \\ 0 & 0 & 0 & 1 & D_4 & E_4 & F_4 & X_4 \\ 0 & 0 & 0 & 0 & 1 & E_5 & F_5 & X_5 \\ 0 & 0 & 0 & 0 & 0 & 1 & F_6 & X_6 \end{bmatrix} \quad (2.3.24)$$

The system in equation 2.3.24 correspond to the equations presented in equation. 2.3.25.

$$\begin{aligned} u_7 &= x \\ u_6 &= X_6 - x * F_6 \\ u_5 &= X_5 - x * F_5 - u_6 * E_5 \\ u_4 &= X_4 - x * F_4 - u_6 * E_4 - u_5 * D_4 \\ u_3 &= X_4 - x * F_3 - u_6 * E_3 - u_5 * D_3 - u_4 * C_3 \\ u_2 &= X_4 - x * F_2 - u_6 * E_2 - u_5 * D_2 - u_4 * C_2 - u_3 * B_2 \\ u_1 &= X_4 - x * F_1 - u_6 * E_1 - u_5 * D_1 - u_4 * C_1 - u_3 * B_1 - u_2 * A_1 \end{aligned} \quad (2.3.25)$$

This can be simplified to the equation presented below 2.3.26.

$$\begin{aligned} u_7 &= x \\ u_6 &= a_6 - b_6 x \\ u_5 &= a_5 - b_5 x \\ u_4 &= a_4 - b_4 x \\ u_3 &= a_3 - b_3 x \\ u_2 &= a_2 - b_2 x \\ u_1 &= a_1 - b_1 x \end{aligned} \quad (2.3.26)$$

This result in a linear system of equations depended of the parameter x . The system of equation in 2.3.26 represents intersection of the solution of degrees of freedom, previously called \mathfrak{N} . All values of x will therefore solve the thrust allocation problem, however selecting x must be made so that the thruster speed does not exceed the maximum thruster speed. On the basis of the system of equations that solve the thrust allocation problem, one solution must be selected. In order to determine an optimal solution, there must be an optimization objective. For an ROV a reasonable objective is to minimize the energy consumption of the ROV or to minimize the thruster speed for some chosen thruster. The next to sections will present procedures for determining the optimal thrust considering minimum energy consumption, and minimum thruster speed for selected thrusters

Thrust allocation - Minimize energy

In order to determine the optimal thrust allocation to minimize the energy, the energy consumption must be modeled. The thruster energy can be modeled as a proportion to the square of the thruster speed according to equation 2.3.27, since the kinetic rotation energy is proportional to angular velocity square. The total propulsion energy is therefore modeled as the sum of propulsion energy for each thruster, according to equation 2.3.28.

$$E \propto u^2 \quad (2.3.27)$$

In equation 2.3.27, E is the energy for the thruster.

$$E_{tot} = \sum_{i=1}^7 S_i * u_i^2 \quad S_i = unknown \quad (2.3.28)$$

In equation 2.3.28 the thruster energy is modeled as a constant S_i multiplied with the square of the thruster speed. This constant account for the thruster characteristics. Since all thrusters for the ROV is assumed to be equal, this constant will be equal for all thrusters and will therefore not contribute to the solution for the energy optimization problem. However different S_i can be used to weighing thrusters contribution different. This will be used later. If there are different thrusters this constant must be determined and accounted for. The optimal speed for the thruster can be found by establishing a function of the propulsion energy in terms of the thruster speed, defined in equation 2.3.26. This is presented in equation 2.3.29.

$$E = (a_1 - b_1x)^2 + (a_2 - b_2x)^2 + (a_3 - b_3x)^2 + (a_4 - b_4x)^2 + (a_5 - b_5x)^2 + (a_6 - b_6x)^2 + x^2 \quad (2.3.29)$$

Rearranging the terms in equation 2.3.29 yields an more simple expression 2.3.30

$$E = (a_1 + \dots + a_6) + (b_1^2 + \dots + b_6^2 + 1)x^2 - 2x(a_1b_1 + \dots + a_6b_6) \quad (2.3.30)$$

The minimal energy is found by setting the derivative of equation 2.3.30 equal to zero. This is done in equation 2.3.31.

$$\frac{dE}{dx} = 2x(b_1^2 + \dots + b_6^2 + 1) - 2(a_1b_1 + \dots + a_6b_6) = A * x - B = 0 \quad (2.3.31)$$

The solution to the optimal thrust allocation problem with respect to minimizing the total energy consumption is found by equation 2.3.32

$$x = \frac{B}{A} \quad (2.3.32)$$

This result can be used in equation 2.3.26, and the thruster speed for each thruster can be computed. After this computation, thruster saturation must be checked.

Thrust allocation - Minimize thruster speeds

When the ROV is moving forward or backwards, it is desirable that the thruster does not direct jets of water in front of the cameras. For this reason a second operating mode can be defined, with a new thrust allocation objective. The objective for the thrust allocation in with this mode is that the thrust allocation problem is solved, and the two thruster in the front have as low speed as possible. Since the objective is to prevent water being flushed in front of the ROV's cameras only negative speed on thruster "1" and "2" must be minimized. In this section three methods to achieve this will be presented. The first method will attempt to determine the minimal thruster speed that solve the thrust allocation problem from the set of linear equations. The second method will use the optimization routine described above, but where the two front thrusters are weighted to reduce their thruster speed. The last approach involve setting one thruster to zero speed, and solve the system as a fully actuated system with six thruster and six DOF's.

Method 1

The first method is based on the system of equation presented in equation 2.3.24. This linear system is rewritten in the form presented in equation 2.3.25. From this it can be seen that the thruster speed for thruster 7, u_7 is a free variable. On the basis of the equation 2.3.24 and 2.3.25 presented earlier the thruster speed u_1 and u_2 can be determined. This is done by finding the minimum value of the objective functions in equation 2.3.33 .

$$\mathbf{O}_b = \min(u_1 + u_2) \quad (2.3.33)$$

The objective function presented in equation 2.3.33 will minimize the sum of u_1 and u_2 . This can however result in one of the thruster having a relative high speed, and the other having a lower. It can be desirable that both thrusters have lower speed, even though the sum can be larger. To achieve this the objective can be augmented, to minimize the sum of the power of speeds. When the power is 2 this method becomes a least square method. This will result in a solution where the difference in the thruster speed is lower. This objective is presented in equation 2.3.34.

$$\mathbf{O}_b = \min(u_1^n + u_2^n) \quad (2.3.34)$$

On the basis of these objective function, the solutions with the lowest values for u_1 and u_2 is selected. If the minimum solution is not unique, a secondary optimization objective is used. This secondary optimization objective is to minimize total propulsion power. On the basis of this the thruster speed can be determined in a similar way as described in section 2.3.6.

Method 2

The second method that can be used to limit the speed on two thruster in the front of the ROV is to apply the same optimization algorithm as described in section 2.3.6, but with some important modification. The thrust allocation is in this method also rewritten in the form in equation 2.3.26. The constant S_i with $i \in [1, 2, 3, 4, 5, 6, 7]$ in equation 2.3.28 is with this approach retained. This parameters is used to weighing the cost of energy for the different thrusters. The optimization problem can be written as in equation 2.3.35

$$E = (S_1a_1^2 + S_2a_2^2 + S_3a_3^2 + \dots + S_6a_6^2) + (S_1b_1^2 + S_2b_2^2 + \dots + S_6b_6^2 + 1)x^2 - 2x(S_1a_1b_1 + S_2a_2b_2 + \dots + S_6a_6b_6) \quad (2.3.35)$$

$$\frac{dE}{dx} = 2x(S_1b_1^2 + S_2b_2^2 + \dots + S_6b_6^2 + 1) - 2(S_1a_1b_1 + S_2a_2b_2 + \dots + S_6a_6b_6) \quad (2.3.36)$$

$$= A * x - B = 0$$

The objective is to select the lowest value of equation 2.3.35. By selecting S_1 and S_2 large relative to the other S_i , the cost of energy from energy from thruster 1 and 2 is said to be large. The result is that a lower value for u_1 and u_2 is selected. The resulting thruster speed for thruster number "7", the free variable, can be determined from equation 2.3.32, and as previously explained. The speed u_1 and u_2 can be determined from equation 2.3.25. The advantage of this method is that the speed u_1 and u_2 are minimized while the overall energy consumption is considered.

Since only negative values at u_1 and u_2 must be avoided, the weights can be set to be equal to the other thrusters, and only increased if the calculated value for the speed would be negative.

Method 3

The last method that will be considered in this project is a more simple approach. To ensure that the speed of one of the two front thruster are low is by setting it equal to zero. To this end the number of thrusters is reduced to six, and the speed u_1 is set to zero. With this approach the thrust configuration matrix \mathbf{T}_{conf} is reduced by eliminating column one. The \mathbf{B}_e is established as presented in equation 2.3.10, and the thruster speed is found by solving equation 2.3.37

$$\mathbf{u} = \mathbf{B}_e^\dagger \boldsymbol{\tau}_c \quad (2.3.37)$$

2.4 System Identification

When a system is analysed, where it is important that the parameters of the system are known, the application of methods from system identification can be useful. System identification involves estimating a model based on the input to the model and the response. For underwater vehicles this can involve estimating the parameters of the model of the movement of the vessel described by 2.2.26, from the input forces $\boldsymbol{\tau}$ and response $\boldsymbol{\nu}$. One possible application of system identification can be as a part of the control system running in parallel with the control loop, where the forces from the controller and the observer states are used to calculate the model of the vessel. This model can either be used to update the vessel parameters used by the control system or as a tool to evaluate whether something have happened to the vessel. For example, if the calculated mass matrix is smaller than the once used in the control system either the once used in the control system is wrong, and should be updated, or the vessel might have lost some weight by loosing an component. Furthermore system identification allows the user to identify the model parameter from the real system, and not from a scale model or computer model. In the following section an introduction to the theory behind system identification will be given. The basic principle will be described for a scalar system. Later these principles are extended to systems in matrix form. This will be concluded by deriving the system identification approach for an ROV, with the modelled described earlier in this chapter.

A generic flow of the process of system identification can be formulated as in figure 2.4.1, [23]. The general procedure can be described accordingly. 1, The existing knowledge of the system is used to formulate an experimental setup where data of the response of the system can be obtained. The prior knowledge of the system is also used to choose the form the model of the system will take. In addition to this a criterion used to select the best model that best fit the data is established. One common approach is the least square method. 2, The experiment is performed, and the input to the system and its response is recorded. This is then used in step 3, which is to calculate a model of the system. One important step in the system identification loop is to verify the model of the system. This is done in step 4, Verification is typically done by using a separate set of data, than the once used to calculate

the model. The response from the real system in this test is compared to the response calculated with the model previously created. If these two correspond well, the calculated model can be used. If there are large offsets, a new iteration in the system identification loop must be performed. This can for example include modifying the form of the model selected. For example, if a quadratic model was selected, and the correspondence in the validation test is poor, the validity of the assumption of a quadratic model should be evaluated, and higher order model might be required.

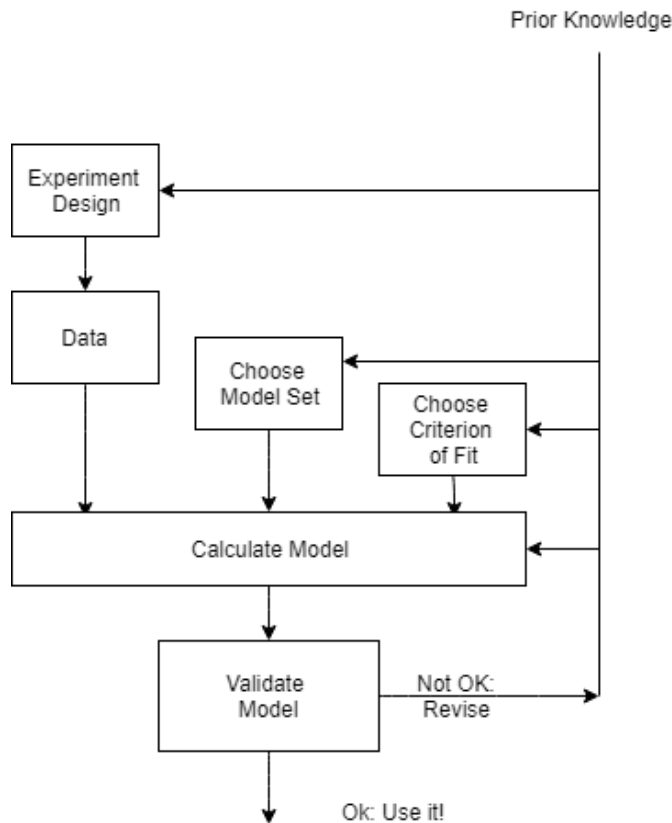


Figure 2.4.1: Generic flow chart of the process of system identification, [23]

For a scalar system described by equation 2.4.1, where the unknown parameters a and b describe the system, the goal of a system identification is to find the values for a and b that best suits the data that have been obtained from the system. The variables x and u are some input to the system, that are measured or recorded. This can for example be the speed of the thruster or the velocity of the body. The output of the model is y . As this is a scalar system the dimensions of the vectors y , x and u will all be $\in \mathbb{R}^{1 \times N}$ where N measurements are recorded. The system parameters a and b is in this case constant.

$$y = ax + bu \tag{2.4.1}$$

Methods of determining the parameters are presented in [23]. The method presented in this section will be primarily based on this. Equation 2.4.1 present the general model of the system. When the data is obtained each value of x and u correspond to a value of y related by a and b . This can be presented by the system of linear

equation presented in 2.4.2. Here the index refers to the measurement number.

$$\begin{bmatrix} y_1 & y_2 & \dots & y_n \end{bmatrix} = \begin{bmatrix} ax_1 + bu_1 & ax_2 + bu_2 & \dots & ax_N + bu_N \end{bmatrix} = \begin{bmatrix} a & b \end{bmatrix} \begin{bmatrix} x_1 & x_2 & \dots & x_N \\ u_1 & u_2 & \dots & u_N \end{bmatrix} \quad (2.4.2)$$

In equation 2.4.2 there are N equations with 2 unknown. This can be solved analytically with two measurement. When there are more than 2 measurement the parameters can be determined with curve fitting. If the proposed model is accounting for all effects, and there is no disturbance or noise the number of measurement will not matter, as a teoretical perfect result can be expected. However all real system will have imperfections and disturbances. Then the more measurement are available the more certain the result will be. The parameters are then found from a linear regression. One common method of doing this is by the least square method, [23]. The scalar formulation of this method can be formulated in equation 2.4.3, [23]. Here a cost function $C(a, b)$ is defined, as a function of the parameters. The least square method involve minimizing the cost function.

$$C(a, b) = \sum_{i=1}^N (y_i - (ax_i + bu_i))^2 \quad (2.4.3)$$

The optimal values for the system parameters are found by partially differentiating equation 2.4.3 with respect to the two parameters, and setting the result equal to zero, as presented in equation 2.4.4. This yield two equations that can be solved, giving the values for a and b that fits the data best.

$$\begin{aligned} \frac{\partial C(a, b)}{\partial a} &= 0 \\ \frac{\partial C(a, b)}{\partial b} &= 0 \end{aligned} \quad (2.4.4)$$

For a linear scalar system the approach outlined above can be used. This method also highlights the fundamental principles that will be used when the system now is on matrix form. A simple system similar is presented in equation 2.4.5.

$$\mathbf{y} = \mathbf{A}\mathbf{x} + \mathbf{B}\mathbf{u} \quad (2.4.5)$$

Equation 2.4.5 is reorganised in equation 2.4.6, to simplify the expression

$$\mathbf{y} = \mathbf{A}\mathbf{x} + \mathbf{B}\mathbf{u} = \mathbf{\Phi}\mathbf{Z} \quad (2.4.6)$$

In equation 2.4.6 the term constituting the system matrices \mathbf{A} and \mathbf{B} is defined as $\mathbf{\Phi} = [\mathbf{A} \ \mathbf{B}]$. The input vector is defined as $\mathbf{Z} = [\mathbf{x} \ \mathbf{u}]$ The matrix formulation of the least square method to find the $\mathbf{\Phi}$ matrix is found according to equation 2.4.7, [10]. The \mathbf{Y} is the measurement matrix containing the measurement \mathbf{y} .

$$\mathbf{\Phi} = (\mathbf{Z}^T \mathbf{Z})^{-1} \mathbf{Z}^T \mathbf{Y} \quad (2.4.7)$$

The system matrices \mathbf{A} and \mathbf{B} is then found from $\mathbf{\Phi}$ in 2.4.7.

System identification can be formulated for an underwater vehicle moving in 6 DOF, described by 2.2.26. There are only two truly nonlinear term in this equation, $\mathbf{C}_A(\boldsymbol{\nu})$ and $\mathbf{C}_{RB}(\boldsymbol{\nu})$. These matrix is however uniquely defined by the added mass, according to section 2.2.2 and 2.2.1. To avoid having to deal with the nonlinear terms, and to keep the simplicity of the linearity the Coriolis and centripetal force from the added mass is found in an iterative manner. The restoring force is also calculated and subtracted in the equation. The equation is formulated in equation 2.4.8.

$$\begin{aligned} \dot{\boldsymbol{\nu}} &= (\mathbf{M}_{RB} + \mathbf{M}_A)^{-1}(\boldsymbol{\tau} - \mathbf{C}_{RB}(\boldsymbol{\nu})\boldsymbol{\nu} - \mathbf{C}_A(\boldsymbol{\nu})\boldsymbol{\nu} - \mathbf{D}_L\boldsymbol{\nu} - \mathbf{D}_q\boldsymbol{\nu}^2 - \mathbf{g}(\boldsymbol{\eta})) \\ \dot{\boldsymbol{\nu}} - (\mathbf{M}_{RB} + \mathbf{M}_A)^{-1}(\mathbf{C}_A(\boldsymbol{\nu}) + \mathbf{C}_{RB}(\boldsymbol{\nu})\boldsymbol{\nu} - \mathbf{g}(\boldsymbol{\eta})) &= (\mathbf{M}_{RB} + \mathbf{M}_A)^{-1}(\boldsymbol{\tau} - \mathbf{D}_L\boldsymbol{\nu} - \mathbf{D}_q\boldsymbol{\nu}^2) \\ \mathbf{Y} &= \boldsymbol{\Phi}\mathbf{X} \end{aligned} \tag{2.4.8}$$

Equation 2.4.8 can be rewritten to equation 2.4.9. The terms dependent on the same input is assembled into the same parameters, defined in equation 2.4.12.

$$\begin{aligned} \dot{\boldsymbol{\nu}} - \mathbf{M}^{-1}\mathbf{g}(\boldsymbol{\eta}) - \mathbf{M}^{-1}(\mathbf{C}_A(\boldsymbol{\nu}) + \mathbf{C}_{RB}(\boldsymbol{\nu}))\boldsymbol{\nu} &= \mathbf{M}^{-1}\boldsymbol{\tau} - \mathbf{M}^{-1}\mathbf{D}_L\boldsymbol{\nu} - \mathbf{M}^{-1}\mathbf{D}_q\boldsymbol{\nu}^2 \\ \mathbf{Y}(\boldsymbol{\eta}, \boldsymbol{\nu}) &= \boldsymbol{\Phi}\mathbf{X} \end{aligned} \tag{2.4.9}$$

The matrix \mathbf{X} is defined in equation 2.4.10 and $\boldsymbol{\Phi}$ is defined in equation 2.4.11. The \mathbf{Y} matrix is defined in equation 2.4.13 These two equation will recreate the system of equation presented in equation 2.4.8.

$$\mathbf{X} = \begin{bmatrix} \boldsymbol{\tau} & \boldsymbol{\nu} & \boldsymbol{\nu}^2 \end{bmatrix} \tag{2.4.10}$$

$$\boldsymbol{\Phi} = \begin{bmatrix} \mathbf{M}^{-1} & \mathbf{M}^{-1}\mathbf{D}_L & \mathbf{M}^{-1}\mathbf{D}_q \end{bmatrix} \tag{2.4.11}$$

Where the term \mathbf{M} is defined in equation 2.4.12

$$\mathbf{M} = \mathbf{M}_{RB} + \mathbf{M}_A \tag{2.4.12}$$

$$\mathbf{Y} = \dot{\boldsymbol{\nu}} - \mathbf{g}(\boldsymbol{\eta}) - (\mathbf{C}_A(\boldsymbol{\nu}) + \mathbf{C}_{RB}(\boldsymbol{\nu}))\boldsymbol{\nu} \tag{2.4.13}$$

One inherent weakness with the proposed method above is that the matrix \mathbf{C}_A and \mathbf{C}_{RB} is not solved directly. This is done to be able to preserve the linear properties of the system. An alternative is to introduce some more complex nonlinear system identification method. In order to calculate the matrices in equation 2.4.11 the matrices in 2.4.10 and 2.4.13 must be determined. Now the \mathbf{Y} is not measured directly, only the acceleration $\dot{\boldsymbol{\nu}}$. The term $\mathbf{g}(\boldsymbol{\eta})$ can be calculated with the known values for $\boldsymbol{\eta}$. The Coriolis and centripetal forces is described by the $\mathbf{C}_A(\boldsymbol{\nu})$ and $\mathbf{C}_{RB}(\boldsymbol{\nu})$ matrix and is defined by equation 2.2.19. This matrix can be determined when the added mass and velocity is known. However the purpose of the system identification is to determine the added mass. A simple solution is to apply some starting estimate for the added mass. This can be used to calculate the \mathbf{Y} vector by equation 2.4.13. The system identification can be performed by the least square method, and the added mass is found. This added mass can then be used to calculate a new \mathbf{C}_A and thus a new \mathbf{Y} . This is then an iterative process that will give

updated estimate for the system parameters Φ .

System identification can be implemented in different ways for a motion control system. One approach, is as presented in [22], where data from a mission is processed after the mission, to identify errors in the ballast. The result is used to make corrections before next mission. With this approach the system identification does not run as a part of the control system but as a post processing tool. Another approach is to integrate system identification in the control system. For practical purposes only a certain number of data point should be used, for example the last 1000 data points. The resulting model can be used by the control system online to improve the performance. If the later approach is selected care should be taken to ensure that this does not cause delays in the system. As presented in equation 2.4.7 the solution is obtained by inverting matrices, which is a computational expensive calculation. One solution could be to have the system identification run on a separate thread, and thus not directly interfering with the control system but only exchanging data between the two systems. This also highlights the advantages of the approach selected in [22]. One approach for ROV operations can be to run a pre-mission test where data is recorded for the current configuration of the ROV. Before the real mission is started the system identification is performed on the pre-mission data, and the model is determined and used in the real mission. With this approach the benefit and the disadvantages of the online calculations is lost.

Chapter 3

Method

In this chapter the methods used to calculate the hydrodynamic coefficients, and to design, implement and develop features of the control system will be presented. Firstly the hydrodynamic part will be treated in section 3.1. The experimental procedure will be outlined in section 3.1.2. Section 3.1.1 will present the method used to determine the added mass and damping and how these values were verified. Implementation of the system identification is presented in section 3.2. The remaining part of this chapter will cover the developments made to the ROV control system, and is presented in section 3.3.

3.1 Establishing Hydrodynamic Coefficients

The hydrodynamic coefficients will be determined with two methods. Experimental tests performed at the MC-labb at NTNU will be used to determine the added mass and damping coefficient for a scale model of the ROV. In addition to this computational tools will be used to calculate the added mass and damping for the full scale ROV

3.1.1 Numerical

The added mass and damping coefficients M_A , C_A , D_L and D_q can be found with numerical methods using the programs Wadam (potential flow tool) and Solidworks Flow Simulator (CFD), presented in section 2.2.2. The plan to establish the hydrodynamic parameters were to first create a simplified CAD model of the ROV, on the basis on the CAD model for the real vessel. The model of the ROV is then converted to a panel model and meshed using the software GeniE. This program was used since both programs are a part of the DNV-GL SESAM package. Because of this the interface between the two programs are designed to be easy to use, which is a great benefit. The meshed model from genie was imported in HydroD, which is the program that runs the Wadam analysis. The output from this program was the calculated added mass of the model. The same model that was created in Solidworks was also used for the CFD analysis. It would be technically possible to use the non simplified model, but this would lead to the added mass and damping not being consistent. In Solidworks the model was opened in the Flow simulation tab, where the CFD analysis was performed. From this the forces on the ROV was

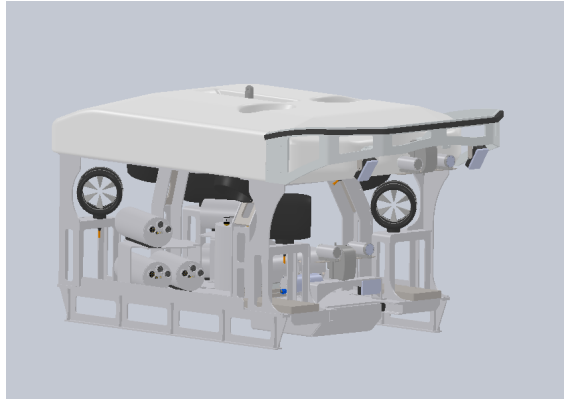


Figure 3.1.1: CAD model of the real ROV.

calculated with current flowing in on the vessel, and the corresponding current velocities was recorded. On the basis of this the hydrodynamic parameters was found. In the following sections the procedure will be detailed further.

Modelling the ROV

The ROV was modelled using the CAD tool Solidworks. This was selected since the tool is relatively simple to use. In addition to this, Solidworks have several add-on packages to the software. One such add-on is the Solidworks Flow Simulator, which is a CFD program, that allow for fluid dynamical analysis of a CAD model. A CAD model of the ROV Minerva 2 was provided by the manufacturer. This model was used as a basis to create a simplified model of the ROV. This was necessary since the panel model in Wadam require all surfaces to be straight. To achieve this circular cylinders was modelled as extruded octagon, and curved surfaces was modelled as several flat surfaces. Furthermore Wadam is limited to 20,000 elements in the analysis, [13], and in order to get a well refined mesh, it was necessary to simplify the geometry of the ROV. One challenge with this is that the geometry of the ROV is relatively complex, something that affects the added mass and damping.

The result was a simplified model of the ROV, where curved and circular shapes had been flattened out, and the geometry had been simplified. In doing this care had been taken to retain as much as possible of the larger features of the vessel. It was attempted to ensure that the inside of the framework of the ROV would have similar density of components, i.e. the same projected area. Figure 3.1.2 presents the simplified CAD model of the real ROV, while figure 3.1.1 is the modelled simplified ROV.

In the two figures 3.1.2 and 3.1.1 it is clear that there are some noticeable differences, but the general shape of the ROV is preserved, and the simplifications make it possible to perform a analysis of the vessel. This was done by measuring the relevant part in the "real" model, and drawing each individual part. The drawn parts was then extruded to create the solid parts. When all relevant parts was created an assembly was created, and the parts was mated together to form the finished assembled model.

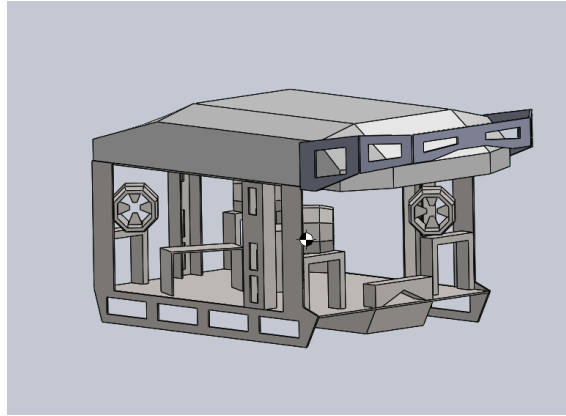


Figure 3.1.2: Simplified CAD model of the ROV, used for the hydrodynamic computations.

Added mass

The added mass was calculated using the software Wadam, as earlier mentioned, which is a analysis tool that runs in the HydroD program. Wadam performs an hydrodynamic analysis of a discretized model (meshed model). The software is used to calculate the wave-structure interaction for fixed or floating structures. The program is based on Morrison formulation to account for drag forces and diffraction radiation methodology, as presented in section 2.2.2, [34]. In order to perform the analysis the CAD model developed in Solidworks must be meshed. This can be done using the program GeniE. This program is together with HydroD and Wadam a part of the DNV-GL developed SESAM package. The benefit of using GeniE over other software's capable of meshing a model is that the meshed model can easily be imported to HydroD.

The CAD model from Solidworks is imported to GeniE as a ".sat" file. The first step in meshing the model is to define the necessary parameters such as thickness of the plates, density, wet surface and mesh detail. A dummy hydrodynamic load is applied to the vessel before the model is meshed. The mesh size was defined small enough to accurately represent the geometry of the geometry, but not exceeding the limit of 20000 elements. An element size of $0.05m$ was selected. Figure 3.1.3 shows the mesh of the ROV.

The ROV is meshed using two different super element types. Superelement number 1 is used to mesh the ROV to create the panel model. This element type is used to define the geometry of each element. When the model is meshed using this element type the panel model is obtained. Superelement number 3 is used to generate a mass model of the ROV. This file will contain information about the mass and mass distribution of each element of the model. Although the hydrodynamic mass and damping is not depended on the real mass, the mass model is used for the computation in GeniE.

The meshed model is exported from GeniE as a ".fem" file. The added mass is then found by creating an analysis using HydroD. Here an environmental model is created defining a set of wave frequency and wave directions, along with properties of the water and the wave height. As presented in section 2.2.2, the added mass

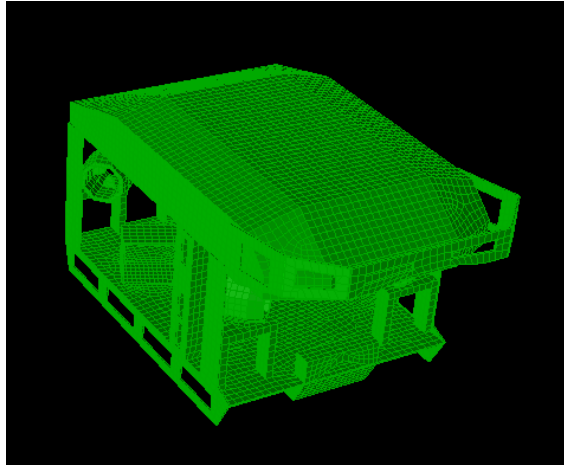


Figure 3.1.3: Model of the ROV that have been meshed using GeniE.

relevant for an underwater vehicle at deep water is independent of wave action, for this reason the water depth is defined as a 300 meters, to represent an ROV operating at deep water. The wave height is set to be zero meters. The model of the geometry of the ROV is loaded in HydroD and the depth of the ROV is defined. This is set to be 150m to ensure that the ROV is operating at deep water. After the analysis is defined this is executed using the software Wadam. The output from this is resulting added mass and damping and motion for the different frequencies defined in the analysis. A verification of the procedure was performed by performing an analysis in HydroD/Wadam of a simple geometry and comparing with empirical data, in accordance with the procedure presented in section 2.2.2.

When the depth of the ROV was defined in Wadam, the default computation would be relative to the sea surface. This would give a large radius of gyration. The radius of gyration is the distance from the body that is rotating to the coordinate system. For the computation the output would be required to be relative to the centre of gravity, not the sea surface. In order to correct this a new output coordinate system was defined in the COG.

Damping

The damping found from HydroD can be neglected since the potential damping without wave radiation will be zero, as presented in section 2.2.2. To determine the damping of the ROV the nonlinear damping due to skin friction and vortex shedding must be determined. These can be modelled as a linear and a quadratic terms as presented in equation 2.2.25. This can be determined by using CFD programs. One such tool is the Solidworks flow simulator. Since the ROV was modelled using Solidworks CAD tool, it was beneficial to use the integrated CFD tool in the software. The CAD model was loaded into the Flow simulator add-on. The environment and fluid parameter was firstly defined. The desired velocity of the flow was then defined. The goals of the analysis was defined as calculating the real velocities and the forces and torque acting on the ROV. Lastly a mesh was defined, and the refinement level was selected. Here the mesh represent volume cells. The mesh function in soldiworks works by selecting a level of refinement. The size of the individual mesh volumes

are not constant but more detailed where it is necessary, and larger further away from the model.

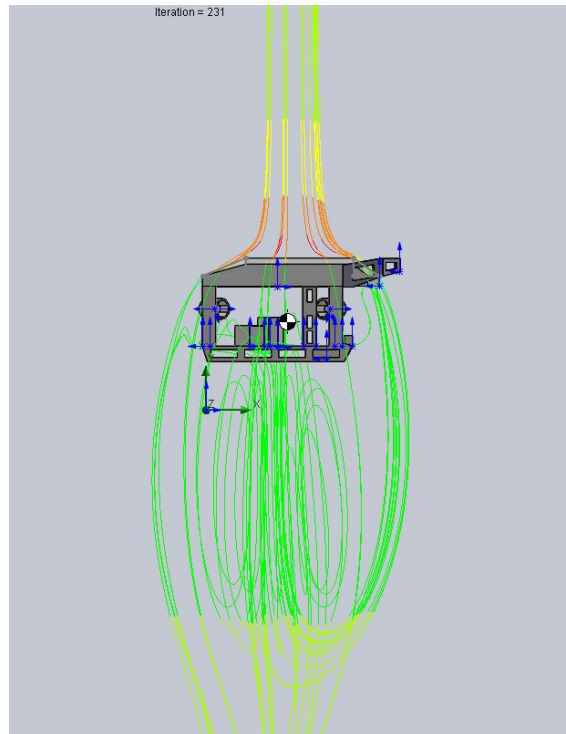


Figure 3.1.4: Illustration of the flow lines around the flotation block from a current flowing from above.

Figure 3.1.4 show the result of a CFD analysis where flow is coming from above. Flow lines around the flotation block is illustrated. The result of the CFD analysis is an excel sheet with the velocities and the forces acting on the vessel. On the basis of this the damping can be calculated using equation 2.2.34 when the added mass is found using HydroD/Wadam. For the CFD analysis Coriolis and centripetal forces will not be present. Furthermore, since the flow have a constant velocity, the mass forces will be zero. The result is that equation 2.2.34 only have two unknown, the matrices \mathbf{D}_L and \mathbf{D}_q , that can be calculated. As presented in section 2.2.2, the two matrices are diagonal matrices, where all non diagonal terms are zero. This means that all DOF's are uncoupled. The coefficients in the matrices can be found by performing a set of CFD analysis for different velocities ν , and determining the values of the coefficients by a least square curve fitting of the result. Verification of the result from the CFD are performed by analysing a simple geometry in solid works and comparing with empirical data.

The procedure for determining the hydrodynamic coefficients are summarised in the flow chart presented in figure 3.1.5. The left hand side of the figure present the steps of the procedure used for the added mass, while the right hand side presents the damping. Both analysis is seen to originate from the model of the ROV.

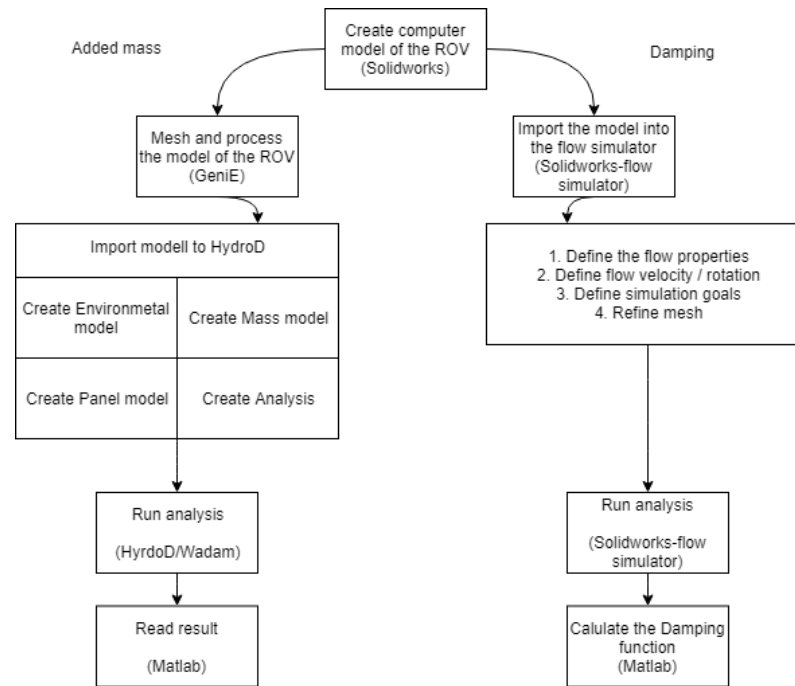


Figure 3.1.5: Flowchart of the hydrodynamic analysis

Verification of numerical methods

Translational added mass found for a cube geometry, and the 3D added mass is determined from table data in [39], presented in appendix A. Rotational added mass is found by determining the two dimensional added mass, and applying strip theory to determine the 3D added mass for the body. This is compared to the results obtained for an identical geometry using numerical tools.

A cube with sides equal to $2m$ is created using the CAD software Solidworks, and the meshed cube is presented in figure 3.1.6. The procedure for determining the added mass above is used, and the added mass matrix is obtained. The added mass of this cube is also determined by identifying the added mass coefficient C_A for the body. Since all sides have length $2m$ the fraction becomes $\frac{b}{a} = 1$ for all three translational directions, which is used to find C_A in the table. From this the three dimensional added mass is found for all three translational DOF's by using equation 2.2.30. In addition to this the added mass is determined for the cube by considering the two dimensional added mass for a square cross-section of the cube, and determining the added mass by strip theory according to 2.2.21. The two added masses are used to create a scaling factor λ between the strip theory result and the empirical data. On the basis of this the rotational added mass is calculated using equation 2.2.32.

A similar verification test is performed on the CFD analysis, to ensure that the quality of the result is acceptable. For generic shapes the drag coefficient can be found according to [3] for given geometrical relations and reynolds number. The Reynolds number can be calculated using equation 2.2.24. From [3] the drag coefficient C_D is determined for a circular cylindrical rod. The drag coefficient is found for a case where the flow is coming in sin the direction of the length of the rod. Figure 3.1.7 presents the scenarios.

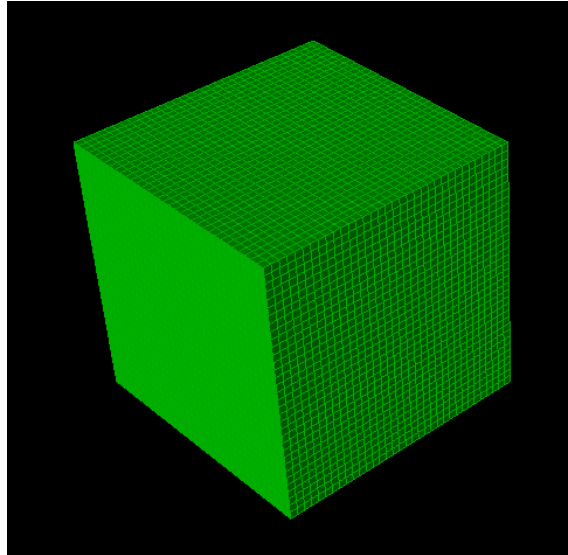


Figure 3.1.6: Reference cube meshed in GeniE.

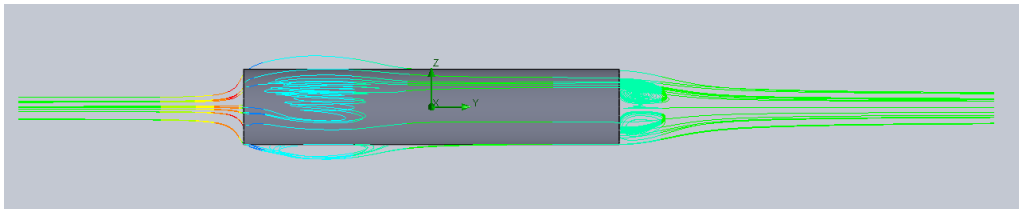


Figure 3.1.7: Flow around the reference cylinder /rod.

A CFD analysis was performed for the case presented above, where the forces was the output from the analysis. From this equation 2.2.23 was used to calculate the drag coefficient. In order to have comparable result, the reynolds number need to be identical for the CFD and the table value in [3]. These table values are found for reynolds number at $R_N = 8.8 \times 10^4$. For a rod with dimensions: diameter $D = 0.1m$ and length $L = 0.5m$ and the kinematic viscosity $\nu = 10^{-6}$, the flow velocity u can be calculated. The flow velocities is found to be $u = 0.176[m/s]$.

3.1.2 Experimental Test

An experimental test was performed on a scale model of the ROV Minerva 2. The ROV was created at a scale $\lambda = 1 : 6$. The experiments were to be performed at the Marine cybernetics laboratory (MC-lab). The scale model was manufactured by first creating the framework of the ROV. This was created in aluminium. The flotation block was created from divynycell. The internal components was created from wood and from divynycell. The resulting scale model of the ROV is presented in figure 3.1.8.



Figure 3.1.8: Picture of the scale model of the ROV used for the experiment.

The setup in the laboratory did only allow for planar motion, that is motion in surge, sway and yaw. Some significant modifications would have to be made in order to test the heave, pitch and roll motion. Due to the limited time that was available in the laboratory, such modifications was not made, and only the horizontal motions was tested. The experimental setup in the laboratory consisted of a mounting bracket mounted to the towing cart. At the bottom of this mounting bracket was the ROV fastened. The mounting bracket used in this experiment was build for the experiments presented in [13]. Figure 3.1.9 illustrate the mounting bracket, and figure 3.1.10 show a picture of the experimental setup were only the mounting bracket is tested. Figure 3.1.11 shows a picture of a towing test of the mounting bracket.

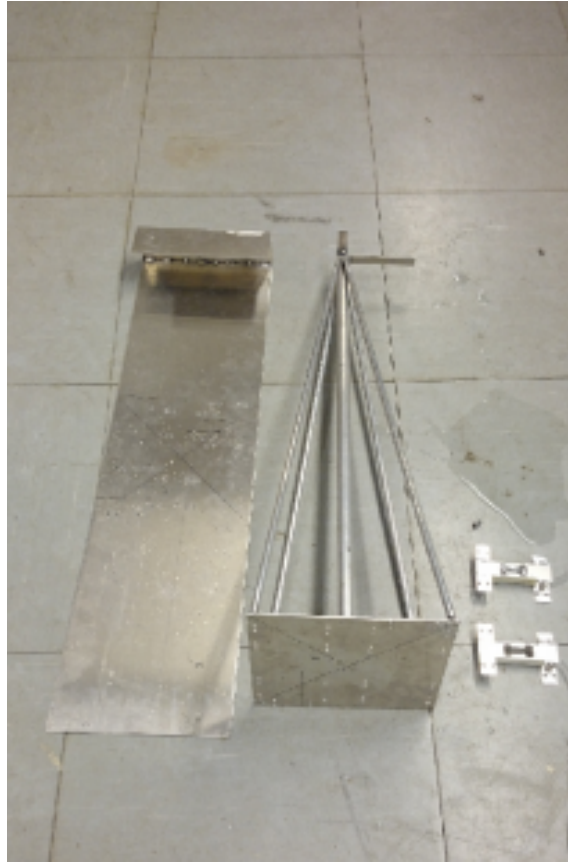


Figure 3.1.9: Picture of the mounting bracket, [13]



Figure 3.1.10: The experimental setup of the test performed in the MC-Lab.

Ideally the ROV and the mounting bracket would together be neutrally buoyant. This was in practice not possible, and the force sensors would therefore also measure the torque as well. Moreover the total system was positive buoyant. Small roll and pitch angles could therefore introduce roll and pitch moments that could pollute the force measurement. To limit this effect the model was fastened to not allow for roll and pitch motion. The since the ROV have port-starboard symmetry, surge motion should not create any sway force or yaw moment. Since force sensor nr.1 was mounted to measure forces in the surge direction and nr.2 was placed in the sway direction, all the surge force would be measured by sensor 1. Although the ROV does not have perfect for-aft symmetry, a similar assumption was made for the sway force. The ROV was mounted as close as possible above the centre of gravity. Any offset fto the COG can introduce moments, that can corrupt the force measurements.

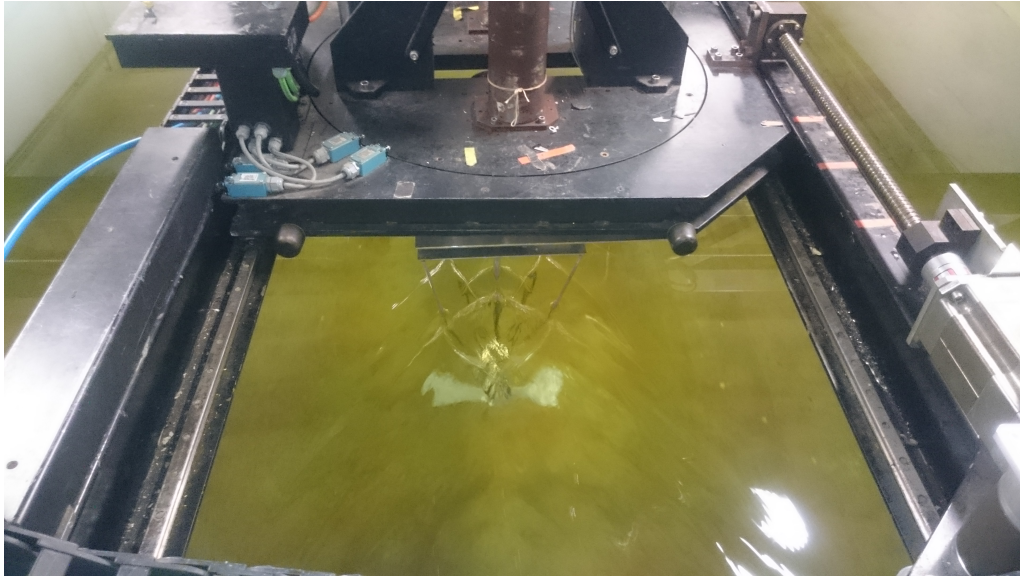


Figure 3.1.11: Towing test performed on the mounting bracket as a reference for the experiment.

The experiment was performed by first running a calibration test, where only the bracket was present. Here the forces on the mounting bracket could be established. It was assumed that the forces on the bracket and the ROV could be linearly superimposed. The first run with the towing carriage was performed with the mounting bracket, but without the model of the ROV. This was done for velocities from $0.1 \frac{m}{s}$ to $1.2 \frac{m}{s}$, with an increment of $0.1 \frac{m}{s}$. On the basis of this the damping function for the bracket was determined. Similarly, rotation of the bracket was performed with a velocity range from $1 \frac{deg}{s}$ to $20 \frac{deg}{s}$. In order to calculate the contribution of the mounting bracket to the added mass, towing runs were performed with accelerations both for surge and for yaw. With the result from the towing test of the mounting bracket, a zero-point could be created, and the contribution from the mounting bracket could be subtracted from the forces measured when the ROV was towed.

In the towing test the ROV was moved in three DOF's. This included surge and sway direction, and rotation in yaw. Figure 3.1.12 illustrates the experimental setup when the ROV was tested. The ROV was tested with the same velocity range as for the mounting bracket. Between every towing run the force sensors were recalibrated so they started with a measurement of zero newton before the towing cart was moving.

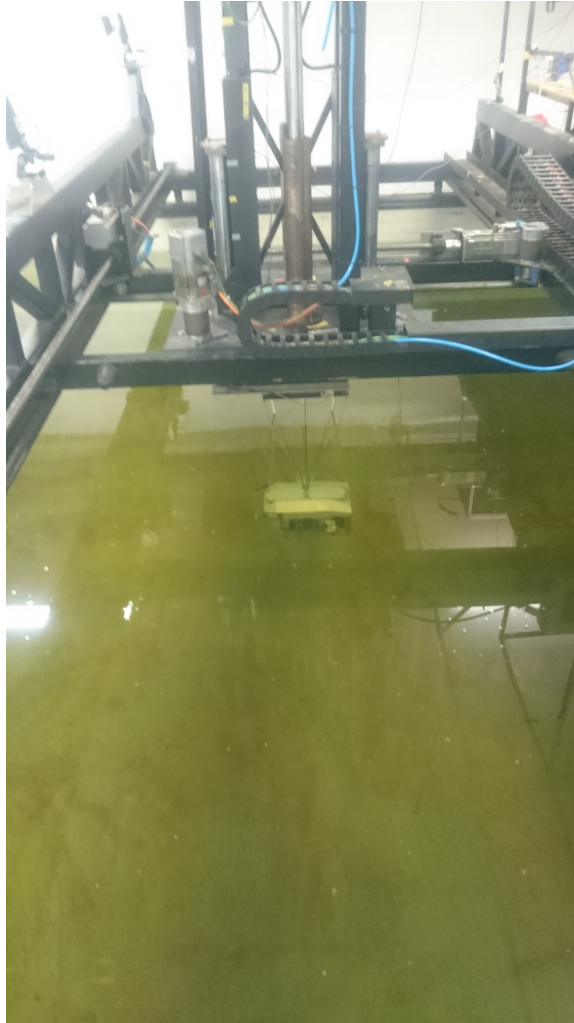


Figure 3.1.12: The experimental setup of the test performed in the MC-Lab.

With the measured force on the ROV at different velocities, the damping function could be created using a least square curve fitting to the data. The damping is determined when the towing is performed at a constant velocity. For a small scale model, the Coriolis and centripetal force on the model, and on the added mass of the body can be neglected. Furthermore, for this test where the model is installed with a zero degrees roll and pitch angle, and the body is held in place in the vertical direction, no restoring forces will act on the ROV in surge, sway or yaw. Therefore at constant velocity there will only be drag / damping forces acting on the model. From this the damping function can be established. From the test where the model was accelerated through the water the added mass force is determined. The damping is calculated with the damping function, and subtracted from the measured forces. This yields the added mass forces. A least square curve fitting of the added mass force can be used to obtain the added mass coefficients.

In order to perform the calculation of the added mass coefficients and the damping force, the forces on the model and the mass of the model must be scaled. The scaling of these parameters are scaled according to equation 2.2.36 and table 2.2.1, presented in section 2.2.4.

3.2 System Identification

System identification will be a new feature for the ROV control system. In this thesis a foundation for this work is done, and test that can serve as a proof of concept is performed. The idea behind the system identification is that a the mathematical model of the system can be established for the relevant modification of the ROV. ROV's can be fitted with extra cameras, manipulators and other forms of payload. Instead of running a separate hydrodynamic analysis for the relevant modification of the ROV, the model can be calculated on the basis of input (thruster speeds) and response (motions and accelerations). It is proposed that an efficient design would be to introduce a function in the control system that the user can activate. When this is done the ROV will run some reprogrammed program where all DOF's are exited, for a given period of time. After this is done the collected data is used in a system identification routine based on equation 2.4.7 and the formulation of the system in 2.4.10, 2.4.11 and 2.4.13. The user can be prompted in the GUI, with a question whether the mathematical model of the system should be updated or not. After this the mission can be performed as usual.

This thesis will focus on the feasibility of such a function for the system, and attempt to create a starting point for such a feature in the ROV motion control system. A system identification program was created in Matlab. This program was based on the approach outlined in section 2.4. Three simulations was performed to test this approach. The first two simulation was done based on a simplified simulation created in Matlab using Simulink. The difference of these two simulations was the complexity of the model. The purpose of this is to see how the introduction of the nonlinear terms effect the system identification performance. The simulation in Simulink is exclusively based on providing some control input to a mathematical model of the system. The test was performed by running a simulation of a system with a defined mass, damping etc. The output from the system, i.e the motion and acceleration together with the forces was used in the system identification program to calculate the model parameters. Lastly the calculated model parameters was compared to the once used for the simulation. The first simulation, hereafter called simulation A

$$(M_{RB} + M_A) \dot{\nu} + (D_l + D_q \nu) \nu = \tau \quad (3.2.1)$$

The second simulation performed in simulink, called simulation B, is based on the more complete version of the equation of motion for the ROV, presented in equation 3.2.2. The only term that is not modelled is the restoring force. This term is not nonlinear with respect to ν , and it was therefore considered as not problematic to exclude this term. This is equivalent to saying that the modelled ROV is neutrally buoyant, with COG and COB coinciding.

$$(M_{RB} + M_A) \dot{\nu} + (C_{RB}(\nu) + C_A(\nu)) \nu + (D_l + D_q \nu) \nu = \tau \quad (3.2.2)$$

The last simulation was performed using the ROV HIL simulator called Verdandi. The control system was used to simulate a tracking mission. While this was running the desired values for pitch and roll was varied, together with motion in heave. The log file from the simulator was used in the system identification program. One

significant benefit of the simplified simulations in Simulink is that it is possible to freely control all degrees of freedom for the vessel. Furthermore the forces in this simulation is based on the real states, and not some observer states, as the case for the HIL simulation is. The system identification program is attached in appendix F.

3.3 Development of the ROV Control System

The ROV control system developed at NTNU is developed on the platform LabVIEW. This is a platform for used for visual programming. LabVIEW consist of a front panel, presenting the inn and output and can function as a GUI, and a back panel where the code is in form of a block diagram.

The control system consist of three projects. The GUI, called Frigg. The HIL simulator called Verdandi and the control system itself called Njord. The development of the control system for Minerva 2 have included work in all of these projects. In the remaining part of this chapter the work done in these programs will be presented.

3.3.1 Control System

The main contribution this thesis provide to the control system is the thrust allocation system. Much of the work done in the control system could be based on existing code, and making necessary modifications. On the other hand the thrust allocation was designed from scratch. The reason for this that the new ROV would have a different number of thrusters, and the thrust allocation had to be solved in a new method. In addition to the thrust allocator work have been performed with adapting the controllers and allowing for more DOF's to be handled by the controller. In addition to this modification to the communication between the control system, Njord, and the HIL software, Verdandi, or the ROV when that is used have been updated.

Controller

The control algorithm that the controller is based on is presented in equation 2.3.1. The previous iteration of the control system implemented this algorithm for four DOF's. This is based on the input the estimated state and the desired states. To accommodate control of pitch and roll motion an input that allows the user to define a desired roll and pitch angle have been established. The current version of the control system allows the operator to manually select these values, where the default value is zero. This was implemented because for most mission it is desirable to have as little as possible effect from the roll and pitch motion, and thus maintaining a zero degree pitch and roll angle is optimal. The implementation allows for an easy connection to the guidance system so that if necessary the desired roll and pitch can automatically be calculated. This can become useful if a future iteration of the control systems implement a function that allow the ROV to maintain an attitude so that the ROV moves perpendicular to the seafloor, as outlined in [27], where the

pitch and roll motion also can be controlled.

Roll and pitch was introduced into the controller by expanding the existing nonlinear PID controller, described by equation 2.3.1. The tuning parameters was found by tuning. For these DOF's a fast controller was not required, but instead a slow and controlled motion was desired. To this end large damping was prioritised by selecting a high derivative term.

Communication

The communication between the different systems are essential. This communication involves sending the calculated thruster speed, receiving the measurements and other variable being transferred between the system. The communication is based on Transmission Control Protocol (TCP) and User Datagram Protocol (UDP) communication and Field-programmable gate array (FPGA). The purpose of the HIL simulator is that the control system can be connected to either the ROV or the HIL simulator with the same communication. To achieve this the communication format between the Njord and Verdandi must be equal to the signals sent from Njord to the ROV. With the new ROV, more thruster signals are sent to the ROV, and a new format of sending the information have been programmed. This have also included a new system for reading this message in the HIL simulator.

Thrust Allocation

The thrust allocation system is designed and presented in section 2.3.6. The thrust allocator was designed and developed in a project work leading up to this thesis. As presented in chapter 2 the purpose of the thrust allocator is to convert the calculated thrust to a set of thruster speeds that are applied to each individual thrusters. Since the system is over-actuated an infinite number of solutions existed and is defined by the intersection \mathfrak{N} of equation 2.3.17-2.3.22. A prototype of the thrust allocator were developed using the programming tool MATLAB. Here all three methods described in section 2.3.6 were implemented and tested. The result from this is presented later in section 4.2.1. On the basis of these test of the prototypes the two variations of the thrust allocation denoted "Thrust allocation - Minimize energy" and "Thrust allocation - Minimize thruster speeds". The default method for thrust allocation is set to be the minimize thruster speed method. The thrust allocation is implemented as a separate "vi", which is a block / function in the LabVIEW environment.

The thrust allocation takes the thrust from the controller as input along with the maximum thruster speed, thrust configuration matrix and the thruster coefficient matrix K defined in an configuration file. The thrust allocation "vi" relies on several sub "vi's" that perform sub-tasks such as formulation the system on the form in equation 2.3.25 or to calculate the thrust by minimizing energy. After the thruster speed have been calculated, a check to ensure that the calculated speed is within the valid thruster speed range is performed. The last action performed in the thrust allocation is to calculate the thrust that correspond to the calculated thruster speed. The difference between these constitute the error in the thrust allocation. This is

calculated to give the user a potential tool to identify any problem with the system. The largest contribution to the error will be due to saturation constraints.

The thrust allocator was tested in two rounds. Firstly the three methods of operation presented in section 2.3.6 was simulated with the same thrust input in a Matlab simulation. In this test method two, minimizing the weighted energy of the propulsion, was tested with three sets of values for the weighing parameters S_1 & S_2 . One of the sets did not have increased values of the S weights, and the S values was kept at unity. The second test consisted of had $S = 10$ for negative speed on thruster 1 and 2. Lastly set three had $S = 10^8$. This aimed to force a solution that prevented negative speed on thruster 1 and 2. On the basis of the result a comparison of the performance was made. In order to test one of the more challenging situations the desired thrust in sway was increased so that the front thruster inevitable had to provide a thrust, causing water to be flushed in front of the cameras. This scenario was tested to see how this special function of limiting this effect work. In addition to this a test was performed where the values for the weighing parameters S for negative thrust for thruster 1 and 2 where reduced. A test of the performance of the thrust allocator was also performed after it had been implemented in the control system. This aimed to ensure and show that the implemented thrust allocation system was working as intended. These test was performed on the control system as a whole and for the control system to function together, the thrust allocator had to function.

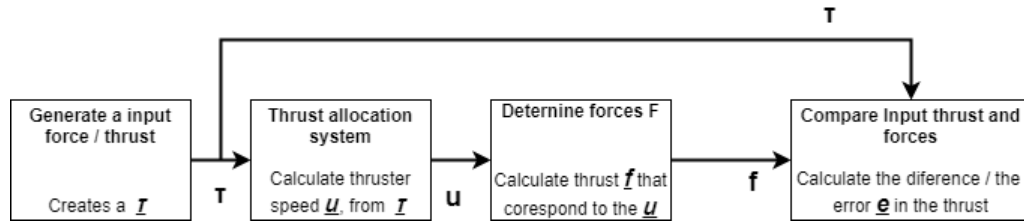


Figure 3.3.1: Flowchart illustrating the simulation of the thrust allocation.

The simulation of the thrust allocation is performed by providing a simulation thrust input. This thrust input is not generated by any controller, but rather as a pure input signal to test the system. Figure 3.3.1 present a simple flowchart of the simulation. The process in the figure is repeated for a predetermined number of iteration constituting a time interval. The performance of the different methods for thrust allocation could be assessed with respect to energy, modelled by equation 2.3.28. In order to obtain a valid comparison the energy must be modelled identically for all approaches, and thus all values of S_i is set to unity. In addition to this the sum of the negative contrition can be used to create a indication of the performance. The performance indicator (PI) of the system is described by equation 3.3.1

$$PI = \begin{cases} |u_1 + u_2| & \text{if } u_1 < 0 \ \& \ u_2 < 0 \\ |u_1| & \text{if } u_1 < 0 \ \& \ u_2 \geq 0 \\ |u_2| & \text{if } u_1 \geq 0 \ \& \ u_2 < 0 \\ 0 & \text{if } u_1 \geq 0 \ \& \ u_2 \geq 0 \end{cases} \quad (3.3.1)$$

3.3.2 HIL

The HIL simulator was updated to use the model of the new ROV. This include defining a new thrust configuration matrix and mathematical model as presented in chapter 2. The rigid body mass and centripetal and Coriolis matrix M_{RB} and C_{RB} for the new ROV are implemented in the HIL system. The hydrodynamic parameters determined by the hydrodynamic analysis is also updated in the HIL simulator and used for the model plant. The thrust coefficient matrix K is also defined in the HIL simulation. The communication between the control system and the HIL is as mentioned also updated.

The HIL simulator was used to test and verify that the control system was working as it was supposed to. Multiple simulations was performed, both with and without disturbances to the system. The HIL simulations are performed by defining a path or waypoint for the ROV to move to. The simulation allows for environmental parameters to be defined by the user, so that different scenarios can be tested.

3.3.3 GUI and Autonomy

The GUI is mainly left the same as for the previous iteration of the system. However the autonomy framework which is part of the GUI have been updated. The system developed in [32] have several empty functions, that in this iteration of the system have been filled. In [32] several mission states were defined, such as; launch, descent, transit, sonar tracking, camera tracking etc. In addition to this a system to determine which state the ROV is in exist, in the system. The function of sonar tracking and camera tracking have been developed in the master thesis of [9] and [41] respectively, who have worked parallel with the author of this thesis. Together a system where the position of the vessel and the state of the vessel are sent to the program where sonar tracking is running. This is sent over UDP link. Similar communication exist with the camera tracking program. These systems return several way points for the ROV. This is read into the autonomy system developed in [32], where a function to create a DP message from this way point that is then sent to the control system.

3.4 Testing of Control System

The ROV control system was tested by using the HIL simulator, together with the control system. The control system have a function that switch between the real ROV and the HIL simulation. When the real ROV is used, the communication is handled over FPGA. When the HIL simulator is used, TCP is used to transmit data between the two systems. In addition to the control system and the HIL simulator the user provide input, and define mission objectives in the GUI. The test of the control system will thus include all three programs. A feature of the control system that will also be tested is the Autonomy code developed in, [32]. This feature is controlled by a separate interface that is activated from the GUI. Figure 3.4.1 and 3.4.2 presents the GUI and the interface of the autonomy code that the user will see during when the control system is used.

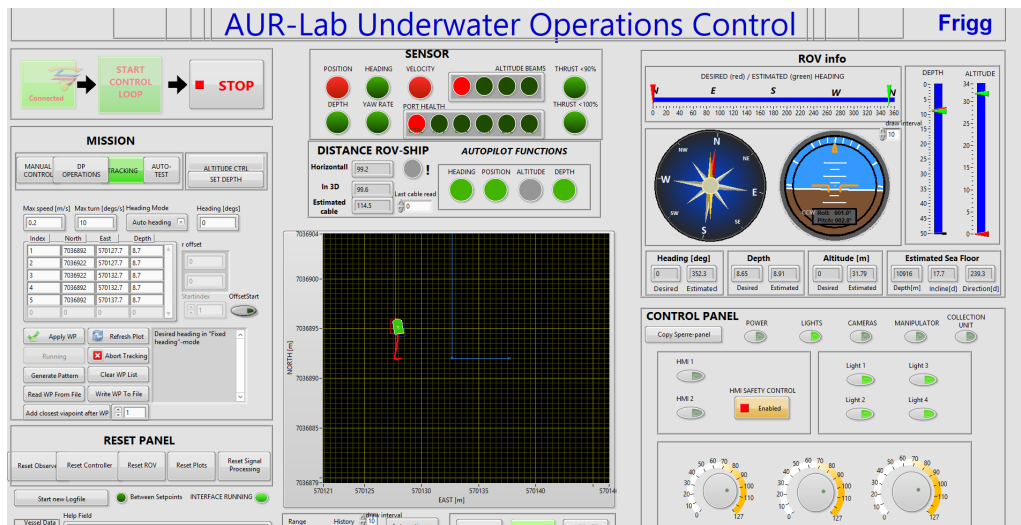


Figure 3.4.1: Graphical user interface of the control system, "Frigg".

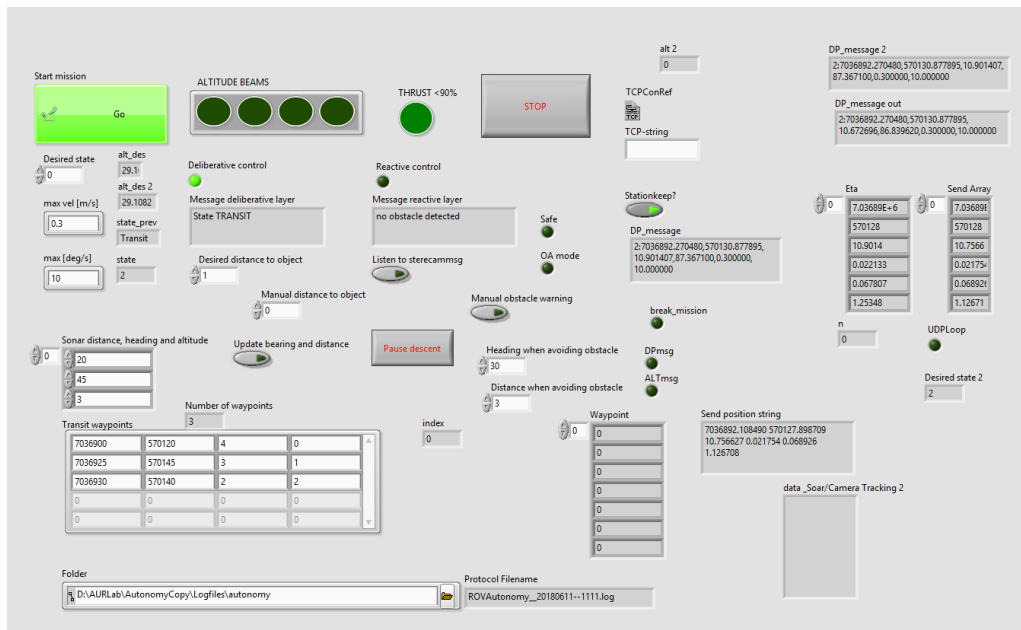


Figure 3.4.2: Interface of the autonomy system.

The user will operate the control system from the GUI and the front panel of the autonomy code presented in figure 3.4.1 and 3.4.2. In addition to this the control system will run in the background. The front panel of the control system is presented in figure 3.4.3, and mainly contain information about the status of the control system, and any potential errors messages are presented here.

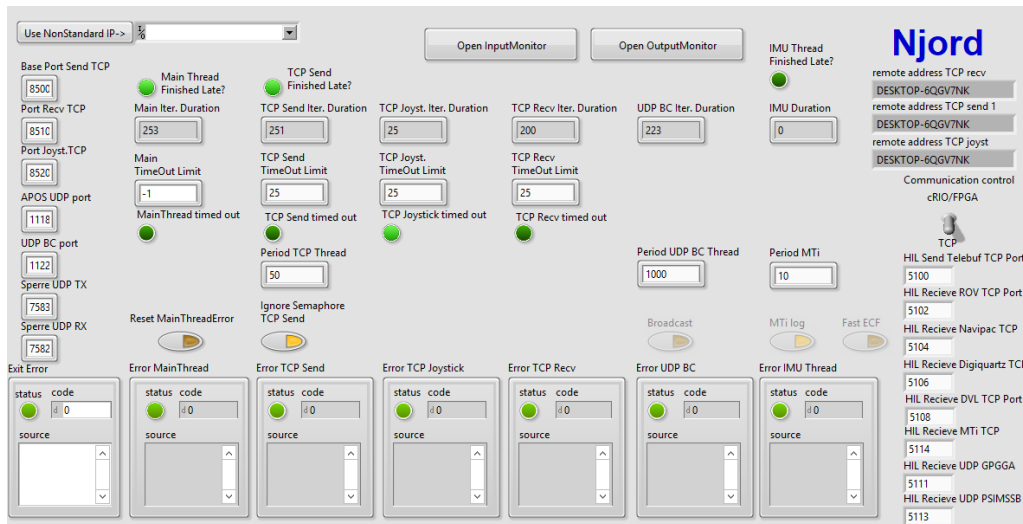


Figure 3.4.3: Front panel of the control system, "Njord".

The control system is tested with the HIL simulator. The interface for this program is presented in figure 3.4.4. Here the user can control the environmental parameters for the simulation or the vessel parameters to mention some. When the real ROV is used, Verdandi will not be used, and will be disconnected.

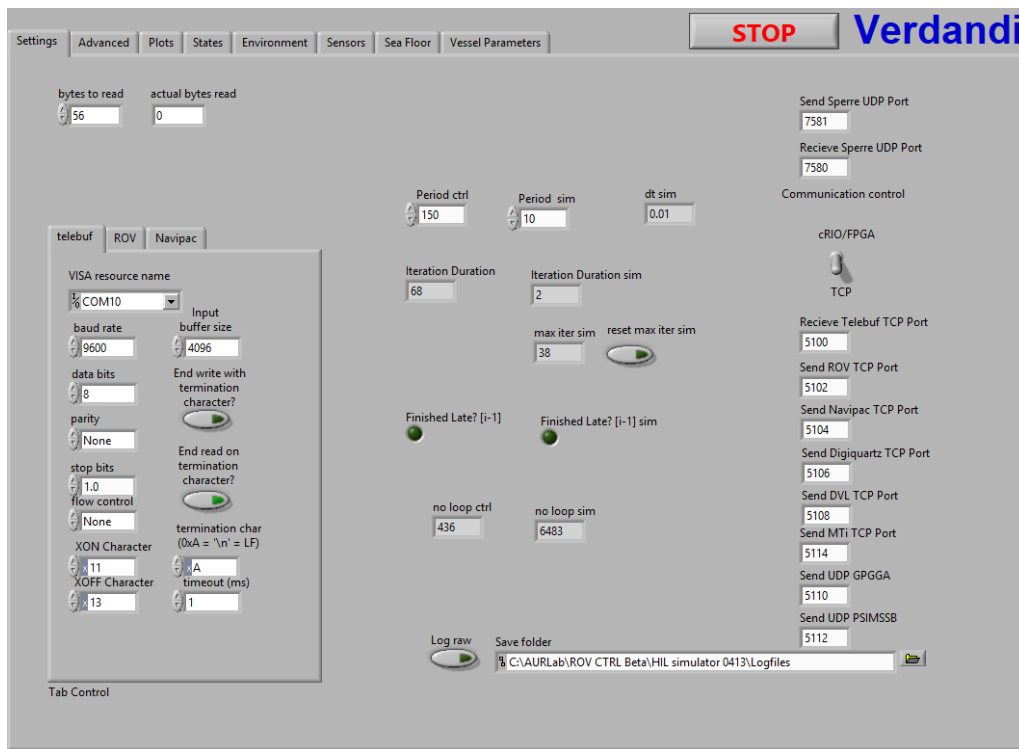


Figure 3.4.4: Front panel of the HIL simulator, "Verdandi".

One new feature of the control system is camera tracking and sonar tracking. This is separate programs that read the sonar data and the camera data, and on the basis of this provide input to the control system. These features are presented in the two theses [9] and [41] respectively. These programs will provide way points to the autonomy program. A test of this was performed by a virtual integration test.

This included as test where a simulation was performed with autonomy program. In the simulation the ROV were to be deployed from a vessel, and move to a site for inspection. The mission was divided into a set of phases, that are presented in table 3.4.1 below.

Table 3.4.1: Phases of the mission simulated in the virtual integration test

Phase	Description
Launch	ROV is launched in the surface, and moves away from the starting position
Descent	The ROV dives to the altitude defined for the mission
Transit	The ROV follows a set of way points towards the target
Sonar tracking	The ROV finds the target on the Sonar data, and approach this target
Camera tracking	The ROV estimate the pose of the ROV relative to the target, and moves into position for inspection
Inspection	The planed inspection is performed.

For this simple test the aim was only to verify that the autonomy program is able to receive waypoint from the camera and sonar tracking programs over UDP link. The autonomy code performed the first three phases in table 3.4.1 autonomously. When the last waypoint in the Transit phase was reached, the state of the system changed to sonar tracking. Here the way points calculated by the sonar tracking code was sent to the control system. When the last waypoint of the sonar tracking was reached, the camera tracking was manually activated. Now the desired state and orientation of the ROV was sent over UDP link to the control system. A further integration of the programs are needed to make the operation completely autonomous, but this is outside of the scope of this thesis. As the test is performed on a simulation, a previously obtained set of sonar data and camera video is used by the camera tracking and sonar tracking. The motion of the ROV in these data set will not mach the motion of the ROV in the simulation. This approach was still used to prove that the programs are able to work together. The reader is refereed to [9] and [41] for a detailed description of how the sonar tracking and camera tracking was developed.

Chapter 4

Result

4.1 Hydrodynamic

4.1.1 Numerical Calculations

The hydrodynamic coefficients were determined using numerical computational tools. In the following sections the resulting added mass and damping will be presented, together with a verification and validation study using similar approaches with the one that was used to calculate the added mass and damping, for a reference object, where the result could be compared with empirical data.

Added mass

The added mass was determined by a hydrodynamic analysis using the computational tool HydroD / Wadam. The resulting added mass matrix is presented in equation 4.1.1. With the calculated added mass matrix \mathbf{M}_A the Coriolis added mass matrix \mathbf{C}_A can be calculated with equation 2.2.19 and 2.2.20 for a given velocity $\boldsymbol{\nu}$.

$$\mathbf{M}_A = \begin{bmatrix} 550.9 & -0.3331 & -69.74 & -1.098 & -29.37 & 0.8607 \\ 0.7009 & 995.3 & 0.14 & -169.3 & 0.07721 & -16.02 \\ -71.01 & 0.6744 & 7311 & 8.562 & 61.56 & 0.3007 \\ -0.2046 & -198.7 & 6.769 & 977.6 & 0.3522 & -41.39 \\ -27.45 & -0.9768 & 148.2 & -1.888 & 2244 & -0.5787 \\ 0.9569 & -19.36 & 0.888 & -41.14 & 0.1511 & 491.9 \end{bmatrix} [kg/kgm] \quad (4.1.1)$$

Damping

The damping matrices \mathbf{D}_L and \mathbf{D}_Q were determined using the approach presented in section 3.1.1. The linear damping matrix was calculated on the basis of CFD simulations. The resulting matrix is presented in equation 4.1.2.

$$\mathbf{D}_L = \begin{bmatrix} -34.5733 & 0 & 0 & 0 & 0 & 0 \\ 0 & -0.3354 & 0 & 0 & 0 & 0 \\ 0 & 0 & 0.0408 & 0 & 0 & 0 \\ 0 & 0 & 0 & -2.7048 & 0 & 0 \\ 0 & 0 & 0 & 0 & -12.314 & 0 \\ 0 & 0 & 0 & 0 & 0 & 0.4557 \end{bmatrix} [kg/kgm] \quad (4.1.2)$$

The quadratic damping matrix \mathbf{D}_Q were determined together with the linear damping matrix, and the calculated quadratic damping matrix is presented in equation 4.1.3.

$$\mathbf{D}_Q = \begin{bmatrix} 625.43 & 0 & 0 & 0 & 0 & 0 \\ 0 & 945.1 & 0 & 0 & 0 & 0 \\ 0 & 0 & 2268.3 & 0 & 0 & 0 \\ 0 & 0 & 0 & 1118.8 & 0 & 0 \\ 0 & 0 & 0 & 0 & 3867.7 & 0 \\ 0 & 0 & 0 & 0 & 0 & 942.1947 \end{bmatrix} [kg/kgm] \quad (4.1.3)$$

The damping coefficients were calculated using a least square regression on a results obtained from the CFD analysis, as presented in section 3.1.1. A total of 8 data points were used for the translational DOF's to create a damping function with velocities ranging from $0.01m/s$ to $1m/s$. For the rotational DOF's six data point is used, with a velocity range from $0.01rad/s$ to $0.2rad/s$. Figure 4.1.1 and 4.1.2 presented the calculated damping function, together with the calculated forces and co responding velocities from the CFD analysis.

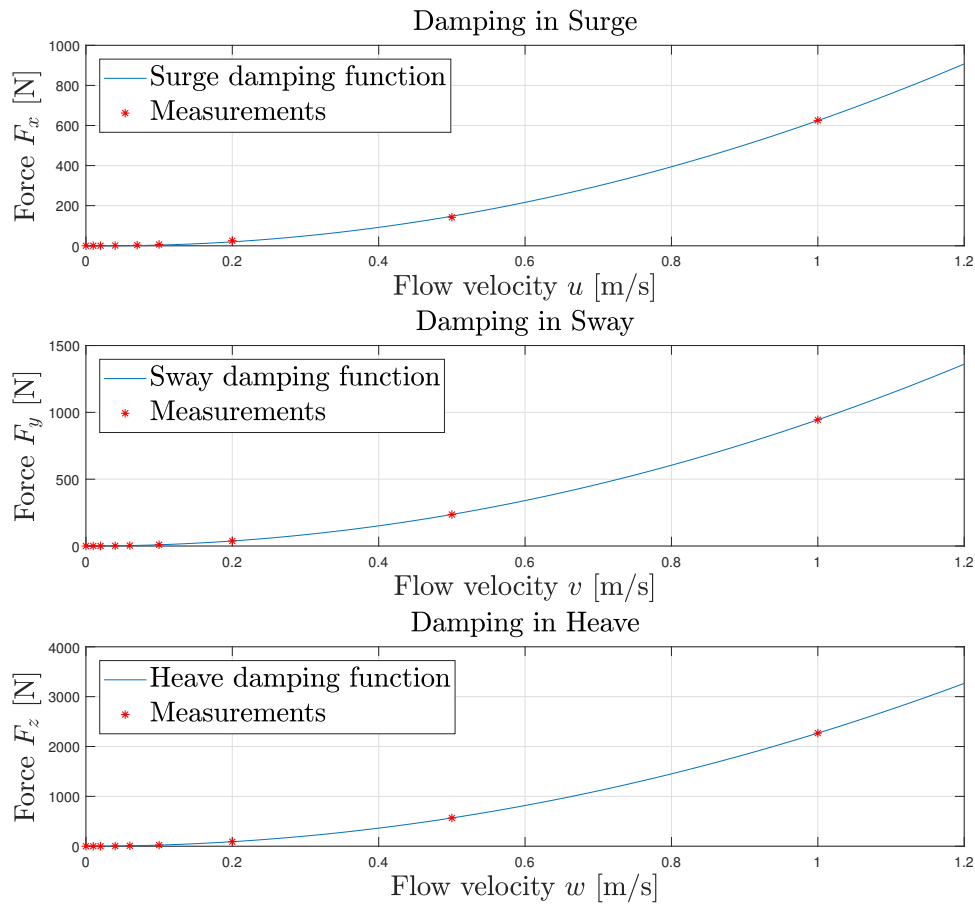


Figure 4.1.1: Plot the damping function for the translational degrees of freedom along with the measurements from the CFD analysis.

The translational damping functions presented in figure 4.1.1 shows that the all data point fall close to the final damping function for all three DOF's. A velocity interval up to $1m/s$ was used as it was necessary to obtain data for an interval where the ROV can be expected to operate. More data point could be used to improve the accuracy of the damping function, but the analysis are time consuming, and the chosen number of data points are believed to be sufficient to calculated a damping function.

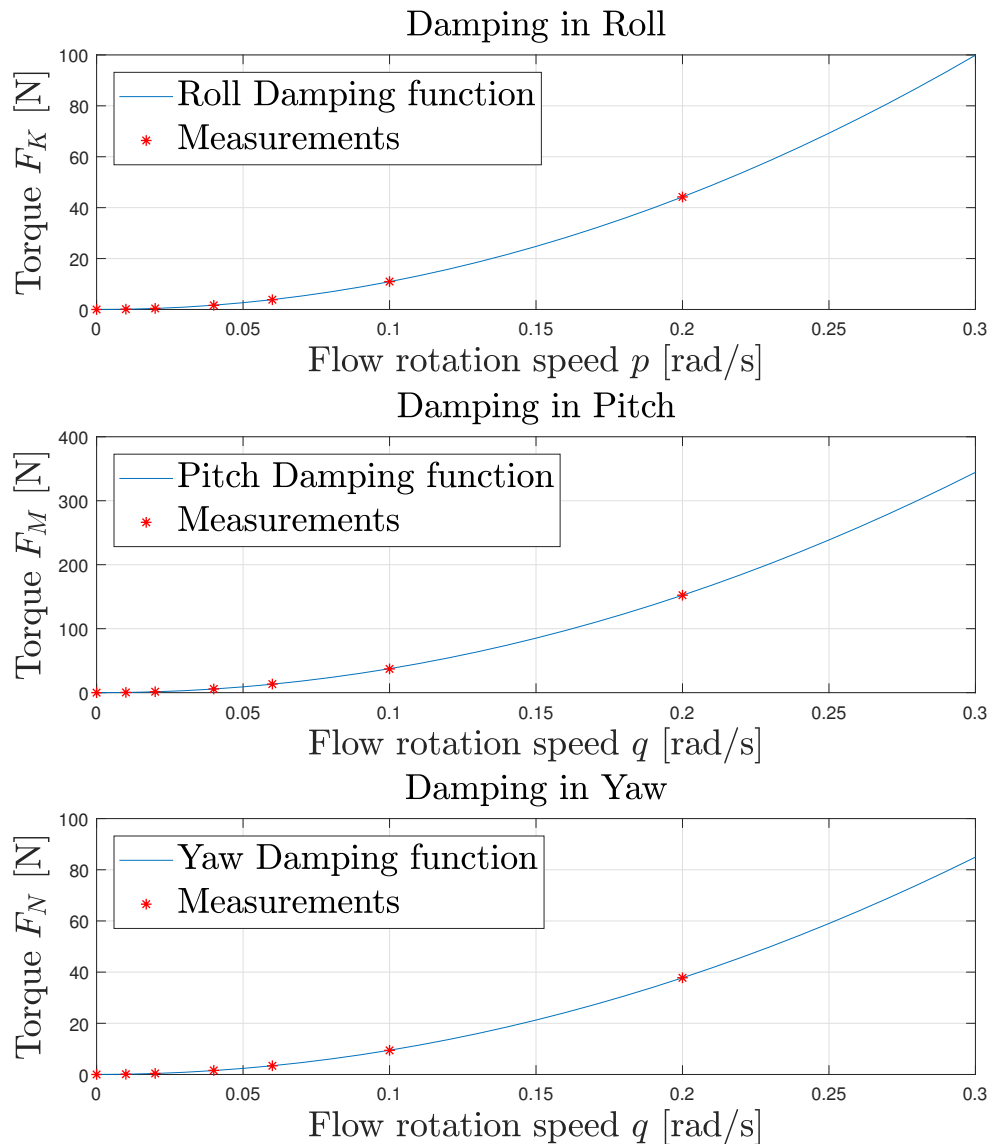


Figure 4.1.2: Plot the damping function for the rotational degrees of freedom along with the measurements from the CFD analysis.

The rotational Damping functions are presented in figure 4.1.2. Again can it be seen that the damping function pass close to all of the data-points. In the linear damping matrices in 4.1.2 some of the elements are seen to be negative. This will cause the damping function to be negative for small values, before the quadratic term start to dominate. This is highlighted in figure 4.1.3. Here the damping function is presented for the DOF's with negative linear damping term, for small velocities. In the large plot the surge velocity can be seen to be negative until a speed of about 0.05m/s is reached. A zoomed in plot above show that the remaining DOF's are negative when the speeds are sufficiently small. It is also observed that the measured data points have a positive value.

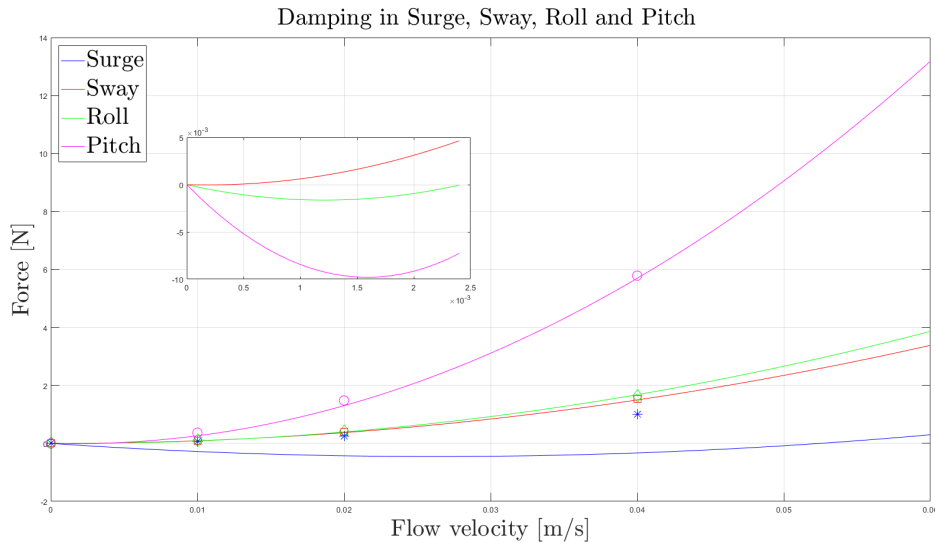


Figure 4.1.3: Plot of the negative par of the damping functions for low velocities, together with the measurements from the CFD analysis.

Verification by empirical calculations

The result from the Hydrodynamic analysis must be verified to ensure that the data is valid. This is done by performing an analysis of of a reference object, using the same procedure as for the ROV, to results obtained with calculations made from empirical data. The result from such an analysis with respect to added mass is presented below. The procedure presented in 3.1.1 was performed for a cube of with dimensions $LxBxH = 2m \times 2m \times 2m$. The added mass obtained from HydroD/Wadam is presented in equation 4.1.4.

$$\mathbf{M}_{A_{verification}} = \begin{bmatrix} 5275.000 & -0.003 & -0.001 & -0.479 & 2.750 & 0.019 \\ -0.001 & 5275.000 & 0.001 & 0.688 & 0.227 & -0.019 \\ 0.000 & 0.003 & 5275.000 & -0.633 & 0.656 & 0.000 \\ -0.012 & 0.563 & 0.004 & 1193.000 & 4.639 & 0.075 \\ 1.312 & 0.012 & 0.000 & -0.174 & 1476.000 & 0.060 \\ 0.027 & -0.030 & 0.000 & -0.141 & 0.122 & 1327.000 \end{bmatrix} \quad [kg/kgm] \quad (4.1.4)$$

By using empirical methods presented in section 3.1.1, the added mass in surge sway and heave is found for a cube with dimensions presented above. This added mass constitute the diagonal terms in the added mass matrix in the top left 3×3 sub matrix. The rotational added mass is determined using equation 2.2.32, and is presented along the diagonal in the rotational part of the added mass matrix in equation 4.1.5.

Table 4.1.1: Comparison of drag coefficient found from empirical analysis and from CFD result

Drag Coefficient	Value
$C_{D,CFD}$	0.849881
$C_{D,empirical}$	0.85

$$M_{A_{empiric}} = \begin{bmatrix} 5576 & - & - & - & - & - \\ - & 5576 & - & - & - & - \\ - & - & 5576 & - & - & - \\ - & - & - & 864.1 & - & - \\ - & - & - & - & 864.1 & - \\ - & - & - & - & - & 864.1 \end{bmatrix} [kg/kgm] \quad (4.1.5)$$

The verification test for the CFD analysis was performed on a cylindrical rod, where the flow was flowing along the length of the rod. The force on the rod was found from the CFD analysis, and as the only contribution to the forces for this simulation is the drag force, the drag coefficient could be directly calculated using equation 2.2.23. The resulting force from the CFD analysis is presented in table 4.1.1 together with the calculated drag coefficient and the empirical CFD coefficient. It can be seen that the two values correspond well with each other.

4.1.2 Experimental Test

The experimental test was performed, but some errors was observed in the experimental data. The setup of the experiment was designed so that one force sensor would record forces in x direction (surge) and one in sway direction. Under the assumption that the motion in surge, sway and yaw are not coupled the sensors should only measure forces in x direction during surge motion. Figure 4.1.4 presents the resulting force measured for a towing of the ROV in surge direction for velocity $0.7[m/s]$, and figure 4.1.5 presents a plot of the velocity of the towing cart during this towing test. In figure 4.1.4 the force measurement is presented. Sensor 1 is oriented in the negative direction y, and sensor 2 is directed in the negative x direction. It is seen that the both of the sensor reach a steady state value, when the correct velocity is obtained. The cyan and green line indicate the average force in the time interval with constant velocity.

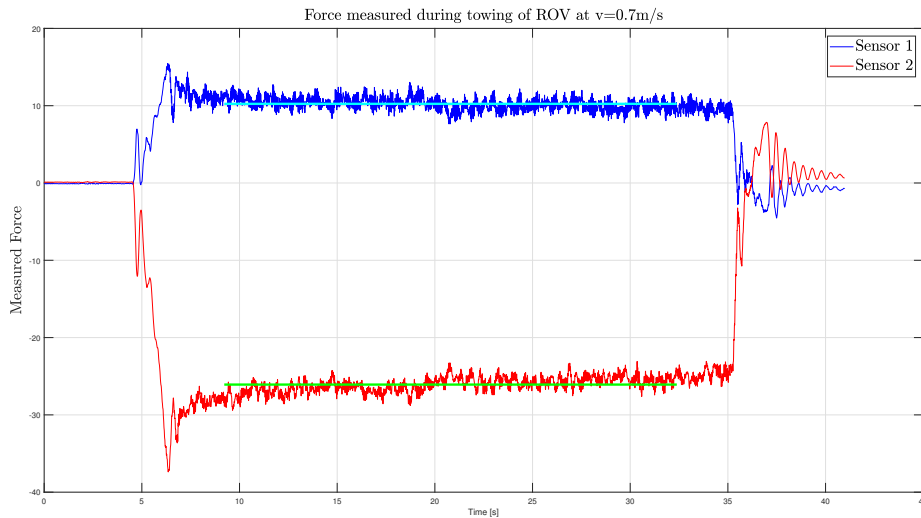


Figure 4.1.4: Plot of the forces measured for sensor 1 and 2, when the model of the ROV was towed in surge direction at a velocity of $0.7[m/s]$

Figure 4.1.5 present the velocity of the towing cart. The orange dots indicate that a constant velocity have been reached. This interval will be used to find the force. Some measurement have been removed from either side of the constant velocity region, to ensure that the most stable region is used.

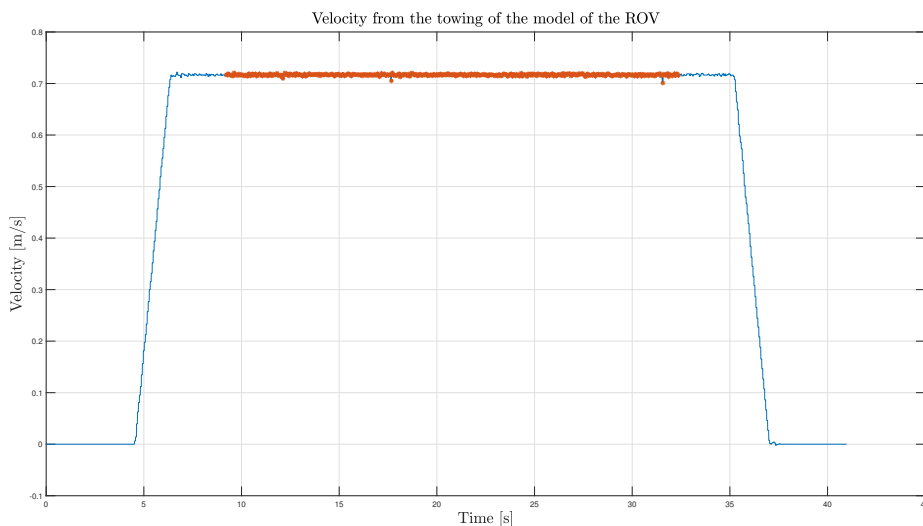


Figure 4.1.5: Plot of the velocity of the towing cart when the model of the ROV is towed at a velocity of $0.7[m/s]$ in surge.

The result from a towing test of the ROV in the y direction is presented in figure 4.1.6 and 4.1.7. It can again be seen that there are both forces in surge and sway direction. In figure 4.1.6, the force on in y direction is smaller than in x direction.

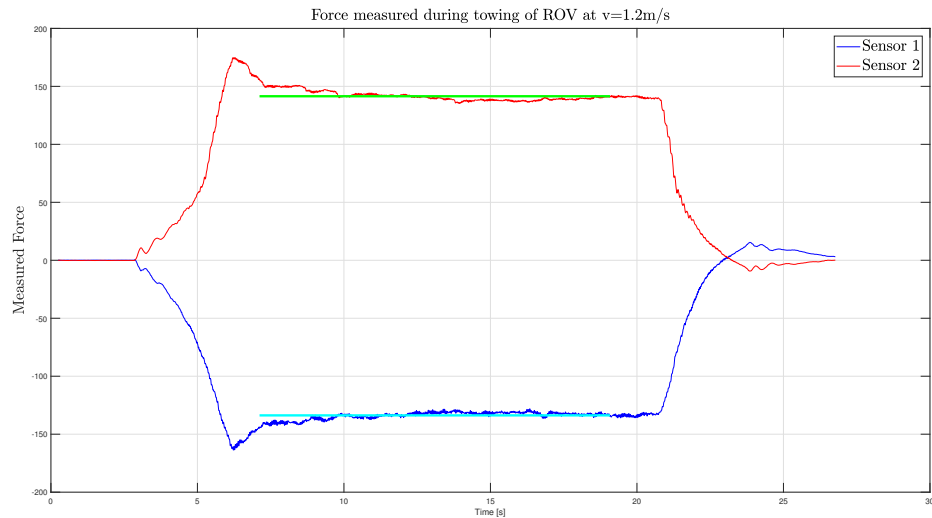


Figure 4.1.6: Plot of the forces measured for sensor 1 and 2, when the model of the ROV was towed in sway direction at a velocity of $1.2[m/s]$

Figure 4.1.7 present the velocity of the towing cart.

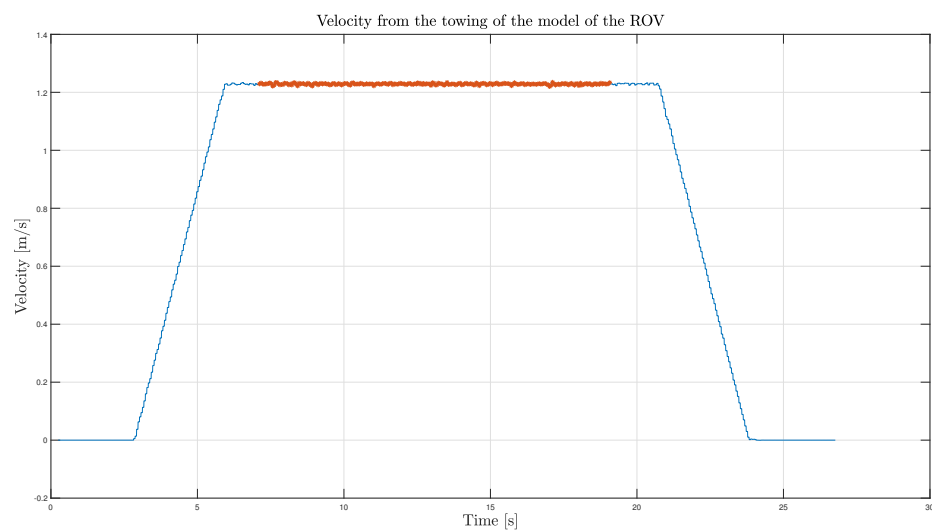


Figure 4.1.7: Plot of the velocity of the towing cart when the model of the ROV is towed at a velocity of $1.2[m/s]$ in sway.

The experiment was performed for velocities from $0.1m/s$ to $1.2m/s$ with a $0.1m/s$ increment. For each velocity the average force is calculated. Only the force from the sensor in surge direction is used to calculate damping and added mass in surge. Figure 4.1.8 presents the force on the ROV in surge direction for constant velocities. Since Coriolis and centripetal forces together with restoring forces, the function presented in figure 4.1.8 become the damping function.

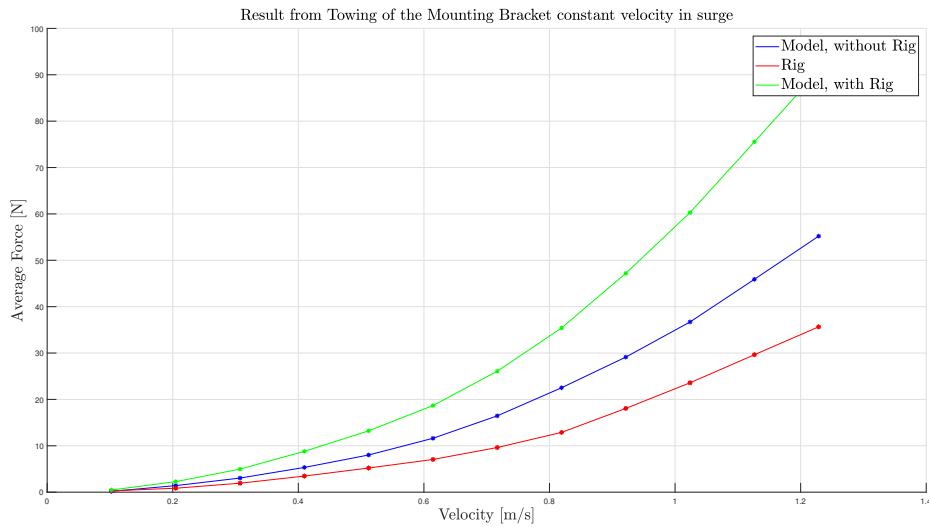


Figure 4.1.8: Plot of the forces when the mounting rig and when the ROV is towed with the mounting rig alone. In addition to this the net force on the model of the ROV is calculated and presented.

The damping function found in figure 4.1.8 above was used to calculate the linear and quadratic damping coefficient for the surge direction. In order to do this, the forces must be scaled. This is done according to table 2.2.1. Both the velocity and the forces are scaled. The linear and quadratic damping is then found by curve fitting the data found. This is presented in table 4.1.2.

Table 4.1.2: Table of the damping coefficient for the surge motion.

Damping element	Value
d_l	-31.237
d_q	1457

The damping coefficients presented in table 4.1.2 have the same order of magnitude as the once calculated with the CFD analysis. This is also observed for the sway and yaw motion. The scaled damping function for sway and yaw is presented in figure 4.1.9 and 4.1.10.

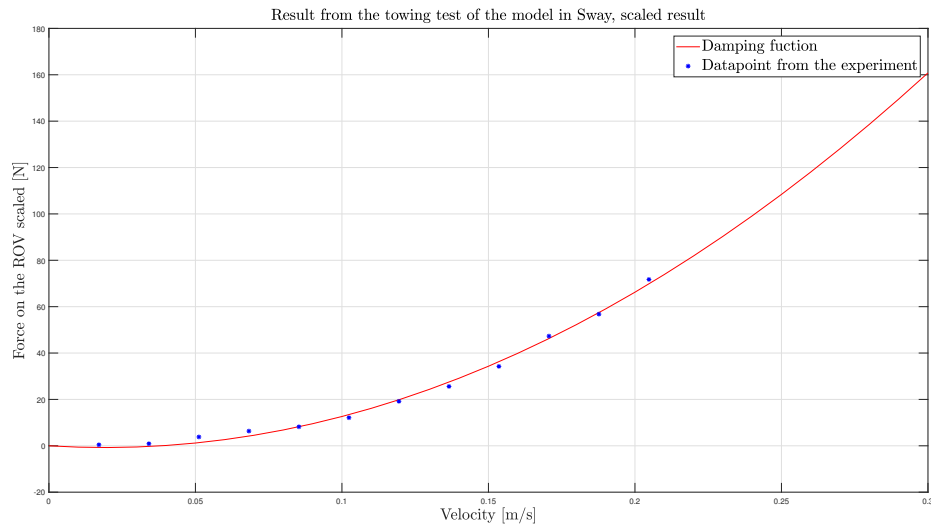


Figure 4.1.9: The figure presents the scaled average sway force and corresponding velocities found from the experimental test, together with the calculated damping function.

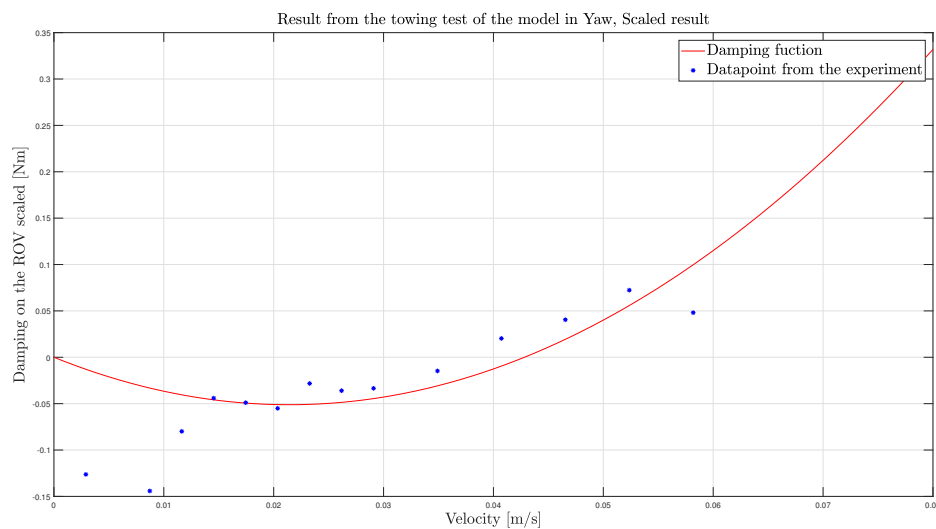


Figure 4.1.10: The figure presents the scaled average yaw moment and corresponding velocities found from the experimental test, together with the calculated damping function.

The resulting damping function for sway, appears to be acceptable, as the damping force is in the same magnitude as the once calculated with the CFD analysis, something that can be seen when figure 4.1.9 to 4.1.1. For the yaw motion the result is seen to be significantly less accurate. The data points does not correspond well with a quadratic function. It is also observed that several of the data points values have negative value. This is caused by a larger measured force during rotation of only the mounting rig, compared to the rotation of the mounting rig and the model. The damping coefficients for both yaw and sway is presented in table 4.1.3. Here the linear damping is again observed to be negative. As the damping must be positive it is clear that either the measurements are incorrect or the hypothesis that the forces from the mounting rig and the model can be linearly superimposed is

invalid. The damping functions for surge and yaw were obtained by only using the sensor measuring the force in the direction of motion, and ignoring the other. It is clear that this will ignore forces with substantial value, something that can be expected to reduce the quality of the damping estimate. Together with the negative linear damping coefficients it was decided that the quality of the data is insufficient for there to be any value in calculating the added mass, as this is dependent on a known damping function, as outlined in section 2.2.4. One additional observation made during the experiment was that some of the measurements were very polluted with noise. One example of this is attached in appendix G, in figure A4.

Table 4.1.3: Table of the damping coefficient for the sway and yaw motion.

Damping element	Value
$D_L Sway$	-78.537
$D_Q Sway$	2048.6
$D_L Yaw$	-4.7780
$D_Q Yaw$	111.5868

4.2 Control System

4.2.1 Thrust Allocation

The thrust allocation developed and presented in section 2.3.6 have been tested with the scenarios presented in section 3.3.1. The test involved simulation tests using the programming tool MATLAB, and tests of the implementation in the ROV control system in LabVIEW. A comparison of the three modes was made in Matlab, while the mode of operation minimizing the energy was implemented in the control system. The input thrust for the Matlab simulation is presented in figure 4.2.1. Here an increasing sway force is given.

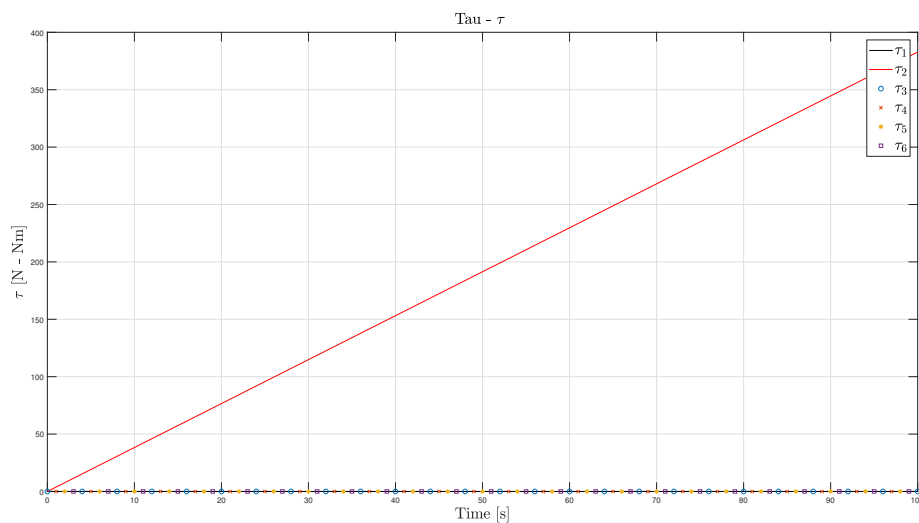


Figure 4.2.1: Desired sway force for the simulation of the thrust allocation.

Figure 4.2.1 show the thrust input to the thrust allocation simulation. In this simulation the desired thrust is increased to above the limits of saturation. This means that that the thrust allocation will not be able to deliver the largest sway force. This is illustrated by figure 4.2.2 which show the error in the resulting thrust corresponding to the thruster speed from the thrust allocation for all five simulations.

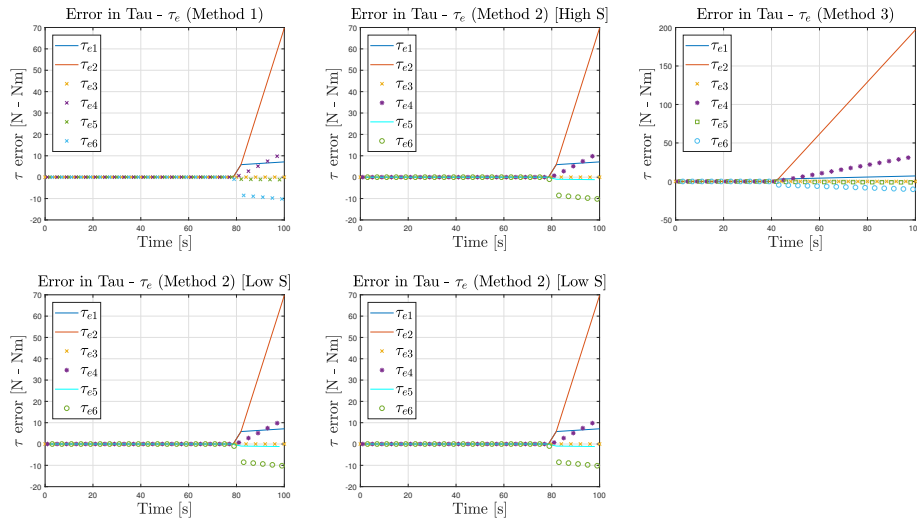


Figure 4.2.2: Error in the calculated thrust for the simulation of the thrust allocation

It can be observed that the error in the resulting thrust is zero for all five simulations until saturation is reached. Saturation is reached for method 3 first, since one thruster is removed. The remaining simulation reach saturation at the same time, which is the when the largest possible sway force is produced. An increase in desired thrust will then only result in a larger error in the thrust as depicted in figure 4.2.2.

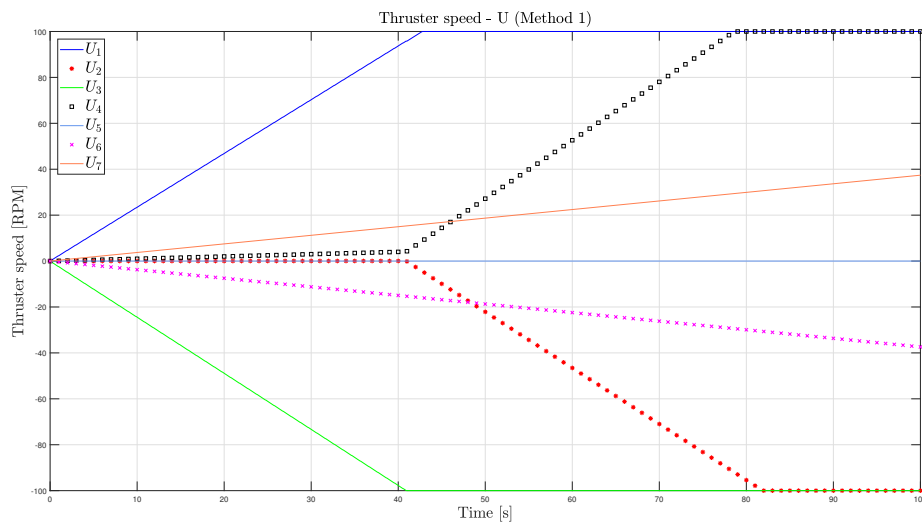


Figure 4.2.3: Thruster speeds for the simulation of the thrust allocation, using method 1

The thruster speeds for the 7 thruster for all of the four simulations is presented in

figure 4.2.3 - 4.2.7. The result from method 1 and method 2 with large S_1 and S_2 can be observed to be very similar. This is reasonable since method 1 will identify the method that minimise the negative thrust for thruster 1 and 2 at among all possible solutions in \mathfrak{N} where method 2 will find the minimal energy solution, but when negative thrust on thruster 1 and 2 is punished so severely that the goal effectively becomes to find any solution where the negative components of 1 and 2 are as small as possible. This is seen in figure 4.2.3 and 4.2.4

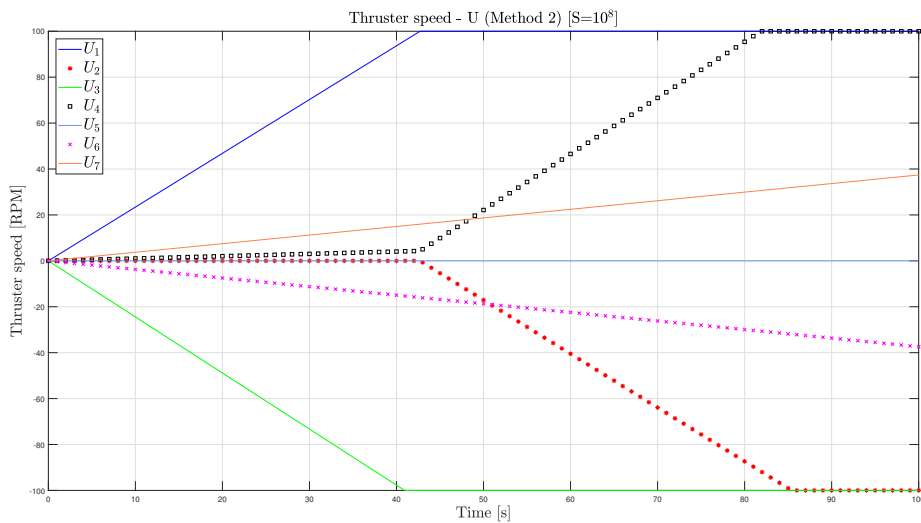


Figure 4.2.4: Thruster speeds for the simulation of the thrust allocation, using method 2 with high values for S

Figure 4.2.5 present the calculated thruster speed using lower weighting values for the energy associated with negative thrust on thruster 1 and 2. The result is that a solution to the thrust allocation problem where a balance is found between limiting the use of thruster 1 and 2 and preventing the remaining thruster from being used too much, to conserve energy. Using thruster 1 and 2 saves energy since it will proportionally reduce the speed on the remaining thruster, but since the energy is proportional to the square of the thruster speed, a more optimal energy performance is obtained. The effect of this will become apparent later. It can also be seen that the first set of thrusters reach saturation at a later point of time compared to the two previous simulations in figure 4.2.3 and 4.2.4. The result in figure 4.2.6 presents the solution with method 2, but when negative thrust on thruster 1. and 2. is not punished. This is equal to a solution that only values reducing propulsion energy

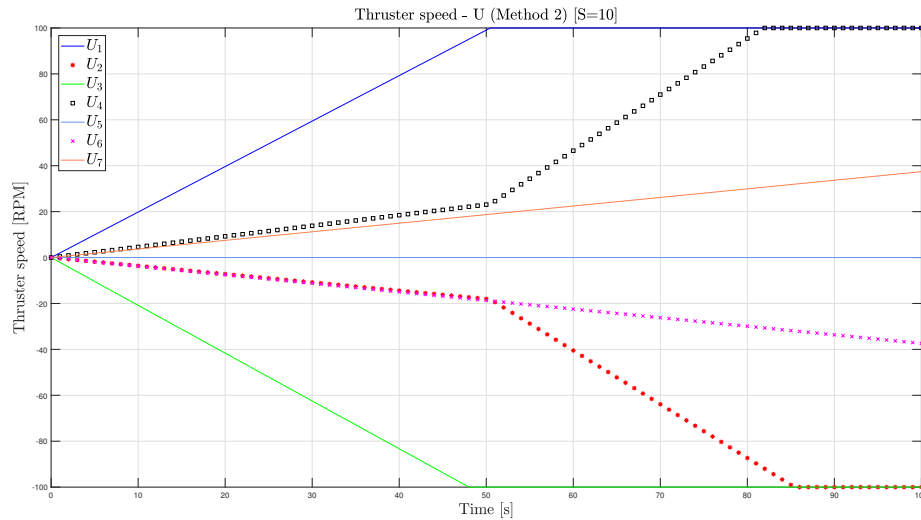


Figure 4.2.5: Thruster speeds for the simulation of the thrust allocation, using method 2 with slightly larger values for S

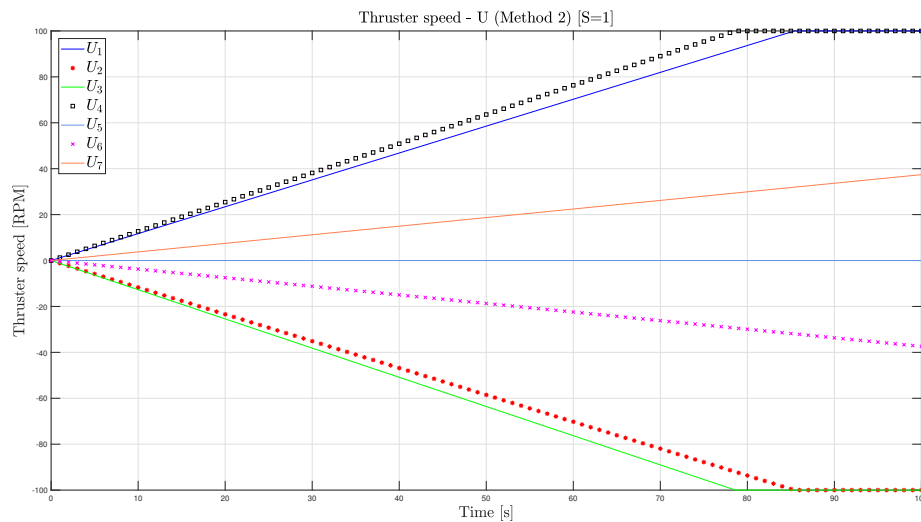


Figure 4.2.6: Thruster speeds for the simulation of the thrust allocation, using method 2 without increasing the values for S

The thruster speed with method 3 described in section 2.3.6 with the input thrust presented in figure 4.2.1 is presented in figure 4.2.7. Since thruster 1 is removed for this method it can be seen that only thruster 2 and 4 can be used, as there is no thruster that can counteract the yaw and surge force from thruster 3 if that is used as well. From symmetry thruster 2 and 4 will cancel each others roll, pitch surge and yaw forces, but retain the sway force. saturation is reached after about 35 seconds. After this more sway force cannot be attained. This correspond to when the error starts to rise in figure 4.2.2 for this method.

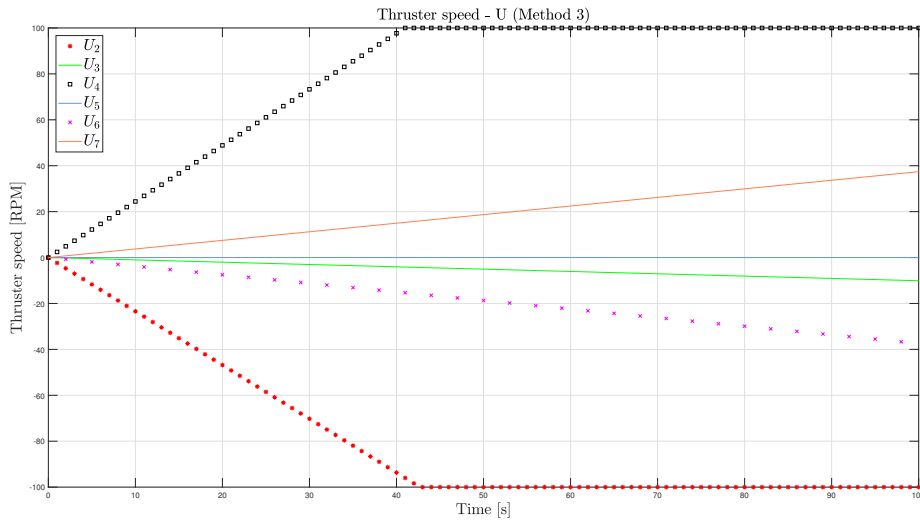


Figure 4.2.7: Thruster speeds for the simulation of the thrust allocation, using method 3

In addition to the thruster speed, a comparison of the energy associated with each method was calculated. The energy is modelled with equation 2.3.28 where the all coefficients S_i were identical and equal to unity. The resulting comparison of the propulsion energy is presented in figure 4.2.8.

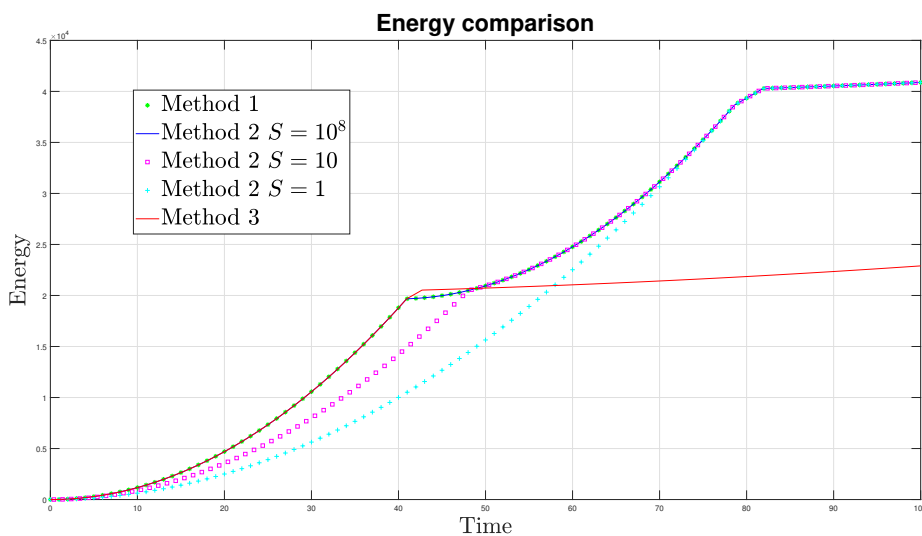


Figure 4.2.8: Comparison of the energy for the simulation of the thrust allocation

The energy comparison show that method 1 and 2 with high S values perform identically. This correspond well with the observations in figure 4.2.3 and 4.2.4. The energy consumption for method 3 is equal to method 1 and 2 with high S until saturation is reached. At this point method 1 and 2 can activate the remaining thruster although this cause water to be flushed in front of the cameras. Method 3 cannot do this, and it reaches maximum energy use. When a low weighing parameter S is used a better energy performance is achieved. It can be seen that the lower the S value, the more energy is conserved. For the case where $S = 10$ the approach will

only have a better energy performance until saturation is reached on the first set of thrusters, where as the case with $S = 1$ will have better performance for the until the last set of thrusters reach saturation, as the thruster reach saturation together. After this the performance is observed to be identical to the other methods aside from method 3.

It is also interesting to see how the different approaches perform with respect to minimizing water from being flushed in front of the ROV. A PI have been established and is defined as the sum of the negative contribution for thruster 1 and 2 according to equation 3.3.1. This is presented in figure 4.2.9. The performance indicator is designed such that a lower value of PI correspond to better performance.

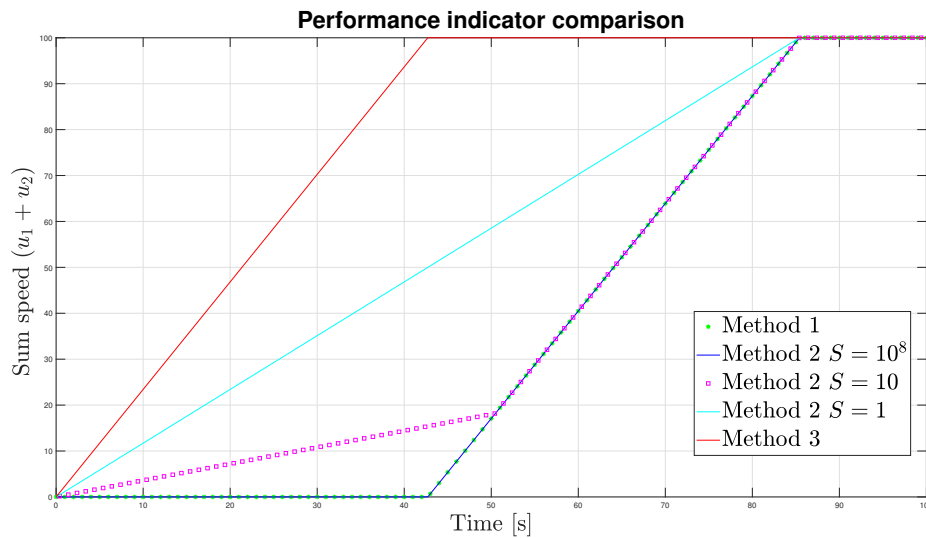


Figure 4.2.9: Comparison of the performance indicator for the simulation of the thrust allocation

In figure 4.2.9 it can be seen that the best performance is obtained when method 1 and 2 with high S is used. The worst performance is obtained with method 3. The with a reduced S values in method 2, reduced performance can be observed. This is a consequence of the system using the thruster 1 and 2 with negative thrust to some extent to reduce energy consumption. On the basis of this is test it is seen that method 1 and 2 preforms equally good when the objective is to prevent water from being flushed in front of the ROV. One significant advantage of method 2 is the flexibility this method can have by tuning the S values, better energy performance can be achieved. The values for S can be determined on the basis of what is the most important goal. This is also a function that can be used as a foundation for a thruster fault accommodation system something that will be discussed later.

4.2.2 HIL Simulation 1

A simulation was performed using the HIL simulator Verdandi. This was a simulation of a tracking mission, where the ROV were to descend to a specified altitude, and start moving along a lawn mover pattern. The ROV were supposed to travel

along six parallel lines, with a spacing between them of $4m$. The lines were to have a angle of 5° relative to the vertical axis. Figure 4.2.10 presents a plot of the motion of the ROV in the North-East plane. The magenta line, and the magenta dots presents the given way points defining the lawnmower pattern. On the basis of this the guidance system will produce a desired state for the ROV. This is presented with the red line in figure 4.2.10. The blue line presents the measurement from the sensors. The observer estimates are presented with the green line in the figure. The ROV can be seen to start with an offset to the first waypoint, in the bottom left corner. The first motion the ROV will make is to move to the first waypoint, and also dive to the desired depth.

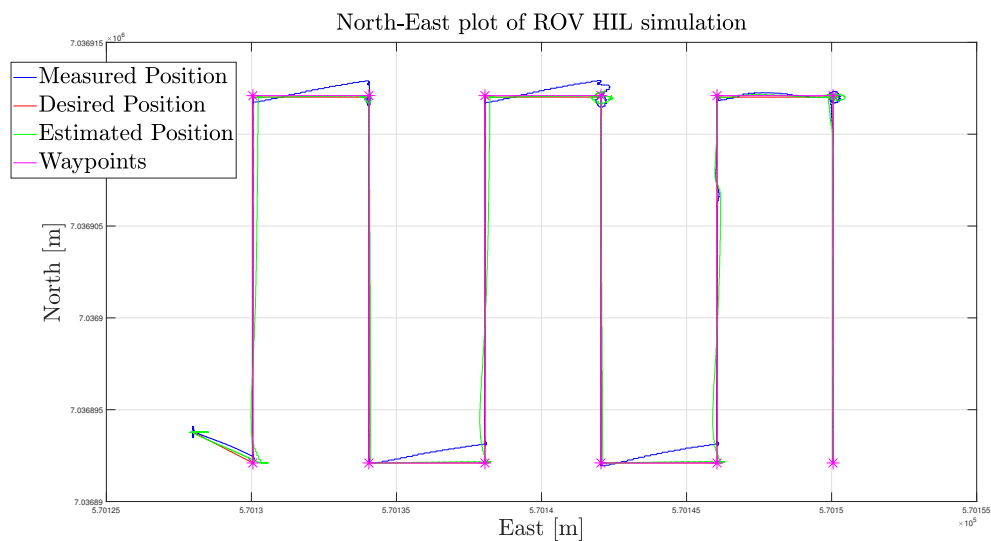


Figure 4.2.10: Development motion of the ROV in North-East plane for the HIL simulation. The estimated states is presented together with the desired states and the measurements. The position in the figure is given in the UTM coordinate system.

In figure 4.2.10 A significant offset between the measured position and the estimated position from the observer can be seen. The observer of the control system is under development, but this is not a part of this thesis, and the inaccuracies in the observer is neither a product nor of consideration in this thesis. The offset between the measured states and the estimate states indicate that the estimate of the estimation is slightly off. The estimation of the position can be seen to be pulled towards the measured value, when a new measurement signal is received. This significantly reduce the performance of the system. Despite this, the ROV control system is able to control the estimated states close to the desired states, and the tracking of the lawnmower pattern can clearly be seen. The main problems with the errors of the observer can be seen when the ROV reach a new waypoint. Especially the motion in east direction causes a large offset between the estimates and the measured position. For the tracking, the green line is relevant, as it is this line the control system "controls". This can be seen to closely track the desired position. The only real problems with the tracking can be seen to be at the corners. Even here the maximum error in the ROV position will only peak at $0.4m$. Figure 4.2.11 presents a figure of the motion in north direction for the ROV over the duration of simulation.

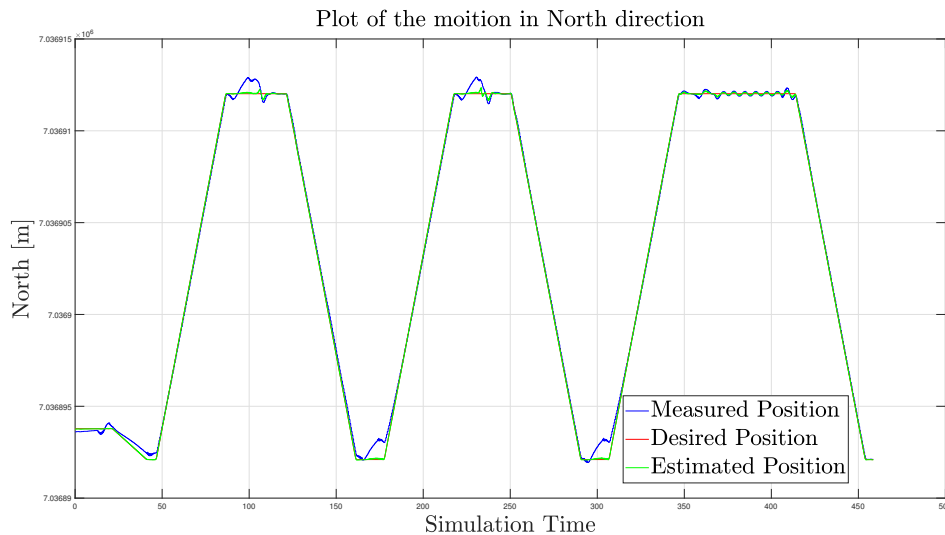


Figure 4.2.11: Development motion of the ROV in North direction for the HIL simulation. The estimated states is presented together with the desired states and the measurements. The position in the figure is given in the UTM coordinate system.

In figure 4.2.11 the problems with lack of correspondence between observer and measurement can be seen when a new way point is reached. However it is also clear that the control system is able to follow the desired position. For the straight parts of the tracking mission, and almost zero offset can be seen between the desired state and the ROV's calculated position. The tracking in east direction is presented in figure 4.2.12. The trend observed in figure 4.2.11 can also be seen in this figure. Offset between the estimated position and the desired position, can be observed after a new waypoint is reached. Aside from this points, the control system is closely able to control the motion of the ROV.

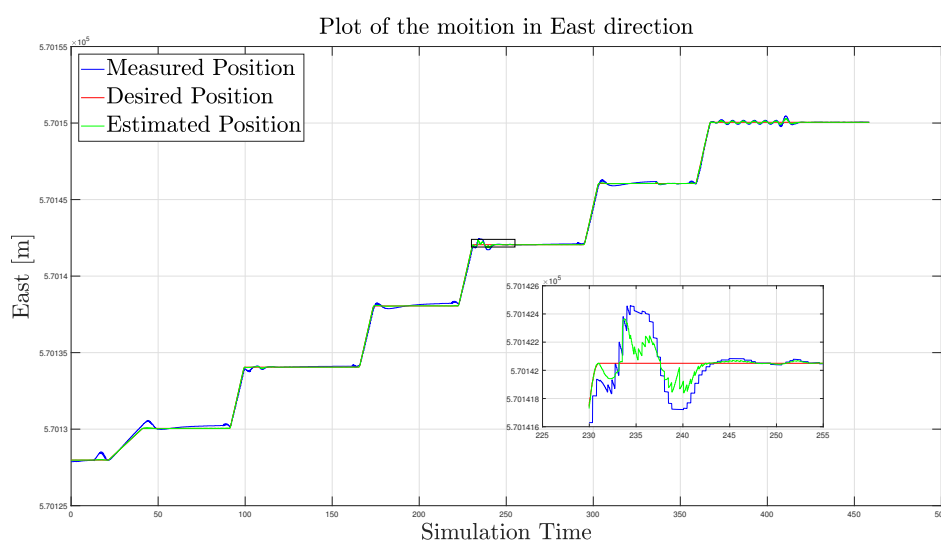


Figure 4.2.12: Development motion of the ROV in East direction for the HIL simulation. The estimated states is presented together with the desired states and the measurements. The position in the figure is given in the UTM coordinate system.

In figure 4.2.12 a zoomed in window is included, where the transient effects that occur after a new way point is reached can more clearly be seen. The magnitude of the offset at the point in time in the zoomed window is approximately $0.3m$, which is relatively low for and ROV at this size. The motion in the vertical direction is presented in figure 4.2.13. The initial dive the ROV makes can clearly be seen here. The offset in this direction is very low, and the tracking is observed to be almost perfect. The zoomed window show the response of the system after the second waypoint is reached. Here the larges of set in the vertical direction between the estimated depth of the vehicle and the desired values is less than $3cm$. For the entire simulation, there is good correspondence between the estimated depth and the measured value.

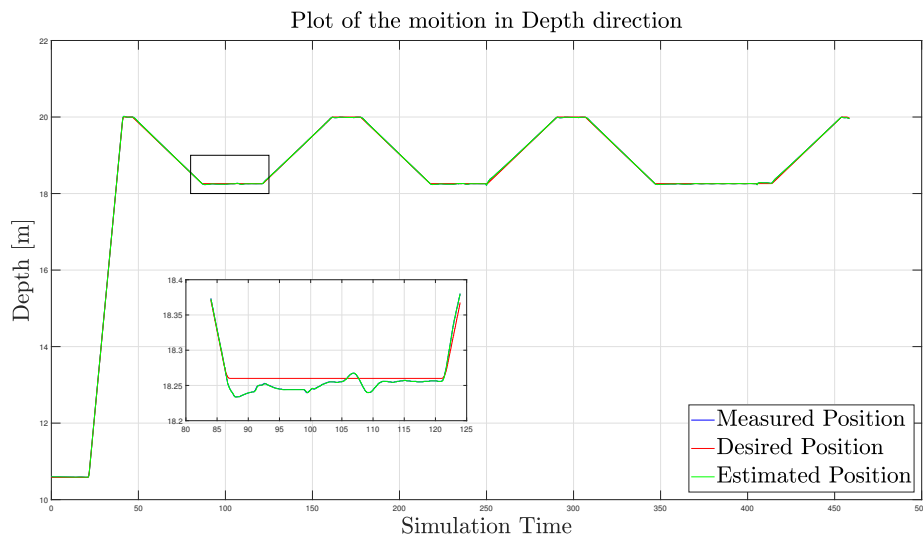


Figure 4.2.13: Development vertical depth motion of the ROV for the HIL simulation. The estimated states is presented together with the desired states and the measurements. The position in the figure is given in the UTM coordinate system.

A three dimensional plot of the motion of the ROV is presented in figure 4.2.14. Here the motion of the ROV is presented in all three spatial dimensions. The offsets in north and east direction can clearly be seen. Similarly it can also be seen that there are small errors in the motion in the vertical direction. The result of the is a mission where the ROV moves in a lawnmower pattern with only small position errors, due to some errors in the observer.

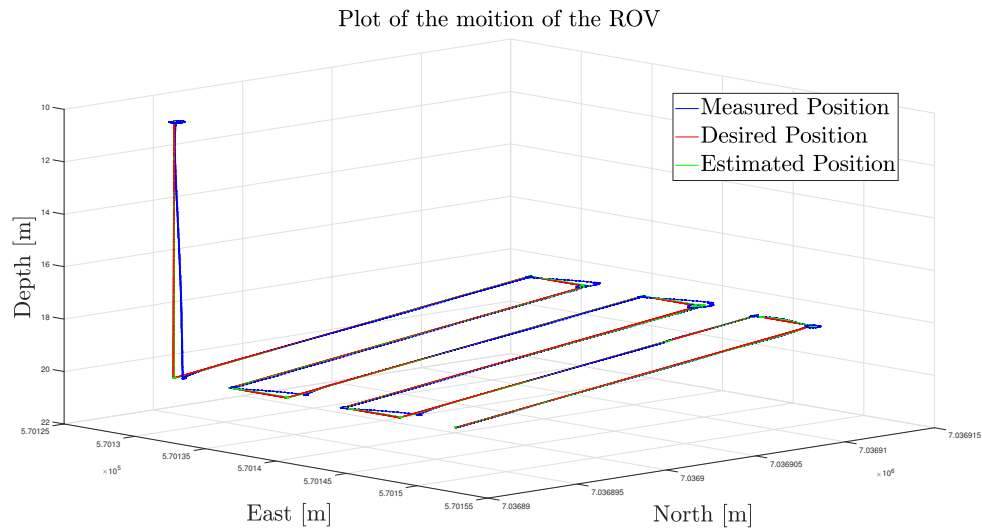


Figure 4.2.14: A 3 dimensional representation of the motion of the ROV during the tracking mission simulated with the HIL simulator. The position in the figure is given in the UTM coordinate system.

The rotational motion is also recorded. For this simulation the goal of the mission was for the ROV was to have as small roll and pitch motion as possible. In such a mission, the observer will operate within the interval in which it is designed. Figure 4.2.15 presents the roll, pitch and yaw motion for the ROV during the HIL simulation. The bottom figure represents the yaw motion. Overall the trend for all three of the plots in figure 4.2.15 are the same. In these DOF's the measurement and the desired values have a good correspondence. The roll and pitch motion is relative small and is limited to a maximum of 2° and 4° respectively. The tracking of the yaw motion can also be seen to be relatively accurate. There are no significant offsets between the desired values and the estimated values. This is partly due to the scale of the plot, and the magnitude of the yaw motion relative to the offsets. By close inspections, some offsets can be seen. The magnitude of these offset will rarely exceed a magnitude of 5°

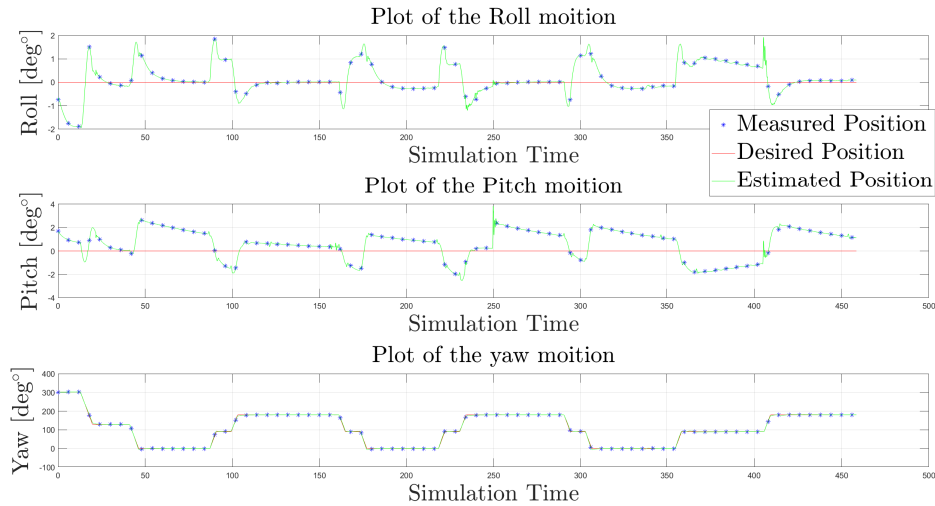


Figure 4.2.15: Development of the Roll, Pitch and yaw motion for the ROV during the HIL simulation. The estimated states is presented together with the desired states and the measurements.

4.2.3 HIL Simulation 2

A second HIL simulation was performed to ensure that the changes and modifications made to the control system GUI and HIL simulator was operating as expected. This simulation consisted of a DP mission, with the aim of simulation a potential real mission for the ROV. Unlike the simulation presented in section 4.2.2, this simulation included environmental disturbances. Waves was included with a period of $T = 5s$ and a wave height of $H_s = 0.5m$. In addition to this a current of $u_c = 0.1 \frac{m}{s}$ in the north direction was included in the simulation. The first step of the mission was to travel to waypoint 1. This included diving to the depth of the first desired DP point. In this phase the wave action on the ROV would be significant. Figure 4.2.16 presents the motion of the vessel in the North-East plane. The ROV starts at the bottom left corner, and moves towards the first DP point. When the first DP point is reached, the ROV will be in DP mode for a period of time, until the next position is given.

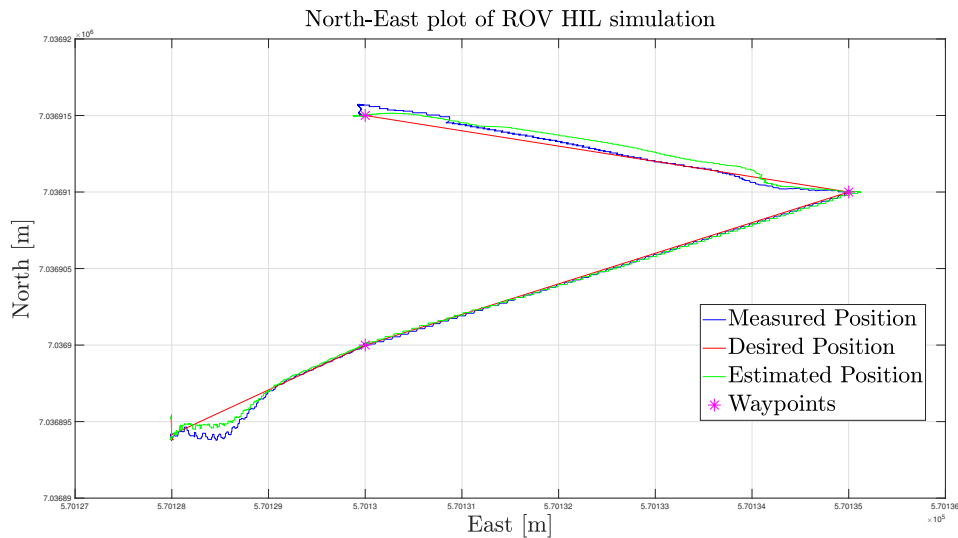


Figure 4.2.16: Development of the motion in the North-East plane for the ROV during the HIL simulation with environmental disturbances. The estimated states is presented together with the desired states and the measurements, and the position is given in the UTM coordinate system.

From figure 4.2.16 Some initial offset between the desired position and the estimated position can be observed. The ROV can be seen to move in a straight line from the first waypoint to the second waypoint, at the right of the figure. At this point the ROV will remain at DP mode for some time, before it is ordered to change heading from 0° , (North) to a heading of 45° . The accuracy of the tracking between the last two waypoints can be seen to be somewhat reduced compared to the accuracy between the first two waypoints. The motion in north direction over time is presented in figure 4.2.17. The measured and estimated position is presented together with the desired position from the guidance system. The purple squares represents the coordinates for the DP point, where the ROV is programmed to hold its position, despite the forces from the waves and current attempting to push the ROV away.

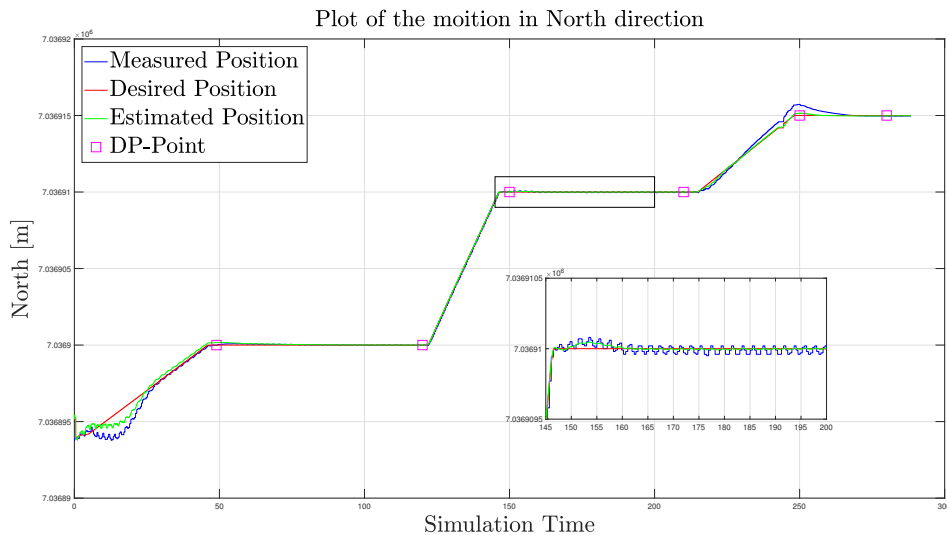


Figure 4.2.17: Development of the motion in the North direction for the ROV during the HIL simulation with environmental disturbances. The estimated states is presented together with the desired states and the measurements, and the position is given in the UTM coordinate system.

The positioning of the ROV in north can be seen in figure 4.2.17 to be relative close to the desired state. An offset can be observed at the beginning of the simulation. At this point the ROV will be at shallow water, and the effect of waves will be more relevant. An aside from this the only point where the positioning of the ROV is less accurate is at the end, after the heading of the ROV have been changed. The reason for this offset can be attributed to an error in the calibration of the magnetometer in the simulation. This will be discussed more and tested later. A similar observation can be seen for the east direction, in figure 4.2.18, as was observed for the north direction above.

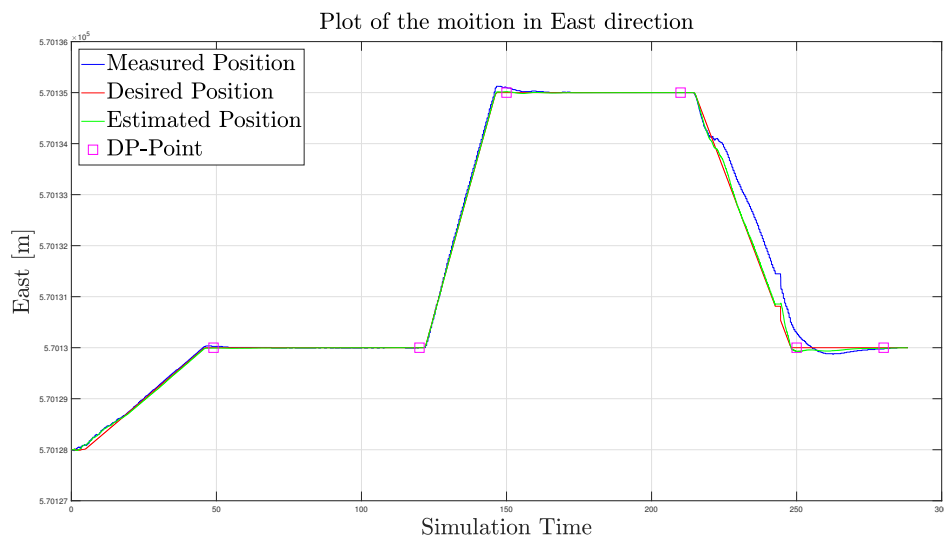


Figure 4.2.18: Development of the motion in the East direction for the ROV during the HIL simulation with environmental disturbances. The estimated states is presented together with the desired states and the measurements, and the position is given in the UTM coordinate system.

In the plot of the motion of the ROV in east direction in figure 4.2.18 for the HIL

simulation with environmental disturbances, the ROV can be observed to be able to retain its position accurately. There are three plateaus in the plot, that correspond to the target positions the ROV was tasked to keep. For the first two positions the error in the positioning is small, and can be seen to be less than m . The last part of the simulation can be seen to have a less accurate positioning. This is due to the change of heading, and the error in the measurement of the magnetometer.

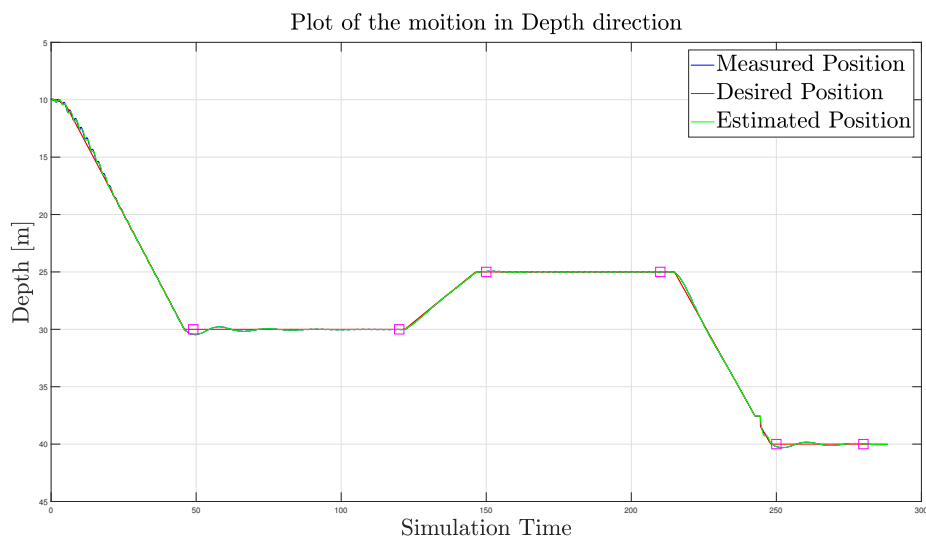


Figure 4.2.19: Development of the motion in the vertical direction for the ROV during the HIL simulation with environmental disturbances. The estimated states is presented together with the desired states and the measurements, and the position is given in the UTM coordinate system.

Figure 4.2.19 present the vertical positioning of the ROV. Some oscillations can be seen at the beginning of the simulation, when the ROV starts of inn the wave zone, and dives down. The difference between the desired depth and the measured and estimated depth can be seen to be relative low. The rotational degrees of freedoms are presented in figure 4.2.20. The desired roll and pitch angles are for the entire simulation defined to be zero. Both roll and pitch motion can be seen to be relatively large at the beginning of the simulation. Especially the pitch motion is seen to be significant, with a magnitude of almost 20° .

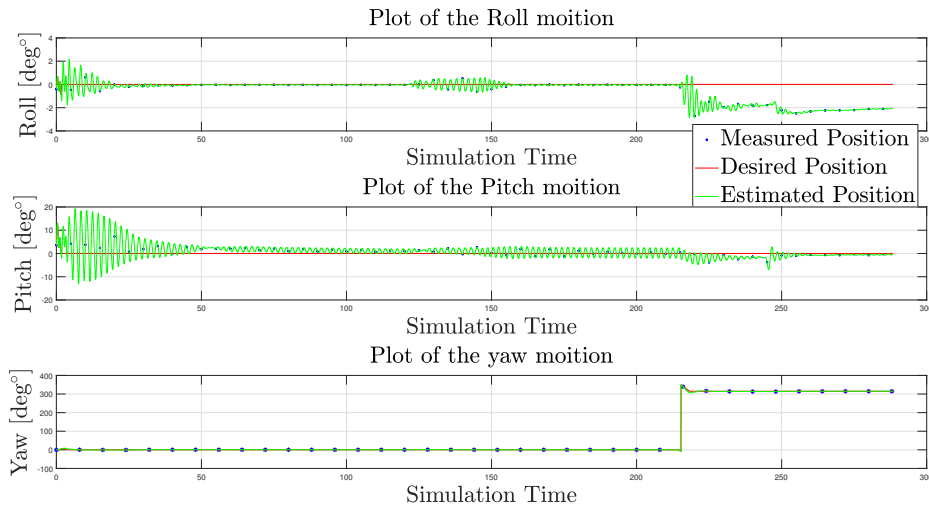


Figure 4.2.20: Development of the Roll, Pitch and yaw motion for the ROV during the HIL simulation with environmental disturbances.

The tracking of the yaw motion is presented in figure 4.2.20. A plot of the motion of the ROV is presented in figure 4.2.21. The ROV starts at the top right corner of the figure. Here an initial offset in the position is observed. This can be attributed to the effect of waves in this region. Aside from this a relatively good tracking of the desired position is observed.

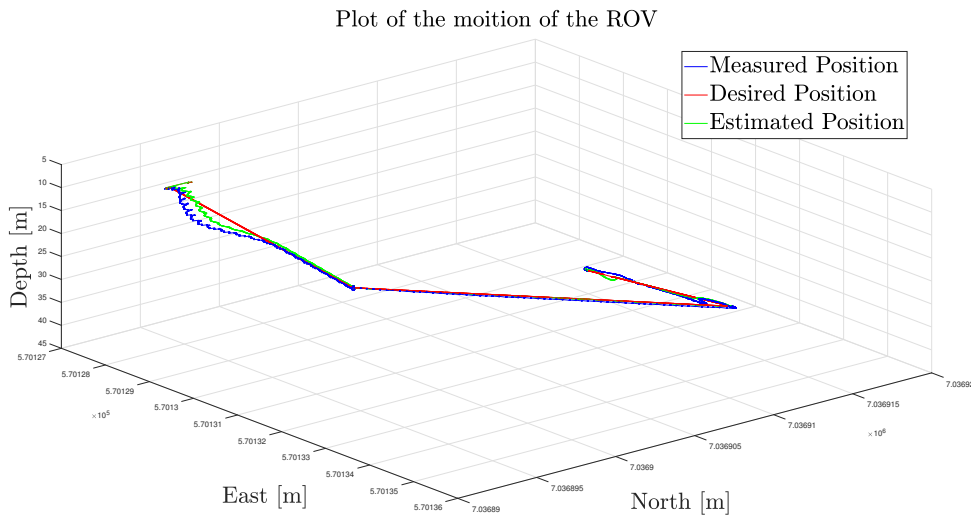


Figure 4.2.21: Plot of the motion of the ROV in a 3D figure for the HIL simulation with environmental disturbances. The estimated states is presented together with the desired states and the measurements, and the position is given in the UTM coordinate system.

4.2.4 HIL Magnetometer Error Test

The HIL simulations are affected by an error in the system. This is an error that takes place in a part of the control system not treated in this thesis. This is related to the calibration of the magnetometer settings. This will result in some reduced

performance for the system. To verify that the cause of the unexpected reduced performance was due to the magnetometer settings a separate test was performed. When the ROV is heading north the error caused by the magnetometer will be minimal. When the heading increases the error will grow to a maximum at heading pure east or west. The observer is designed such that it will give a high weight to the measurement from the magnetometer and the DVL. An error in the magnetometer will give an incorrect heading, and thus also an incorrect position. A test of this was performed by running a short DP mission, with an initial heading north. The ROV was set to move in a straight line due north, and due east. This was done with the ROV heading north. When the final waypoint was reached, the heading was changed to due east, before the controller and observer was reset. The ROV was programmed to drive south and east. The resulting motion of the ROV in the north-east plane from this simulation is presented in figure 4.2.22.

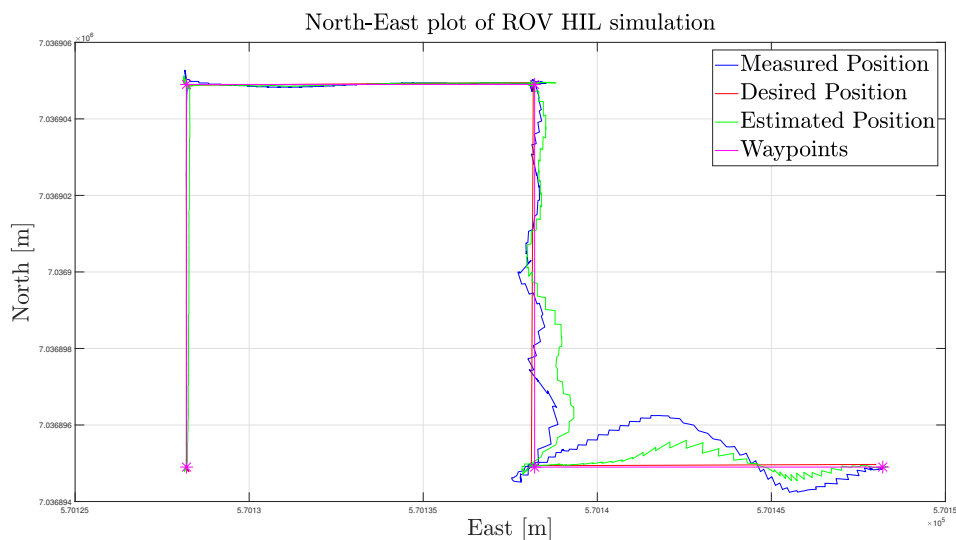


Figure 4.2.22: Motion of the ROV in the North-East plane, for the HIL observer test. The position in the figure is given in the UTM coordinate system.

In the figure of the north-east motion of the ROV in 4.2.22 show that the the ROV are able to track the desired position closely between the first three waypoint, when the ROV was heading north. The ROV had a starting position in the bottom left corner of figure 4.2.22, and from this point started to move north while facing north. The motion of the ROV in the north direction over the duration of the simulation is presented in figure 4.2.23. A significant better tracking can be seen in the first part of the simulation. The vertical line represent the point of time when the heading was changed.

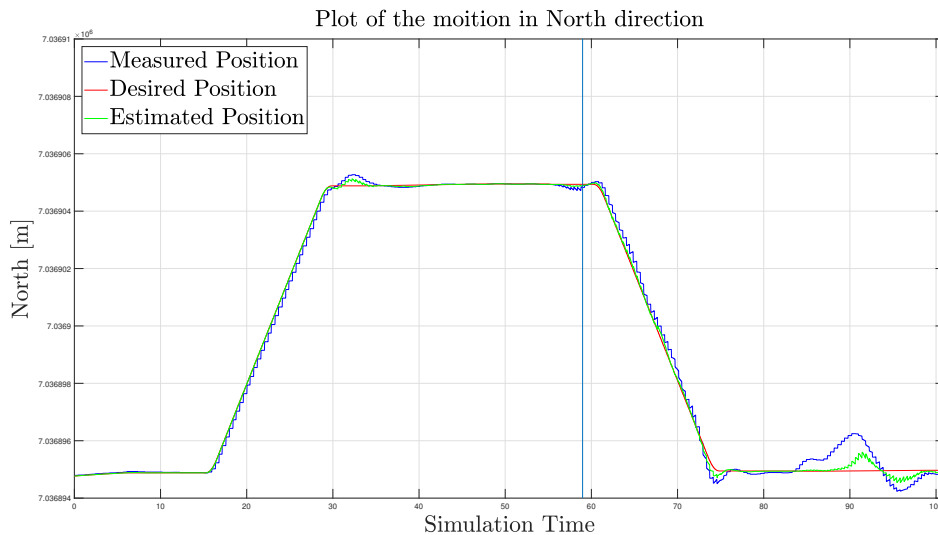


Figure 4.2.23: Development of the motion in North direction, for the HIL observer test. The position in the figure is given in the UTM coordinate system.

Figure 4.2.24 presents the motion of the ROV in the east direction. The trend seen in the previous figures can also be seen here. The performance of the control system deteriorates after the heading is changed.

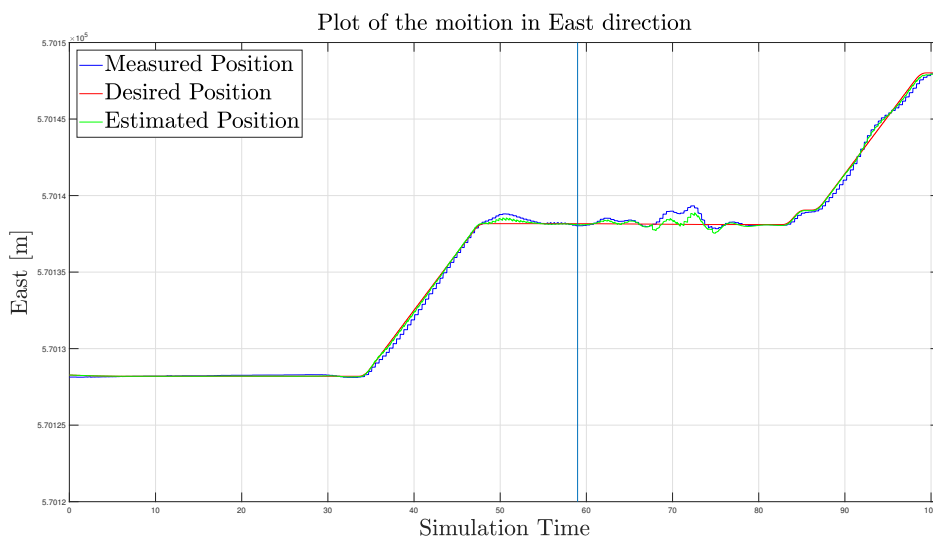


Figure 4.2.24: Development of the motion in East direction, for the HIL observer test. The position in the figure is given in the UTM coordinate system.

The rotational motion is presented in figure 4.2.25. The jump in the desired roll and pitch motion indicate when the control system was activated. Prior to this, no desired roll and pitch motion was defined. The roll and pitch motion is observed to be relatively low for the entire duration of the simulation. The last plot in figure 4.2.25 present the yaw motion. A close correlation can be seen between the measured and desired heading can be seen.

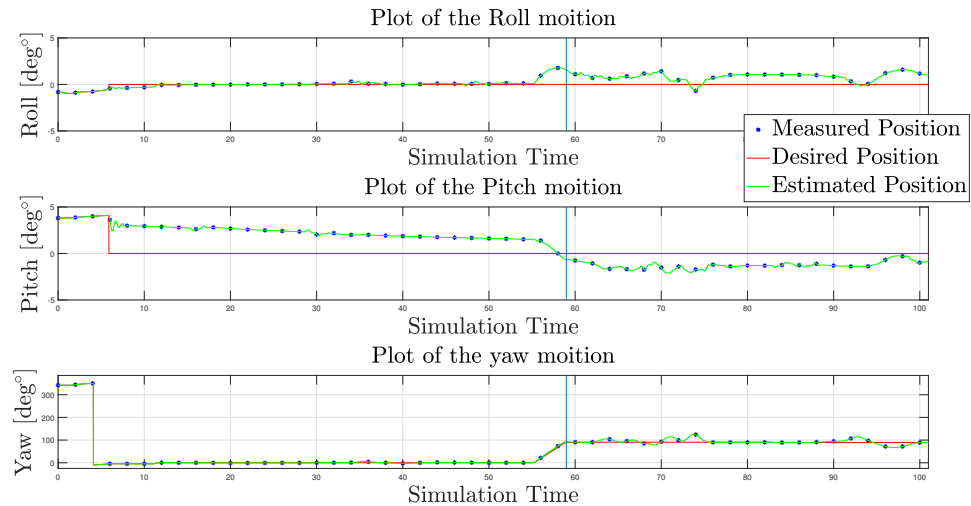


Figure 4.2.25: Development of the rotational DOF's in East direction, for the HIL observer test

4.2.5 Joint Autonomy Simulation / Virtual Integration Test

The joint autonomy simulation, where a virtual integration test of the control system, sonar tracking and camera tracking aimed at testing the sonar and camera tracking algorithms, the control and autonomy system and the communication between the control system and external computers running camera and sonar tracking. As formerly mentioned there HIL simulation is prone to some errors due to the magnetometer calibration. This is especially apparent in this test. Figure 4.2.26 presents the motion of the ROV in the north-east plane. The starting position of the ROV is at the bottom of this figure. The purple stars in the figure represents the given way points in the transit phase, defined in 3.4.1. The cyan circles is the way points obtained from the sonar tacking. The two black crosses lie almost on top of each other, and together with the last cyan circle, and represents the position of the camera tracking waypoint. In this thesis, the result will focus on the performance of the control system and autonomy code in this test.

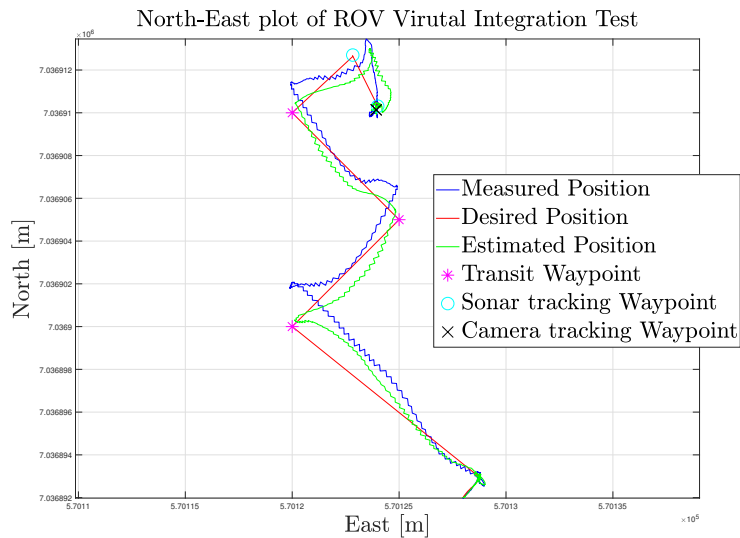


Figure 4.2.26: Motion of the ROV in the North-East plane, for the Virtual integration test. The position in the figure is given in the UTM coordinate system.

The performance of the tracking of the desired state can be seen to be relative poor in this simulation. The ROV have difficulties following a straight line between the way points. The offset between the estimated position and the measured position is significant. However the ROV is by and large able to move towards the waypoint, and the offset is limited to around $1[m]$. From figure 4.2.26 it can be seen that the ROV is able to navigate through all the way points. Figure 4.2.27 present the motion of the ROV in the north direction. In this plot the tracking can be seen.

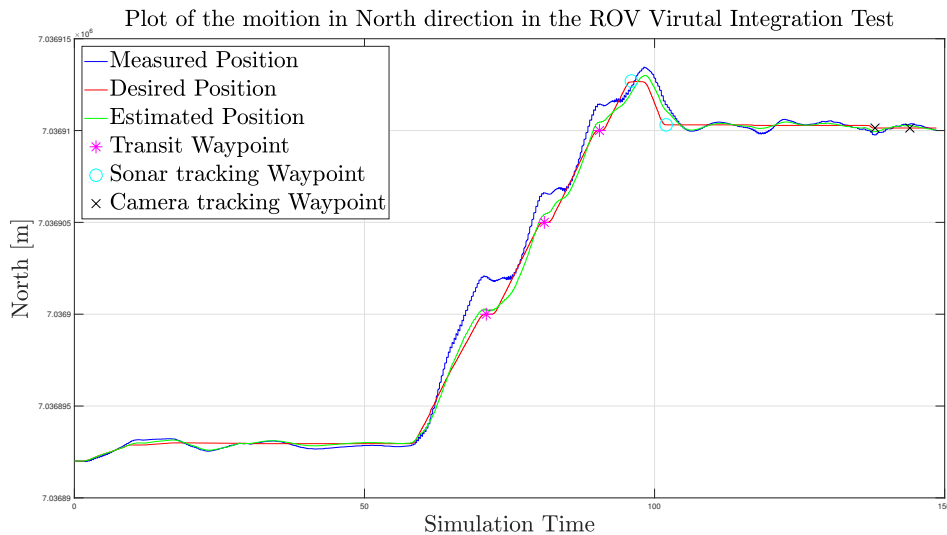


Figure 4.2.27: Development of the motion in the North direction for the Virtual integration test. The estimated states is presented together with the desired states and the measurements. The position in the figure is given in the UTM coordinate system.

The main offsets are between the measured state and the desired state. Figure 4.2.27 show that the error between the estimated state and the desired state is relatively

low. The control system appears to be able to control the ROV to the desired position. Similar observations can be made from figure 4.2.28. Here there are a close tracking between the desired and estimated position. Again there are some offset between the measured state. Between the first and second camera tracking waypoint there is some offset between the estimated and desired position.

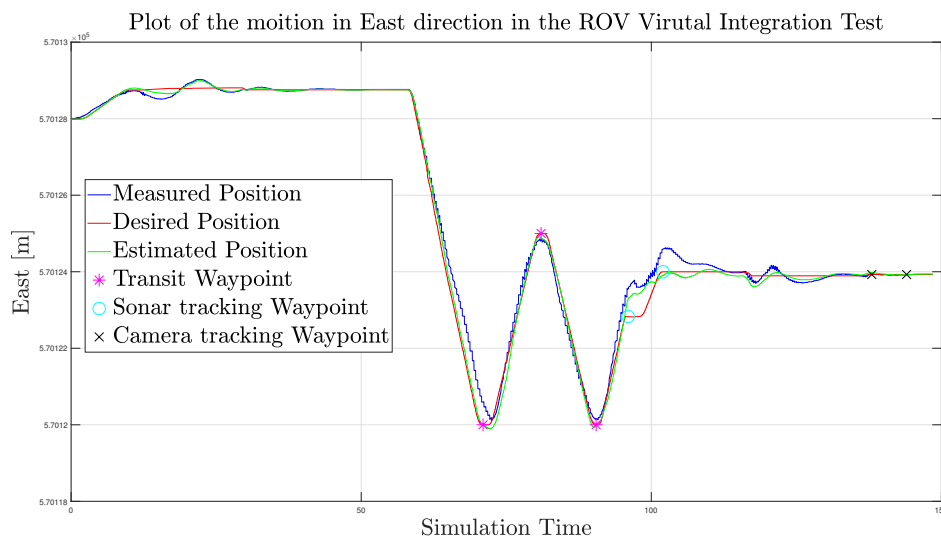


Figure 4.2.28: Development of the motion in the East direction for the Virtual integration test. The estimated states is presented together with the desired states and the measurements. The position in the figure is given in the UTM coordinate system.

The plot of the depth motion of the ROV is presented in figure 4.2.29. The tracking in heave is seen to be significantly better than for the horizontal motions. Towards the end of the simulation the performance is seen to deteriorate. This is a result of an oscillating desired vertical position of the ROV. This oscillations is seen to start after the autonomy system switches to sonar tracking. At this time the autonomy code will calculate a desired depth of the vessel.

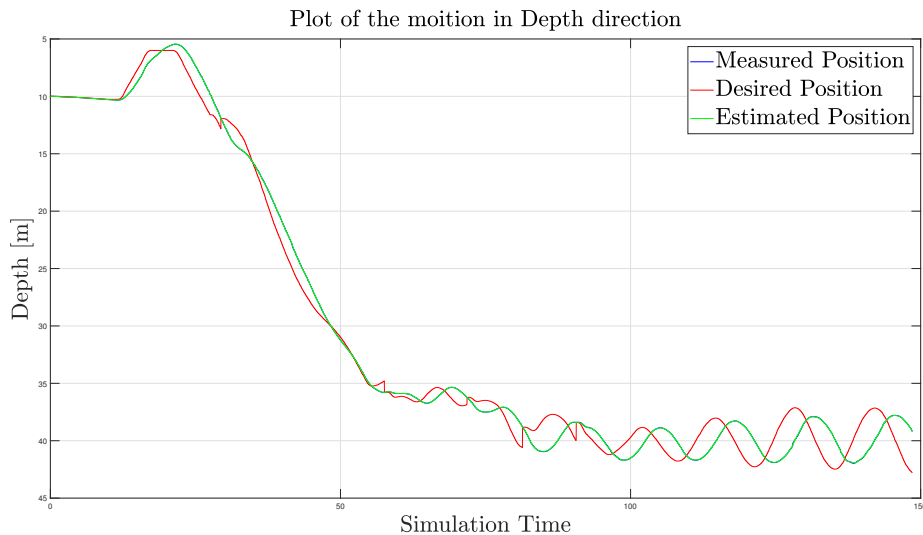


Figure 4.2.29: Development of the motion in the vertical direction for the Virtual integration test. The estimated states is presented together with the desired states and the measurements.

The rotational motion of the ROV is presented in figure 4.2.30. Here the magnitude of the roll and pitch motion can be seen to have a relatively low for the entire simulation. Both are limited to $\pm 5^\circ$, with the exception of one peak of almost 10° in roll. For the yaw motion the tracking of the ROV is seen to be relatively good, with few significant offsets.

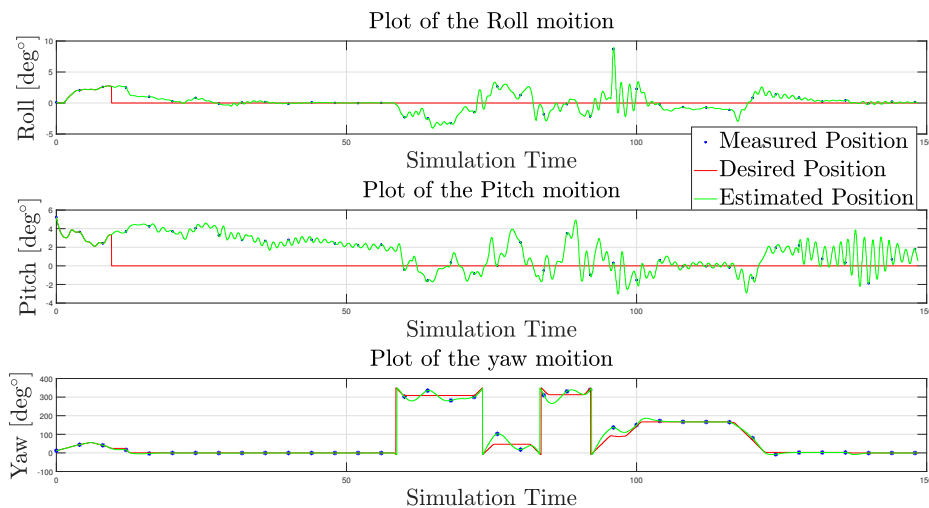


Figure 4.2.30: Development of the Roll, Pitch and yaw motion for the ROV during the Virtual integration test.

In figure 4.2.30 some oscillations can be observed in the yaw motion. This takes place in the transit phase of the simulation. Towards the end of the simulation a new yaw angle is given. This is the result from the pose estimation in the camera tracking, where the pose of the ROV, relative to the target object is calculated, and the necessary orientation to face the object straight on is found. The resulting motion of the ROV is presented in figure 4.2.31 where the ROV's path is plotted

in a three dimensional plot. The initial dive can clearly be seen at the right side of the figure. Here it is also seen that the offset between the estimated and desired position starts to grow as soon as the transit phase begins. This correspond well with the observations made in figure 4.2.27 and 4.2.28 earlier. The figure also show the problems the ROV have with the tracking in the transit phase, but it is clear that the ROV is able to reach the final destination.

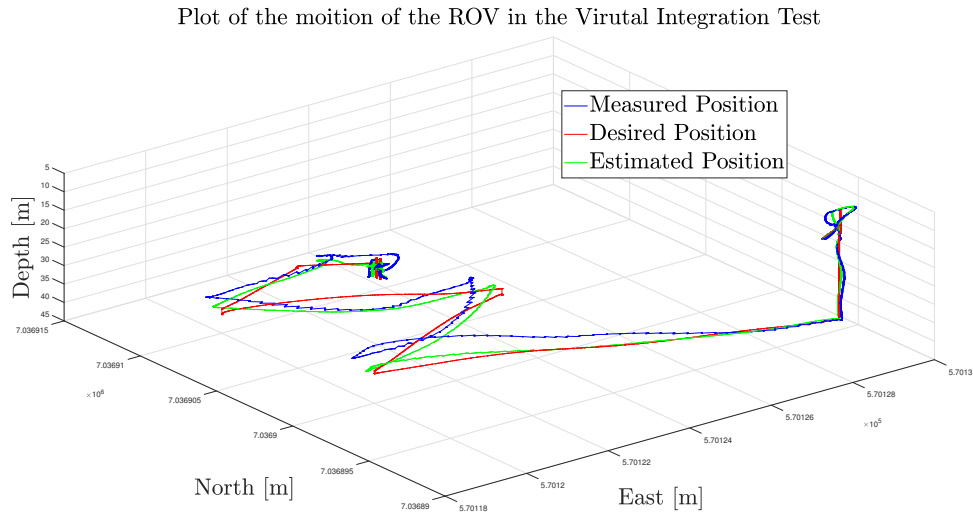


Figure 4.2.31: Plot of the motion of the ROV in a 3D figure for the Virtual integration test. The estimated states is presented together with the desired states and the measurements. The position in the figure is given in the UTM coordinate system.

4.3 System Identification

In the following section the result from the test of applying system identification for the ROV will be presented. As mentioned in section 3.2 three simulations will be performed. The simulation will have a gradually increasing complexity of the model and simulation. As some of the simulations was performed before the damping and added mass was found for the ROV Minerva 2, test values and values from ROV minerva 1 was used.

4.3.1 Simulation A

The result of the simplified model was quite good. The relative difference between the calculated mass matrix $M_{RB} + M_A$ was for almost all DOF very accurate. Matrix 4.3.1 present the mass calculated by the system identification program. For comparison, the mass used for the simulation is presented in equation 4.3.2. The subscript *SysID* indicate that the value is obtained from system identification, as opposed to subscript *Real* which indicate that this is the value used in the

simulation of the system.

$$M_{SysID} = \begin{bmatrix} 3350.9 & 0.00058462 & -69.739 & -0.00020308 & -29.366 & 0 \\ 0 & 3795.3 & 0 & -169.3 & 0.00012261 & -16.02 \\ -71.01 & 0 & 10111 & 0 & 61.56 & 0 \\ 0 & -198.7 & -0.0011583 & 1087.6 & 1.0011 & -171.39 \\ -27.45 & 0.00051884 & 148.2 & 1.0003 & 2434 & 0 \\ 0 & -19.36 & -0.00016774 & -171.14 & 0.00017161 & 691.9 \end{bmatrix} \quad (4.3.1)$$

$$M_{Real} = \begin{bmatrix} 3350.9 & 0 & -69.74 & 0 & -29.37 & 0 \\ 0 & 3795.3 & 0 & -169.3 & 0 & -16.02 \\ -71.01 & 0 & 10111 & 0 & 61.56 & 0 \\ 0 & -198.7 & 0 & 1087.6 & 1 & -171.39 \\ -27.45 & 0 & 148.2 & 1 & 2434 & 0 \\ 0 & -19.36 & 0 & -171.14 & 0 & 691.9 \end{bmatrix} \quad (4.3.2)$$

It can be seen that the result from the system identification is very close to the real values. The reader is made aware that the the elements in 4.3.1 with value 0 in reality represent values smaller than 10^{-5} , but they are rounded of to 0 for the sake of easier presentation. Similar result is observed for the two damping matrices D_L and D_Q . The result for the damping matrices is presented Appendix B in equation A1 to A4. These matrices also show very good result from the system identification analysis. An almost nonexistent error in the calculation can be seen.

4.3.2 Simulation B

Simulation B involved a more complex and complete model of the ROV. This included the nonlinear terms of the Coriolis matrices, as presented in 3.2. When introducing the nonlinear terms in the system identification the performance would be expected to drop. However the system identification is still able to determine many of the elements quite accurately. Especially good results was obtained for the quadratic damping matrix D_Q . The linear damping is also respectively good. Table 4.3.1 summarise the most important parts of these matrices. The matrices themselves are presented in Appendix C in equation A5 to A8. A maximum offset of $1.97[kg/m]$ in a matrix where the diagonal term reach values as large as 386, is a relatively good result.

Table 4.3.1: Performance of the system identification for the damping matrices in simulation B

Matrix	Error	Unit
D_Q larges error	1.9665	$[kg/s / kgm/s]$
D_Q smallest error	0.0013486	$[kg/s / kgm/s]$
D_L larges error	0.063622	$[kg/s / kgm/s]$
D_L smallest error	7.1277e-05	$[kg/s / kgm/s]$

The difference between the calculated mass matrix $M + M_A$ and the real values are presented in equation 4.3.3. Here the values in the matrix represent the error between the real and calculated values relative to the real values. The real mass matrix of the system and the calculated matrix is presented in appendix C in equation

A10 and A9.

$$\mathbf{M}_{difference} = \begin{bmatrix} 1.2865 & -9.5983 & -0.57797 & 1.6161 & 0.32463 & -0.23593 \\ 10.131 & -1.3277 & 14.944 & 4.0181 & -7.2984 & -0.67296 \\ 10.621 & -9.6142 & 15.036 & 2.5499 & 5.4015 & -0.435 \\ -31.044 & -4.3571 & -51.351 & 0.1289 & 12.327 & 0.0021177 \\ -22.243 & 2.5612 & -36.327 & 2.5186 & 3.3786 & -0.44325 \\ -25.298 & -2.7291 & -42.812 & 0.63451 & -0.70015 & -0.12423 \end{bmatrix} \quad (4.3.3)$$

From the matrix above in 4.3.3 it can be seen that there are some errors in the calculations of the mass relative to the real values, but the magnitude is relatively low. The largest offset here is at 51.351[kgm].

4.3.3 Simulation C (HIL)

The result from the system identification performed on the HIL simulation, showed relative high level of accuracy. A comparison between the calculated mass of the system and the mass of the system in the simulation is presented in equation 4.3.4, and calculated as $\mathbf{M}_{difference} = \mathbf{M}_{SysID} - (\mathbf{M}_{RB} + \mathbf{M}_A)$. The mass matrix and the calculated mass is attached in Appendix D, in equation A11 and A12 respectively.

$$\mathbf{M}_{difference} = \begin{bmatrix} 0.1315 & -0.2230 & 2.7704 & -0.7749 & 0.1849 & -0.1699 \\ -0.0070 & 0.0101 & 0.0029 & 0.0004 & -0.0014 & 5.9930 \\ -0.0070 & -0.0150 & -0.0183 & 0.0090 & -0.0053 & 0.0012 \\ -0.1552 & -0.1919 & 1.1971 & -0.2186 & -0.0166 & -0.0631 \\ -0.0162 & 0.0364 & 0.0427 & 0.0020 & -0.0202 & 0.0022 \\ -0.1045 & 5.9785 & 0.4761 & -0.3593 & -0.0216 & 0.0310 \end{bmatrix} \quad (4.3.4)$$

In the comparison matrix in 4.3.4 it can be seen that the result for the mass matrix is relatively good. The largest error is observed for some off-diagonal term at almost 6kg. For a simulation of an ROV with a mass (incl. added mass) of about 760kg, this is a relative offset of less than 1%. The two damping matrices is attached in appendix D, together with the mass matrix. For the linear damping the maximum error between the calculated values are found to be around 15kg. The result are observed to be somewhat less accurate for the quadratic damping. Here all elements in the quadratic damping matrix have an error less than 50kgs, with the exception of two. These two have a magnitude of -315.59 & -507.38. Both of these elements are off-diagonal terms in column 3, corresponding to the forces calculated due to heave motion. The error in the diagonal terms of the quadratic damping matrix is presented in table 4.3.2. The largest percentage offset for the diagonal terms is seen to be 6.62%.

Table 4.3.2: Relative error in the diagonal terms in the quadratic damping D_Q

Dof nr.	Error [%]
1	6.62
2	4.9781
3	-0.18382
4	-2.7104
5	-0.038244
6	-0.3564

Chapter 5

Discussion

5.1 Hydrodynamic

5.1.1 Added Mass

The result of added mass analysis with the computational tool is presented in equation 4.1.1. In the calculated added mass matrix it can be seen that the diagonal terms are substantially larger than the off diagonal term. For the pure translational degrees of freedom presented as the top left 3×3 elements in the matrix. Here it can be seen that the heave motion have the largest added mass of more than $7000[kg]$, compared to the surge and sway added mass where the added mass for both is less than $1000[kg]$. This is a reasonable result since the added mass originate from the force required to move the surrounding fluid. Since the ROV seen from the front or the side is hollow, water is allowed to move through the ROV when moving in surge or sway. However in heave this is not the case, and more water must be moved to move the ROV in heave.

The Added mass matrix also illustrate that there is little coupling between the surge and the sway motion. This is evident with the relative low and negligible values at the elements at row 1 and column 2 and row 2 and column 1. The most important off diagonal terms and therefore also coupling between the degrees of freedom can be seen for roll and pitch motion, that is along row and column 4 and 5. This is a result of the vessel geometry and given the shape of the ROV it is a reasonable result. A motion in pitch will due to lack of fore-aft symmetry result in forces in surge and in heave direction. Similar observation is made for the roll motion. The added mass matrix is also observed to not be symmetrical. For a real system this is necessary. However, the calculated added mass matrix show that the added mass matrix is very close to being symmetrical. The relative difference between symmetrical elements are seen in equation 4.1.1 to be very low.

Any result from computational tools should be quality controlled. This is good habit, and is important to ensure that errors in the program or in the use of the program have affected the results. To do this the result from an analysis with HydroD / Wadam can be checked against empirical or experimental results. For a body with a complex geometry such as the ROV Minerva 2, it is for practical purposes not possible to perform an accurate analysis of the added mass by employing empirical

methods. Instead a simple geometry was used to compare the result for the HydroD / Wadam with empirical results. A cube with dimension $2m$ was used, as presented in figure 3.1.6. The added mass found with numerical tools is presented in equation 4.1.4. For a deeply submerged cube where there exist symmetry around all axis, one would expect the different degrees of freedom to be uncoupled. This is because symmetry would mean that forces cancels. For example any positive heave force on the front of the vessel due to pitch motion be cancelled by an equally large negative heave force at the aft. This is also evident in the resulting added mass matrix from Wadam, presented in equation 4.1.4. Here the off-diagonal terms can be seen to be near zero. The off-diagonal terms are nonzero, but all have a magnitude smaller than $5[kg/kgm]$. These small off-diagonal terms are due to small computational errors in the computer. One method to limit this can be to reduce the mesh size in the model. The magnitude of the off-diagonal terms is seen to be sufficiently small relative to the diagonal terms to be considered as accurate enough. However this inaccuracies should noted, and the implications of this is that some small errors should be expected for the added mass of the ROV presented in equation 4.1.1.

The empirical added mass for the cube is presented in equation 4.1.5. Only the diagonal terms are presented, as they are the once that are relevant as previously discussed. The translational added mass was determined directly using the three dimensional added mass. The result can be compared to the translational added mass for the cube with the Wadam calculations. The translational added mass is seen to be similar for both calculations. The computational calculation resulted in an translational added mass of $5275[kg]$ where the empirical data suggested that the added mass would be $5576[kg]$. This is a relative difference of only 5.4%. This indicate that the result from the computational tool closely represent the real added mass. This gives reason to assume that the calculated added mass for the ROV will be reasonable close to the real value for the added mass.

For the rotational degree of freedom the empirical method provide some lower estimated added mass compared to the result from HydroD/Wadam. One weakness of the rotational added mass from empirical estimation is that the added mass is not directly found, but the two dimensional added mass coefficient found from table A1 and A2,[39]. The rotational added mass was then found by strip theory. Strip theory is, as presented in section 2.2.2, based on the assumption that the flow changes slowly along the length of the body. This is good approximation for a long and slender body, but for a body such as a cube this approximation will not be true, and some inaccuracies can be introduced. This can explain difference between the empirical estimates and the numerical calculation. Although the difference is relatively large, the values is both around $1000[kgm]$, and the results from HydroD/Wadam can be considered as sufficiently accurate for the purposes of an ROV control system.

The calculated added mass for the ROV presented in equation 4.1.1 is developed for a deeply submerged vessel without any waves. At these conditions the added mass will be constant. If the ROV would only be operating under this condition, the calculated added mass would accurately represent the vehicle. However the ROV will be launched from a ship, and have to descent to the operating depth, and return to the ship after the mission is complete. These two phases will be relevant

for all ROV, given they don't operate from some form of submerged docking station. Under these two phases the assumptions the added mass is calculated under is invalid. This becomes more relevant if there are waves present. Now the added mass will be frequency depended and variations in the added mass relative to the matrix presented in 4.1.1 must be expected. It is considered acceptable to develop the ROV control system with the frequency independent dependent added mass, despite the weaknesses previously mentioned. This is because, the phases where the added mass and damping will be least accurate is phases that have a relative short duration. Furthermore this is not a phase where the highest requirement to the accuracy of the control system is required. The added mass will be frequency dependent as a result of wave action, where the larger and longer waves will create a larger effect. For many ROV systems there are limits to the sea state where the ROV can be launched for safety reasons. This is another reason why the frequency dependency will only have limited effect on the ROV, and for most cases can be ignored. If the ROV is operating at shallow water, where the depth is less than half the wavelength, the waves will affect the ROV and the accuracy of the calculated added mass can be reduced.

5.1.2 Damping

The linear and quadratic damping coefficient was determined for each DOF by curve fitting data from CFD. The resulting damping function is presented in figure 4.1.1 and 4.1.2. As can be seen in these figures the density of the data point were closer at lower speeds. This was done in order to get high accuracy at the low speeds. Ideally more data point should be used, but it is expected that the 8 data point would be sufficient to accurately describe the second order equation of the damping function. This is will be the case if the damping of the vehicle accurately can be modelled by a second order equation. Based on the result it can be seen that all data points lie close to the resulting damping function, something that support this hypothesis. It is however possible that at larger velocities turbulent flow around the vehicle can reduce the accuracy of this model where more viscous and nonlinear effects can be come more important. This is however not of great importance since the ROV is expected to be moving at relative low velocities, and within the range of velocities tested in the CFD analysis.

The damping matrices contain the coefficient of the damping function described by 2.2.25 is presented in equation 4.1.2 and 4.1.3. As previously presented the damping of the ROV cannot be negative, as this would be nonphysically. This does means that all the terms in the linear damping matrix and quadratic damping matrix must be positive. For very low velocities the quadratic terms will vanish, and a negative linear term will result in negative damping. Similar argument holds for the quadratic term for large velocities. In equation 4.1.2 it can be seen that several of the diagonal terms of the linear damping matrix \mathbf{D}_L is negative. The damping function $\mathbf{D}(\nu)$ presented in figure 4.1.1 and 4.1.2 appear to be positive for all values. By close inspection it is evident in figure 4.1.3 that 4 of the DOF's will have negative damping for small velocities. This is unphysical and will not accurately represent the forces on the ROV at low speeds. This indicates that at low speed the model

of the damping as a quadratic equation might be invalid. The result from the CFD analysis can be seen to all be positive, and it is the least square curve fitting that result in a negative damping. One possible approach that could be used to more accurately determine the damping could be to gather more data points within the relevant region of velocities, and on the basis of this use a curve fitting, interpolation or piecewise interpolation / Spline interpolation. This is not done in this thesis, but instead left as a recommendation for the further development of the control system. The effect of this inaccuracies will be limited, since the negative damping will, as seen in figure 4.1.3, only be relevant for very low speed. Here the magnitude of the damping will be small, and the largest possible negative damping for any DOF is less than $-0.5[N]$. Figure 4.1.1 and 4.1.2 illustrate that the damping function closely follow the remaining data point, and the calculated damping matrices can therefore be used, despite some inaccuracies at low speeds. Negative values of the linear elements was also observed in [13], and this highlight that the damping for an ROV can be difficult to estimate with CFD.

It is reasonable to expected that the linear term would be smaller than the quadratic term in the damping function, and the quadratic damping would dominate. This is also observed in both [13] and [11] that both treat hydrodynamics for different ROV's. The results presented earlier show a very large difference between the linear and quadratic part of the damping, and is a much larger difference than the results of the former mentioned theses found. This might indicate a weakness in the CFD analysis or the calculation of the damping coefficients. On the other hand, the ROV Minerva 2 have a more complex shape than the former ROV's and it is reasonable to assume that the damping will be more nonlinear. In this thesis the linear damping was for all ROV's more than one order of magnitude smaller than the quadratic term. For many of the elements the difference was significant more. On the basis of this it appears that the results obtained from the CFD analysis presented in chapter 4 is reasonable, and in accordance with other similar analysis. However it can be expected that the calculated damping it will differ somewhat from the true values.

The damping matrices can be compared to the matrices found for ROV Minerva, presented in [11]. Minerva 2 is essentially a larger version of the original Minerva. The damping matrices for ROV Minerva 1 is presented in Appendix F. It could be expected that both damping matrices would be larger for ROV Minerva 2. It is observed that the quadratic damping is larger for Minerva 2, but the linear is significantly smaller. This can indicate that CFD program underestimate the linear damping, at the cost of overestimating the quadratic damping. This should be further investigated before conclusive remarks are made.

In the damping function presented in figure 4.1.1 it can be that the heave damping have the largest value. This is a reasonable result considering the geometry of the ROV. In both surge and sway motion the water can flow through the vessel, and less water will move when the ROV moves, and thus less energy is removed from the system. From the top the ROV appears more or less solid, and water will have to flow around the flotation block or the bottom plate of the ROV. This is a common result for ROV's with this kind of geometry. Similar result was observed in [13] for an ROV from the same manufacturer as Minerva 2.

The density of the ROV can be understood as a measure of how large part of the projected area is open through the ROV. The density of the ROV will be more or less identical in surge and sway direction. As the ROV is longer than it is wide, it is reasonable that the sway damping also is greater than the surge damping. This can be seen both in the damping matrices and in the figure of the damping functions 4.1.1. For the rotational DOF's it is seen that the roll and pitch mode have higher damping than yaw. This is also a logical result based on the geometry of the ROV.

5.1.3 Experimental Test

The experimental test was performed on a model of the ROV Minerva 2. The result from this test was not sufficiently good to calculate the added mass coefficients. The experiment was performed by towing the model at different velocities and accelerations and measure the forces on the ROV. This was replicated for the same setup, but without the model present. The net force on the ROV could then be obtained by subtracting the forces on the mounting rig from the forces measured with the model. It was seen that for many of the test the forces without the model was larger than for the test where the model was present. This is a surprising result, that is not in accordance with expectations. It is physically possible for the forces to be smaller with the ROV, if the model of the ROV would help to round off the bottom of the mounting rig, and thus reduce drag. However for this experiments the result should have showed that the force had increased, as presence of the ROV could not reduce the drag. The cause of this can be calibration of the force sensors, and disturbances on the experiment. The larger force for the rig, than for the model, was most relevant for the yaw motion. For these measurement the measured force was relative small, and the noise-measurement ratio was relatively high. This is also something that can explain the result.

The initial plan was that the force sensors would be placed at the centre of the fastening rig, so that moments would not interfere, and only the forces in x and y directions was measured. This would require more sensors that was not available. Furthermore it was not possible to mount the sensors at the centre. Since the ROV had a port-starboard symmetry it would be expected that motion in surge would not cause any forces in sway direction or any yaw moments. Figure 4.1.4 clearly shows that this was not the case. Both sensors measure forces during the tow of the model in surge direction. This can either be the result of forces acting on the ROV in sway direction during this test or a yaw moment is causing the measurement. One other possibility is that the sensors alignment is off, so that they are not directed perfectly in x or y direction. The later could either be cause by the sensor installation, or due to an incorrect orientation of the ROV relative to the mounting rig. There could also be an error with the calibration of one or both of the force sensors.

The towing test was performed with the ROV facing down the towing tank. It is possible that the ROV had rotated slightly relative to the mounting plate, see figure 3.1.9, and since the sensors were mounted on the plate at the top of the rig seen in this figure, the alignment of the sensors would be incorrect. Since this plate was

installed underneath the towing carriage, as seen in figure 3.1.12, the orientation of the bracket could not easily be seen. It is considered as unlikely that there was any significant forces in the sway direction during the towing test, but the lack of symmetry and the imperfections of the model means that there is possible that a yaw moment can have been introduced. Since both of the force sensors are placed with a distance relative to the centre of mounting rig, a yaw moment will be measured as a y and x force by the sensors. It is likely that these effects discussed above have affected the measurement during the experimental test, leading to the reduced quality of the result.

The resulting damping coefficients calculated for the surge direction presented in table 4.1.2 and 4.1.3 is seen in the expected order of magnitude. The calculated damping coefficients can be compared with the once calculated with the CFD analysis. The CFD analysis seem, as discussed earlier, to underestimate the linear term, and over estimate the quadratic term. However, for the experiment, similar observations are made. As previously mentioned the accuracy of the calculated damping from the experiment is limited. For all DOF's a negative linear term is observed. This is a more understandable result for the experimental test, than for the CFD analysis, and a net negative force can be measured, if the forces of the mounting rig is larger than on the model. When the result from the model is scaled the velocity is decided by the scaling coefficient and the force is multiplied by a power of the scaling factor. This also highlights a weakness of the Reynolds scaling. Ideally the towing velocity should have been significantly larger, and have the same velocity range as the CFD analysis. There are limits to the velocity of the towing carts that made this impossible. For hydrodynamic towing test, Froude scaling is more commonly used, and the scaling of velocity is one of the reasons for this. For many towing test the viscous effects are not essential, and wave effects are considered as more important, something that makes froude scaling more relevant. For ROV's the damping will be dominated by the viscous effects. The experiments could be performed with a froude scaling. This could potentially give good result for the added mass. However, in order to isolate the added mass term the damping must be accounted for. It is therefore considered as most appropriate to use Reynolds scaling for an ROV. One weakness of this is that effects of waves are incorrectly scaled. For a real ROV this is not a problem, since this effect is negligible. For a towing tank test the ROV cannot be submerged at a deep depth, so that surface effect can have an effect on the measurement. This will however only have limited effect, and is ignored in this experiment.

One other possible error in the experimental setup related to the can be the position where the ROV is fastened. Ideally the model should be fastened at the centre of gravity of the model. This centre of gravity was found for the computer model, the model is based on. However simplifications and imperfections in the model mean that this centre of gravity might be displaced. This can also be a source of yaw moments corrupting the force measurements. In the calculated damping for all three DOF's tested, it is seen that the results are unphysical and inconsistent. On the basis of this it the computation of the added mass was not performed, as it would not yield anything of value. The added mass would have been found by subtracting the damping forces on the model from the force measured in the acceleration test.

The result would be only the mass forces remaining. The rigid body mass could be subtracted from this again, leaving only the added mass. The added mass could be considered as constant for all DOF's. For each towing test of the ROV where acceleration is tested, an added mass would be found. The average value could then be used for the added mass.

The added mass found from Wadam can be considered as relatively reliable. Some more uncertainties are related to the calculated damping. Ideally the experimental test would be able to provide input to this, either with values that supported the CFD and Wadam calculating, or that contradicted it. The result from the experiment show some similarities with the results obtained from the CFD. However, since the accuracy of this experiment is limited further research should be conducted before a conclusive damping function is defined. If a new towing test is performed to calculate the hydrodynamic coefficients there are opportunities for some improvements. Firstly it is recommended that 3 sensors are used. A setup should be designed so that two sensors can be mounted at the centre of the rig, only measuring the surge and sway forces. The remaining sensor will be able to measure moments. Secondly a new mounting bracket should be designed. The designed should be based on the existing configuration of the laboratory. With these modifications it is reasonable to assume that sufficiently good measurements can be obtained to calculate the hydrodynamic coefficients with an acceptable accuracy.

5.2 Control System

5.2.1 Thrust Allocation

The simulation of the thrust allocation where an increasing pure sway force is desired is presented in section 4.2.1. Sway force is increasing from the start of the simulation, to the end where it exceeds the saturation limit on the thruster. The most important objective of the thrust allocator is that the allocated thruster speed correspond to the forces that are desired. Figure 4.2.2 present the difference between the forces corresponding to the allocated thruster speeds and the desired thrust. For all methods presented it can be seen that this error is zero for most part of the simulation. Method 3, which is developed by removing one thruster will be the first method to reach saturation, as it will have a reduced maximum sway force. The remaining method reach saturation, where the error will start to grow, at the same time. In this respect only method 3 underperforms, and for very good reason. It is worth noting that method 3 is only used as a comparison as a simple solution to the thrust allocation problem.

The resulting thruster speed is presented in figure 4.2.3-4.2.7. Method 3 in figure 4.2.7 present the only possible solution this method can provide. Method 1 in figure 4.2.3 will only optimize the thrust allocation with respect to minimise negative thrust on the two frontal thrusters, thruster nr 1. and 2. This is achieved by only applying negative thrust on thruster 2 after the first set of thruster have reached saturation, and the only option left is to use negative thrust on thruster 2. This result is similar to the result obtained with method 2, where the cost of energy from negative thrust

on thruster 1. and 2. have been artificially increased. When arbitrate large values of S , this method effectively becomes an optimisation to minimise the negative sum of thruster 1. and 2. and not an energy optimisation. Figure 4.2.6 present method the thruster speed using method 2 without modifying the weighting parameters. The result is a solution that only optimise energy. By tuning the weighting parameter S a balance between how much it is needed to prevent negative thrust on thruster 1. and 2. The result is a balance between a solution that is optimal with respect to energy and with respect to minimum negative speed on thruster 1. and 2. This is evident in figure 4.2.8 and 4.2.9. Method 1 and method 2 will yield similar result, for the reasons previously mentioned. Method 3 have both a poor energy performance and performance with respect to preventing water from being flushed in front of the cameras. When method 2 is used without modifying the weighting parameter, the optimal thrust allocation with respect to energy is obtained, as seen in figure 4.2.8. This is however a trade of, as more water is flushed in front of the cameras, and the line in figure 4.2.9 lies above the remaining methods except method 3.

It is clear that both of the proposed method, method 1 and 2 performs better than the benchmark test, method 3. Method 2 is the more elegant solution to the thrust allocation problem, and is more flexible than method 1, which only minimise negative thruster speed on thruster 1. and 2. One weakens of method 2 is that this the negative values for thruster 1 and 2 are not set to be zero, even if that is what is desired. To achieve this, the weight of the energy would need to be infinite, but this would not work for the thrust allocator. The large S value only means that the energy from negative thrust cost S times more than for the other thrusters. The result is that small, but nonzero values for thruster 2 is selected in the test presented in section 4.2.1. This negative value is however so small that it will not appear on the figures, and it is also to small for the thrusters on the ROV to activate. This is the reason why a large value of $S = 10^8$ is selected. Even larger values could further decrease the magnitude of this small nonzero value, but with the value of 10^8 the result is sufficiently small to be neglected. On the basis of this was method 2 chosen for the ROV control system, and implemented in LabVIEW and the control system Njord.

5.2.2 HIL Simulation 1

A simulation of the control system was the control system was performed to ensure that the implemented modules such as the thrust allocator, and the changes made to modules such as the controller worked as intended. For this simulation it was decided that the desired roll and pitch angles would be zero. This was chosen as the most realistic setting for a real mission, and the aim of the simulation was to closely simulate a real mission. One benefit of this choice is that the potential challenges with the attitude observer for roll and pitch angles outside the valid interval is avoided. The result from the HIL simulation with the control system is presented in section 4.2.2

The result from this simulations generally show that the control system is able to perform the tracking mission as planed. Some offset is observed between the ob-

server and the estimated states. The control algorithm will use the states calculated by the observer, and it is these states that is attempted to be controlled to the desired states. The offset between the observer calculations and the measurement indicate that there are some errors in the observer estimation. The reason for this is an error in the implementation of the simulation of the magnetometer, which takes place in a different part of the control system, not treated in this thesis. The observer is designed to "trust" the DVL and magnetometer measurement, and when the magnetometer measurement is incorrect, the positioning will be incorrect. The magnetometer is a part of the HIL simulator, and work on this component is outside the scope of this thesis. This measurement will therefore create an incorrect estimate of the position from the observer. The observer is not treated in this thesis, and for the purposes of this project the observer is treated like a black box. Since the control system use the observer values, the calculated thrust will drive these states towards the desired values. At the same time, since the observer values does not coincide the thruster will not control the estimated states, but the real ROV providing the measurement. This inconsistency explains the offsets that can be seen, and all offsets in the tracking occurs when the difference between the observer and the measurement increase. This is especially evident in figure 4.2.10 where the offset between the observer and the estimation grows after a new waypoint is given. This offset also causes the tracking to be off. However, the estimated states show that the control system is able to maintain a relatively good tracking despite of these offset. It is also worth taking into account that these offsets are relatively small, in comparison to the vehicle size and the tracking mission.

The offset between the observer values and the measured values can clearly be seen in the plot of the motion in north direction 4.2.11. The offsets become large after each way point. It is also evident that the controller and thrust allocator is able to perform the designated tasks, as the estimated states closely tracks the desired states.

5.2.3 HIL Simulation 2

Section 4.2.3 presents a second HIL simulation, where environmental disturbances of waves and currents was simulated. The purpose of this was to determine how the control system was able to function under more realistic conditions. For this simulation the ROV was programmed to keep a heading north for most of the simulation. The purpose of this was to reduce the effect of the error in the magnetometer calibration. The error in the magnetometer calibration will affect the system as a form of a strong disturbance. The heading was deliberately kept such that the effect of the magnetometer would be lowest possible, and then the effect of the wave and current can be tested. For the last waypoint, the heading was changed to give a comparison of how the different disturbances affect the system. It can clearly be seen that the effect of the environmental disturbances have the largest effect at the beginning of the simulation. At this point the ROV is at shallow water, and the water velocity due to waves will be more important at this depth. The large pitch and roll motion at the beginning of the simulation can also be explained by the wave action on the ROV. This is supported by the observation that the pitch

motion is more or less constant when the ROV maintain one position. Furthermore the lowest pitch motion is seen between the simulation time 50 and 120, as seen in figure 4.2.20. This is the time the ROV maintain its position at depth of 30m. In the period between simulation time 150 to 210 the pitch motion have an oscillation with a constant magnitude. This is seen together with a lower depth of the ROV, where the wave forces will be larger. The ROV reach the deepest depth after simulation time 250, as seen in figure 4.2.19. In figure 4.2.20 it can also be seen that the oscillation in pitch fades out almost completely at this point.

The effect of the current is more difficult to observe. This indicate the the motion control system is able to observe. The effect of the current will be expected to push the ROV off position. From figure 4.2.16 it can be seen that once the ROV reach the waypoint they are able to keep this position relatively accurate. This can also be seen in figure 4.2.17, 4.2.18 and 4.2.19. As the ROV is able to maintain it's position despite current acting on the vessel is an indication that the ROV motion control system is functioning as intended, and that it have a good performance. At the beginning of the simulation, the ROV have an offset to the desired position, and is to far south. This cannot be explained by the effect of current, as the current would force the ROV in the opposite direction. Instead, this offset might be the result of the wave action or transient behaviour in the beginning of the simulation, before the controller and observer have had sufficient time to converge.

The station keeping capabilities of the ROV can best be seen in figure 4.2.17, 4.2.18 and 4.2.19. In these figures three plateaus can be seen between simulation time intervals [50, 120], [150, 210] and from simulation time 250. The first two plateaus show that the station keeping capability of the ROV is accurate despite the actions of waves and current. By close inspection of the figures it can be seen that the largest offset occur as the ROV reach the DP point. After some time the offset is reduced in magnitude. The largest offsets to the DP points are [20[cm] 15[cm] 20[cm]] for North-East-Down respectively.

5.2.4 Magnetometer Error Test

In the HIL tests presented in section 4.2.2 and 4.2.3 some offsets was observed between the estimated and measured position in north and east direction. This was believed to be a result from a known problem with control system, originating from a calibration error in the implementation of the magnetometer. The simulation test in section 4.2.4 was performed with the purpose of determining whether the offsets was caused by the magnetometer calibrations. The error in the heading from the magnetometer due to error in the implementation would be expected to be insignificant at heading around north, and the error would increasing when the heading changed towards east.

The result from this simulation is presented in figure 4.2.22, 4.2.23 and 4.2.24. By comparing the performance of the system before and after the heading was changed from due north to east, the error in the positioning can be seen to significantly increase. From figure 4.2.23 the performance of the tracking in north direction in the first section after the heading was changed before the heading was changed be

seen to be close to the performance before the heading was changed. On the other hand the tracking in east direction for this part is significantly worse. Similarly for the section between the last two way points, the performance of the tracing in north direction is bad, while the east direction is better. Physically this means that the cross track tracking of the ROV is much worse than the along track motion. This can clearly be seen in the north-east plot in figure 4.2.22. This is a reasonable result with an inaccurate heading measurement. This can be understood by considering the vertical and horizontal displacement when a line is displaced by a small angle. A simple sketch of this was created in figure A3, and attached in the Appendix E. In this figure the blue box represent the ROV. The black line indicate the motion the ROV is desired to have. The red line correspond to the real motion of the ROV as a result of the heading error. The along track displacement Δx is seen to be significantly smaller than the cross track error Δy .

It is also worth noting that one reason why the along track error will be less than the cross track error is that desired position will move with the ROV towards the next waypoint. For the cross track direction this will instead directly translate to an error, as the cross track desire value will remain constant. This correspond well with the observations made in figure 4.2.23 and 4.2.24. The figures in section 4.2.4 have some significant motion along track of the tracking objective. In figure 4.2.25 it can be seen that both the estimated and measured yaw motion indicate very little motion in yaw. This can be a result of the errors in the magnetometer calibration. The result is that the ROV "thinks" it is on the correct course, when in fact have a heading offset. The result is some undesired motions. The result from the simulation is in accordance with the expectations of the system when the magnetometer measurement is incorrect, and support the claim that the errors observed in HIL simulation 1 and 2 are due to this calibration error. This was not attempted to be corrected, as this is outside of the scope of this thesis.

5.2.5 Joint Autonomy Simulation / Virtual Integration Test

The joint autonomy simulation, where a virtual integration test of the control system, sonar tracking and camera tracking was performed is presented in section 4.2.5. The result from this test show that the control system is able to complete the mission, but the accuracy is limited. Figure 4.2.26 is showing the motion of the ROV in the north-east plane. The tracking of the desired position can here be seen to be somewhat inaccurate. As previously mentioned this can partly be explained by the error in the magnetometer. The offset between estimated position and the measured position starts of relatively small, but increase in the tracking phase. The point where the ROV change from the first waypoint to the second can clearly be seen, where the measured position have an offset of almost $2m$. Here it can be seen that the vessel is moving in a direction found from the measured position, is very different from the direction that can be observed from the estimated position in figure 4.2.26. In this figure the heading angle does not necessarily equal to the direction of motion. At the point where the first waypoint of the transit phase is reached, and the direction is changed, the direction of motion from the measured position is almost due east. The same direction found from the estimated state is in

the north-east direction. This is a significant offset, and indicate that the measured heading is significant different from the true heading of the ROV, something that highlight the error in the magnetometer. If this effect is removed, it is reasonable to believe that the performance would be significantly better.

The plot of the motion in north and east direction is presented in figure 4.2.27 and 4.2.28. The desired position of the ROV is observed as the red line. In the plot of the motion in east direction can be seen to have a notch. At this notch the ROV is not able to follow the desired state. This notch is a result of a delay between when the first sonar tracking waypoint was reached by the ROV, and when the second waypoint was sent to the system. This also explain the short plateau seen between the first and second sonar tracking waypoint observed in the plot of the motion in the north direction.

Figure 4.2.29 present the motion of the ROV in the vertical direction. Here the tracking is substantially better, with an maximum offset of less than $2m$ for the part of the simulation until the sonar tracking is activated. This happens at around simulation time 90. After this, the desired state is seen to oscillate, and the motion of the ROV in the vertical direction oscillate. The heave motion of the ROV oscillate out of phase compared to the desired state, indicating that the heave motion is somewhat slow. In this part, the desired depth of the ROV is calculated in a part of the autonomy code that have not been considered in this thesis. On the basis of the observations made in figure 4.2.29 it appears that there are some errors in this code. This part of the autonomy code is outside of the scope for this thesis, and it was not possible to resolve this problem with the time frame available. This appears to be an error that first have been discovered when the sonar and camera tracking have been introduced. The depth of the ROV is determined separately from where the way points are defined in the autonomy code. This have probably not been tested for the camera and sonar tracking before. Aside from this, the tracking in the vertical direction is acceptable, but not perfect. Most of the ofsetts between the estimated and the desired position for this motion is when the estimated state is lagging behind the desired state. This can be a result of to slow movement in the vertical direction, or to fast movement of the tracking objective. This can be considered as a more acceptable and understandable form of an offset, since the ROV will arrive at the desired depth, but it take some time for the ROV to get there. It is possible that the performance of the ROV can be improved further by tuning the controller gains for the heave direction, or by preventing the autonomy system from outputting an oscillating desired depth.

The rotational DOF's are presented in figure 4.2.30. The roll and pitch motion is kept relatively low, with both being limited to only small angels. In the figure it can be seen that the control system is first activated after a simulation time of 10. At this time the desired roll and pitch angle is given. This explain the sudden jump in the red line, "desired position", that can be observed in figure 4.2.30. Some roll and pitch motion can be seen for the remainder of the simulation, but the motion is relatively small. The tracking of the yaw motion is seen to be very precise. This indicate that the control system is able to obtain the desired position. As previously mentioned, the measured heading angle is incorrect. This cause the estimated

heading to be incorrect as well. This should be taken into account when evaluating the performance of the control system. The yaw motion is the cause of much of the inaccurate tracking that is visible in this simulation. However, the control system is only able to act on the basis of the estimated states. On the basis of this the tracking of the yaw angle can be considered as good. During the transit phase some oscillations are observed between the estimated yaw angle and the real yaw angle. This is only present once one waypoint is reached, and the desired yaw angle change, and the angle approach the desired yaw angle over time. This is however an indication that the controller is tuned sub optimal. This is something that should be improved in a future iteration of the control system.

5.3 System Identification

The system identification is a new functionality under development for the new ROV. The result from simulation test both with nonlinearities shows promising results. The two simulations presented in section 4.3.1 and 4.3.2 shows that the approach outlined in section 2.4 can be used to calculate the mathematical model of an ROV, with a relatively high level of accuracy. Some inaccuracies will always be present. One feature that is not included in these analyses is noise and disturbances on the system. This is something that will affect a real ROV, and it can be expected to reduce the quality of the results. There are some methods that can be used to overcome this. The simplest approach will be to use the values from the observer on the ROV. If this observer is functioning as it is supposed to, this will filter out noise and disturbances. With such an approach the current system can more or less be directly applied for the ROV. One prerequisite for this to be done is that the system identification must be programmed into LabVIEW.

Simulation A, is an optimal scenario for the developed system identification. Here all the states are known, there are no noise, disturbances or nonlinear terms. The results are exceptionally good where the largest error in the mass matrix is $0.01[kg/m]$. For a mass matrix where the terms have values above 3000, an error of $\frac{1}{100}$ is a more than good enough result. The two damping matrices presented in appendix B show similar results. One factor that can influence the result is the duration of the simulation. The longer the simulation, the more data is obtained. Since the system identification is based on a least square curve fitting, more data points will give a more accurate representation of the system. The primary purpose of simulation A, was to verify that the system identification program would function as desired.

Table 4.3.1 summarises the differences between the calculated damping matrices and the real damping matrices for simulation B. The error in the two damping matrices is seen to be relatively small. The largest error in the linear and quadratic damping matrix, relative to the largest real damping element is 0.52% and 0.51% respectively. On the basis of this it is seen that the system identification is able to accurately calculate the damping matrices on the basis of the motion of the ROV, and the forces imposed on it. The result from the calculation of the mass matrix was also found to be satisfactory, although error in the calculation was significantly larger than for the damping matrices. Along the diagonal terms the largest error

was observed to be $15[kg]$. This was observed at position 3,3 in the matrix, where the real value were be supposed to be $10111[kg]$. In this context a $15[kg]$ error is not an significant error. The overall largest error at $50[kgm]$ was found at an off diagonal term. Although this is a significant error, the effect of this will only be limited, since the other terms have a significant larger magnitude, and will dominate.

The result from the system identification when data from a HIL simulation of the ROV and control system is used are presented in section 4.3.3. The result shows that the system identification is able to calculate the mass of the system. The error in the mass can be seen to not exceed $6[kg]$ for all degrees of freedom, as can be seen in matrix 4.3.4. The result from the linear damping matrix is also accurate, whit the maximum error of $15[kgs]$. The average error is less than $1[kgs]$, which must be considered to be considered to be sufficiently accurate. With the assumption that the linear damping matrix is diagonal, these elements will be the most important. For these elements the average error is $0.1775[kgs]$, and the maximum error in the linear damping matrix on the diagonal is $0.7250[kgs]$ for the surge motion.

The result for the quadratic damping matrix is somewhat less accurate, compared to the mass matrix and the linear damping matrix. The diagonal terms in the quadratic damping matrix have an acceptable accuracy, as presented in table 4.3.2. For the off-diagonal terms the errors become more prominent. The error is seen to be as large as $500kgs$ for some terms. Both of the terms with an error larger than $50[kgs]$ are found in the third column related to heave motion. This can originate from some error in the modelling of the restoring force in the heave direction. This could potentially reduce the accuracy of the calculations of the coefficients related to heave motion. If this was the case, it could be expected that the an error could be observed for all of the three matrices. The error in the quadratic matrix can also be explained with some error in the velocity measurement. As previously presented in this thesis some errors have been uncovered in the measurements obtained from the HIL simulator. This is however mostly related to the yaw motion. By inspection it can be seen that the largest error in both the diagonal damping matrix and some of the largest errors in the mass matrix are found in the third column. This indicate that the error is related to restoring force calculated for the heave motion. The current version of the system identification program were supposed to model the restoring forces identically as they are calculated in the HIL simulator. However there might be some errors in this implementation. This is supported by the fact that the error is only observed for simulation C when the restoring force is included. This require further investigation, and work to optimise the performance of the system identification should be continued.

Despite some errors in simulation C the result from the system identification test shows generally good and promising results. Using a linear system identification, on the nonlinear system seems to be a valid approach. One significant weakness of this approach is that a priori knowledge of the mass and added mass of the vehicle is needed to calculate the Coriolis and centripetal rigid body and added mass force. However this force is generally speaking a smaller force, especially at low speeds, at which it is relevant to run a system identification. Furthermore, one approach to deal with this can be to be to have a set of standard starting values for the mass and

added mass, that is used to calculate the Coriolis added mass in the first iteration. This can for example be the values found in section 4.1.1. The second iteration can use the values calculated from the first iteration, and from this an iterative procedure can be performed until the result converge.

Chapter 6

Conclusion

An advanced motion controls system have been developed for the ROV systems at NTNU. In this thesis the control system have been developed for the ROV Minerva 2. The hydrodynamics of the vessel have been obtained by numerical computation and from experimental test. In addition to this a test and evaluation of the potential of applying system identification as a function in the control system to calculating the mathematical model of the ROV. The resulting motion control system is a system that is able to control the ROV. As such the overall goal of the thesis was reached.

The results from the hydrodynamic analysis was verified against empirical data. Empirical data and numerical computation showed good correspondence. This indicate that the resulting hydrodynamic coefficients calculated with numerical tools are reasonable accurate. The comparison of the added mass calculation shows that the added mass for the translational motion correspond well with the numerical computations. For rotational added mass strip theory is used on empirical data. The result was corresponding to a lower degree than for the translational motion, but was still relatively good. The hydrodynamic analysis resulted in a model of the ROV that could be used by the control system. The calculated damping was somewhat different from the expectations. The calculations resulted in a very small linear term and a large quadratic term. An experimental test was performed, with the intentions of obtaining more estimates of the added mass and damping. The measurements obtained from this test was seen to be polluted by noise, and some unexpected force measurements. It is assumed that the installation of the sensors along with calibration of the sensors, yaw moments during towing and imperfections in the model was the cause of the poor result for these test. It is recommended to perform new towing test of the model to obtain an experimental estimate of the hydrodynamic parameters. The damping coefficients that was calculated on the basis of the measurement from the experiment seems to be in the same order of magnitude as the once calculated with the CFD analysis. Further analysis should be performed on topic area to ensure a more accurate damping is determined.

The control system was developed to a state where it can be used on the new ROV. The new thrust allocation deals with the new situation of having an over-actuated ROV. The thrust allocation is developed under the goal of both minimizing the total propulsion energy and preventing water from being flushed in front of the cameras.

This was achieved by using an optimisation algorithm. The thrust allocation together with the extension of the controller to control roll and pitch was the major developments made in the control system. In addition to this an extension to the autonomy code have been made to make it possible to use sonar and camera tracking on the ROV. Simulations of the control system was performed, and indicate that the control system is able to accurately manoeuvre the ROV. Some errors were identified in different parts of the control system not treated in this thesis, that affected these simulations. Despite these errors, the simulations showed generally good results.

The prospect of applying system identification as a function to determine the mathematical model of the ROV, have been evaluated in this thesis. A system identification function was developed as an external program, and was tested with multiple simulations, including a HIL simulation from the ROV motion control system. The results show that the system identification the proposed system identification design can be used to determine the matrices used to describe the motion of the ROV, with relatively good accuracy. Some difference between the real values and the calculated values was seen. This became more apparent for the more complex models. Despite this, the system identification was able to calculate the diagonal terms for all simulation with a high level of precision. The result clearly shows that system identification can be applied for the ROV motion control system, but a full implementation will require more work than what is possible in this thesis. This thesis shows that a linear approach to system identification can work well, but this approach is based on assuming an starting value of the mass and added mass, and iteratively solving the system identification until the mass matrix converge.

6.1 Further Work

The ROV control system is a project under continuously development. The idea of this system is to gradually improve the system, and to have an ever more advance ROV control system. For the control system for ROV Minerva 2 there are several useful developments that can be made. For the hydrodynamics, more CFD analysis can be performed on the ROV. From this a more accurate damping function can be obtained. As shown in the result in this thesis, modelling the damping function as a quadratic function can lead to negative linear damping coefficient. This cause the damping at low speed to be negative. Instead, by obtaining more datapoints the damping can be determined using some higher order polynomial, or by representing the damping as a piecewise polynomial function, like a spline. This can result in a more precise representation of the damping. A second experimental test with towing of the ROV should also be performed, but with a mounting rig designed from scratch for the current configuration in the towing tank and with a better sensor suit.

In the control system, the desired roll and pitch angles should be introduced to the guidance system. As it stands now, the desired roll and pitch are directly fed into the controller. When the values are changed a step response will be obtained. For the current version of the control system this is not a problem, as the main goal is to control the roll and pitch to zero degrees. For the thrust allocator, the thruster

coefficients K should be determined through experimental tests and updated in the system. It is also recommended that the controller parameters should be further tuned to obtain a better performance.

As mentioned it is recommended to implement the system identification in the control system. A functionality should be included in the GUI, where the user can manually initiate a system identification mode. Furthermore this system should be extended to directly calculate the nonlinear model. The result from the system identification can also be improved by extending the observer in the control system. For the system identification, it can also be interesting to investigate nonlinear methods, so that the Coriolis forces can be directly accounted.

Bibliography

- [1] *Research Vessel R/V Gunnerus*. The Norwegian University of Science and Technology, <https://www.ntnu.edu/oceans/gunnerus>, Accessed: 04.06.2018.
- [2] *The Applied Underwater Robotics Laboratory*. The Norwegian University of Science and Technology, <https://www.ntnu.edu/web/aur-lab/aur-lab>, Accessed: 24.05.2018.
- [3] R.D Blevins. *Applied fluid dynamics handbook*. Van Nostrand Reinhold, New York, 1984.
- [4] M. Candeloro. *Tools and methods for autonomous operations on seabed and water column using underwater vehicles*, volume 2016:17 of *[IMT-rapport]*. Norwegian University of Science and Technology, Faculty of Engineering Science and Technology, Department of Marine Technology, Trondheim, 2016.
- [5] M. Candeloro, F. Dezi, A.J. Sørensen, and S. Longhi. *Analysis of a multi-objective observer for UUVs*, volume 3. IFAC Proceedings Volumes (IFAC-PapersOnline), 2012.
- [6] M. Candeloro, A.M. Lekkas, A.J. Sørensen, and T.I. Fossen. Continuous curvature path planning using voronoi diagrams and fermat’s spirals. *IFAC Proceedings Volumes*, 46(33):132–137, 2013.
- [7] M. Candeloro, A.J. Sørensen, S. Longhi, and F. Dukan. Observers for dynamic positioning of rovs with experimental results. *IFAC Proceedings Volumes*, 45(27):85–90, 2012.
- [8] M. Candeloro, E. Valle, M.R. Miyazaki, M. Ludvigsen, and A.J. Sørensen. Hmd as a new tool for telepresence in underwater operations and closed-loop control of rovs. *MTS/IEEE OCEANS*, 2015.
- [9] T.C Chiu. *Sonar tracking and obstacle avoidance for Navigation of ROV*. Department of marine technology, NTNU, 2018, (Unpublished).
- [10] NTNU compiled by: Department of Mathematical Sciences. *Differential equations, linear algebra and its applications*. Pearson, Harlow, 2012.
- [11] F. Dukan. *ROV motion control systems*, volume 2014:295 of *Doktoravhandlingar ved NTNU (trykt utg.)*. Norwegian University of Science and Technology, Faculty of Engineering Science and Technology, Department of Marine Technology, Trondheim, 2014.

- [12] F. Dukan, M. Ludvigsen, and A.J. Sørensen. Dynamic positioning system for a small size roV with experimental results. pages 1–10. IEEE Publishing, June 2011.
- [13] O.A. Eidsvik. *Identification of Hydrodynamic Parameters for Remotely Operated Vehicles*. Department of marine technology, NTNU, June 2015.
- [14] O.A. Eidsvik and I. Schjøberg. *Determination of Hydrodynamic Parameters for Remotely Operated Vehicles*. OMEA2016, 2016.
- [15] O.M. Faltinsen. *Sea loads on ships and offshore structures*. Cambridge ocean technology series. Cambridge University Press, Cambridge, 1990.
- [16] D.A. Fernandes. *An output feedback motion control system for ROVs : guidance, navigation, and control*, volume 2015:122 of *Doktoravhandling ved NTNU (trykt utg.)*. Norwegian University of Science and Technology, Faculty of Engineering Science and Technology, Department of Marine Technology, Trondheim, 2015.
- [17] T.I. Fossen. *Nonlinear modelling and control of underwater vehicles*, volume 1991:39 of *Doktor ingeniøravhandling (Trondheim : online)*. Universitetet i Trondheim, Norges tekniske høgskole, Institutt for teknisk kybernetikk, Trondheim, 1991.
- [18] T.I. Fossen. *Handbook of Marine Craft Hydrodynamics and Motion Control*. John Wiley Sons, Ltd, Chichester, UK, 2011.
- [19] T.O. Fossum, M. Ludvigsen, S. M. Nornes, I. Rist-Christensen, and L. Brusletto. *Autonomous robotic intervention using roV: an experimental approach*. Ocean’s 2016 Conference, 2016.
- [20] H.K. Khalil. *Nonlinear Control, Global Edition*. Pearson Education Limited, 2015.
- [21] A. M. Lekkas, M. Candeloro, and I. Schjøberg. Outlier rejection in underwater acoustic position measurements based on prediction errors. *IFAC PapersOn-Line*, 48(2):82–87, 2015.
- [22] N.F. Lillemoen. *Development of Software Tool for Identification of Ballast Errors in Autonomous Underwater Vehicles*. Department for engineering cybernetics, NTNU, 2014.
- [23] L. Ljung. *System identification : theory for the user*. Prentice Hall information and system sciences series. Prentice Hall PTR, Upper Saddle River, N.J, 2nd ed. edition, 1999.
- [24] M. Ludvigsen and A. J. Sørensen. Towards integrated autonomous underwater operations for ocean mapping and monitoring. *Annual Reviews in Control*, 42:145–157, 2016.
- [25] P. Matisko and V. Havlena. Optimality tests and adaptive kalman filter. *IFAC Proceedings Volumes*, 45(16):1523–1528, July 2012.

- [26] Standard Norge. Remotely operated vehicles (rov) services, norsok u-102, 2016.
- [27] S.M Nornes, A.J Sørensen, and M. Ludvigsen. Motion control of rovs for mapping of steep underwater walls. In *Sensing and Control for Autonomous Vehicles*, pages 51–69. Springer, 2017.
- [28] E. Omerdic and G. Roberts. Thruster fault diagnosis and accommodation for open-frame underwater vehicles. *Control Engineering Practice*, 12(12):1575–1598, 2004.
- [29] Committee on Autonomous Vehicles in Support of Naval Operations. *Autonomous vehicles in support of naval operations*. National Academies Press, Washington, D.C., 2005.
- [30] J. Pereira and A. Duncan. System identification of underwater vehicles. pages 419–424. IEEE Publishing, 2000.
- [31] B. Pettersen. *Hydrodynamikk, TMR4147 - Marin Teknikk 3*. Department of Marine Technology, NTNU, Trondheim, 2007.
- [32] I. Rist-Christensen. *Autonomous Robotic Intervention using ROV*. Department of marine technology, NTNU, 2016.
- [33] A. Ross, T.I. Fossen, and T.A. Johansen. Identification of underwater vehicle hydrodynamic coefficients using free decay tests. *IFAC Proceedings Volumes*, 37(10):363–368, July 2004.
- [34] DNV GL Software. Feature description - sesam, software suite for hydrodynamic and structural analysis of ships and offshore structures, 2018.
- [35] Solidworks. *Technical Reference, Solidworks Flow Simulation 2017*. Dassault systems, 2017.
- [36] S. Steen. *TMR7 - Experimental Methods in Marine Hydrodynamics*. Department of marine technology, NTNU, 2014.
- [37] A.J. Sørensen. *Marine control systems : propulsion and motion control of ships and ocean structures*, volume UK-2013-76 of *Kompendium (Norges teknisk-naturvitenskapelige universitet. Institutt for marin teknikk)*. Department of Marine Technology. Norwegian University of Science and Technology, Trondheim, 2013.
- [38] A.J. Sørensen, F. Dukan, M. Ludvigsen, D. de Almeida Fernandes, and M. Candeloro. *Development of dynamic positioning and tracking system for the ROV Minerva*. Institution of Engineering and Technology, January 2012.
- [39] Det Norske Veritas. *Recommended Practice DNV-RP-H103, Modeling and Analysis of Marine Operations*. Det Norske Veritas, 2011.
- [40] F.M White. *Viscous Fluid Flow*. McGraw-Hill series in mechanical engineering. McGraw-Hill Higher Education, Boston, 3rd ed. edition, 2006.
- [41] L. Xue. *Computer vision based autonomous panel intervention for a rov*. Department of marine technology, NTNU, 2018, (Unpublished).

Appendix

Appendix A: Table of Added mass coefficients

Figure A1 and A2 presents added mass coefficients for some geometries. The table is obtained from [39].

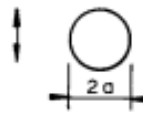
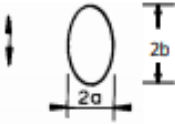
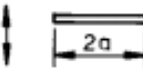
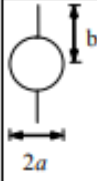
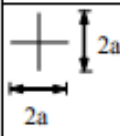
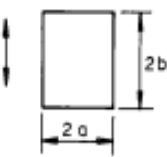
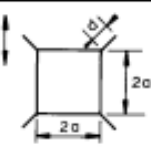
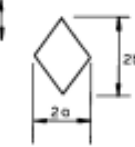
Section through body		Direction of motion	C_A	A_R	Added mass moment of inertia [(kg/m)*m ²]
			1.0	πa^2	0
		Vertical	1.0	πa^2	$\rho \frac{\pi}{8} (b^2 - a^2)^2$
		Horizontal	1.0	πb^2	
		Vertical	1.0	πa^2	$\rho \frac{\pi}{8} a^4$
 Circular cylinder with two fins		Vertical	1.0	πa^2	$\rho a^4 (\csc^4 \alpha f(\alpha) - \pi^2) / 2\pi$ where $f(\alpha) = 2\alpha^2 - \alpha \sin 4\alpha + 0.5 \sin^2 2\alpha$ and $\sin \alpha = 2ab / (a^2 + b^2)$ $\pi/2 < \alpha < \pi$
		Horizontal	$1 - \left(\frac{a}{b}\right)^2 + \left(\frac{a}{b}\right)^4$	πb^2	
		Horizontal or Vertical	1.0	πa^2	$\frac{2}{\pi} \rho a^4$
	a/b = ∞ a/b = 10 a/b = 5 a/b = 2 a/b = 1 a/b = 0.5 a/b = 0.2 a/b = 0.1	Vertical	1.0 1.14 1.21 1.36 1.51 1.70 1.98 2.23	πa^2	$\beta_1 \rho \pi a^4$ or $\beta_2 \rho \pi b^4$
					a/b
		Vertical	1.61 1.72 2.19	πa^2	$\beta \rho \pi a^4$
					d/a
		Vertical	0.85 0.76 0.67 0.61	πa^2	0.059 $\rho \pi a^4$ for a = b only

Figure A1: Analytical added mass coefficient for two-dimensional bodies, i.e. long cylinders in infinite fluid (far from boundaries). Added mass (per unit length) is $A_{ij} = \rho C_A A_R$ [kg/m] where A_R [m²] is the reference area, [39]

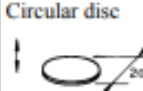
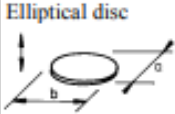
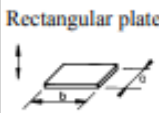

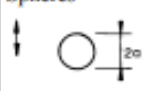
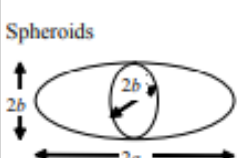
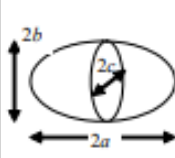
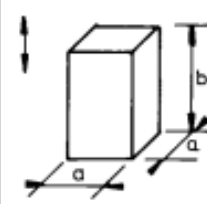
Body shape		Direction of motion	C_A				V_R
Flat plates	Circular disc 	Vertical	$2/\pi$				$\frac{4}{3}\pi a^3$
	Elliptical disc 	Vertical	b/a	C_A	b/a	C_A	$\frac{\pi}{6} a^2 b$
		∞	1.000	5.0	0.952		
		14.3	0.991	4.0	0.933		
		12.8	0.989	3.0	0.900		
	10.0	0.984	2.0	0.826			
	7.0	0.972	1.5	0.758			
	6.0	0.964	1.0	0.637			
	Rectangular plates 	Vertical	b/a	C_A	b/a	C_A	$\frac{\pi}{4} a^2 b$
		1.00	0.579	3.17	0.840		
		1.25	0.642	4.00	0.872		
		1.50	0.690	5.00	0.897		
		1.59	0.704	6.25	0.917		
		2.00	0.757	8.00	0.934		
		2.50	0.801	10.00	0.947		
		3.00	0.830	∞	1.000		
	Triangular plates 	Vertical	$\frac{1}{\pi} (\tan \theta)^{3/2}$				$\frac{a^3}{3}$
Bodies of revolution	Spheres 	Any direction	$1/2$				$\frac{4}{3}\pi a^3$
	Spheroids 	Lateral or axial	a/b	C_A		$\frac{4}{3}\pi b^2 a$	
			Axial	Lateral			
		1.0	0.500	0.500			
		1.5	0.304	0.622			
		2.0	0.210	0.704			
		2.5	0.156	0.762			
		4.0	0.082	0.860			
		5.0	0.059	0.894			
		6.0	0.045	0.917			
		7.0	0.036	0.933			
		8.0	0.029	0.945			
Ellipsoid	 Axis $a > b > c$	Axial	$C_A = \frac{\alpha_0}{2 - \alpha_0}$ where $\alpha_0 = 2\delta \int_0^{\pi} (1+u)^{-3/2} (\epsilon^2 + u)^{-1/2} (\delta^2 + u)^{-1/2} du$ $\epsilon = b/a$ $\delta = c/a$				$\frac{4}{3}\pi abc$
Square prisms		Vertical	b/a	C_A		$a^2 b$	
		1.0	0.68				
		2.0	0.36				
		3.0	0.24				
		4.0	0.19				
		5.0	0.15				
		6.0	0.13				
		7.0	0.11				
		10.0	0.08				

Figure A2: Analytical added mass coefficient for three-dimensional bodies in infinite fluid (far from boundaries). Added mass is $A_{ij} = \rho C_A V_R$ [kg] where V_R [m^3] is reference volume, [39]

Appendix B: Additional Result from System Identification, Simulation A

$$D_{L SysID} = \begin{bmatrix} 0.00061416 & -1.4077e-08 & 1.6393e-08 & 1.3155e-07 & -4.019e-07 & -6.2549e-08 \\ -2.2331e-10 & 0.007178 & 1.7357e-09 & 1.3358e-08 & -1.6492e-08 & -3.4878e-09 \\ -1.5661e-10 & -5.9187e-10 & -0.0033542 & 6.3539e-09 & -3.7072e-09 & -2.8804e-09 \\ -3.1066e-08 & -1.3727e-08 & 5.5115e-07 & -0.027048 & -3.2831e-07 & -5.6516e-08 \\ -1.5667e-08 & -2.7474e-08 & 1.3104e-06 & -2.3901e-07 & -0.12314 & 6.2148e-09 \\ -2.1789e-09 & -8.3326e-10 & 8.0562e-08 & -3.3243e-09 & -1.5806e-09 & 0.004557 \end{bmatrix} \quad (A1)$$

$$D_{L Real} = \begin{bmatrix} 0.00061416 & 0 & 0 & 0 & 0 & 0 \\ 0 & 0.007178 & 0 & 0 & 0 & 0 \\ 0 & 0 & -0.0033542 & 0 & 0 & 0 \\ 0 & 0 & 0 & -0.027048 & 0 & 0 \\ 0 & 0 & 0 & 0 & -0.12314 & 0 \\ 0 & 0 & 0 & 0 & 0 & 0.004557 \end{bmatrix} \quad (A2)$$

$$D_{Q SysID} = \begin{bmatrix} 6.2543 & 1.3908e-06 & 2.0824e-06 & -1.8525e-06 & 6.3454e-05 & 6.8349e-09 \\ -2.0245e-08 & 9.451 & 1.0777e-07 & -4.7232e-08 & 1.9435e-06 & -3.6752e-09 \\ 3.8364e-09 & -5.588e-09 & 22.683 & -9.7896e-10 & -7.9944e-08 & 3.2432e-09 \\ -3.0144e-08 & 4.8656e-07 & -1.6035e-06 & 11.188 & 1.6845e-05 & -3.9442e-06 \\ -1.7283e-07 & 1.3882e-06 & -6.7717e-06 & 1.5936e-06 & 38.677 & -9.1023e-06 \\ -1.3525e-08 & 9.5069e-08 & -4.2462e-07 & 1.0574e-07 & 2.7433e-06 & 9.4219 \end{bmatrix} \quad (A3)$$

$$D_{Q Real} = \begin{bmatrix} 6.2543 & 0 & 0 & 0 & 0 & 0 \\ 0 & 9.451 & 0 & 0 & 0 & 0 \\ 0 & 0 & 22.683 & 0 & 0 & 0 \\ 0 & 0 & 0 & 11.188 & 0 & 0 \\ 0 & 0 & 0 & 0 & 38.677 & 0 \\ 0 & 0 & 0 & 0 & 0 & 9.4219 \end{bmatrix} \quad (A4)$$

Appendix C: Additional Result from System Identification, Simulation B

$$D_L \text{ SysID} = \begin{bmatrix} 0.061687 & -0.0030854 & -0.0075598 & -0.0035147 & -0.0020038 & -0.0023435 \\ 0.00037781 & 0.71745 & -0.0063556 & -0.0092956 & 0.035614 & -0.00098127 \\ -0.001432 & -0.0036683 & -0.34824 & -0.0048455 & -0.026351 & -0.0015807 \\ -7.1277e-05 & -0.0037854 & 0.0098553 & -2.7043 & -0.063622 & -0.0014609 \\ -0.00037927 & -0.00045168 & 0.0099062 & -0.0064474 & -12.331 & 0.0011151 \\ -0.0012426 & 0.0017554 & 0.0095685 & -0.0016502 & 0.0036821 & 0.45497 \end{bmatrix} \quad (\text{A5})$$

$$D_L \text{ Real} = \begin{bmatrix} 0.061416 & 0 & 0 & 0 & 0 & 0 \\ 0 & 0.7178 & 0 & 0 & 0 & 0 \\ 0 & 0 & -0.33542 & 0 & 0 & 0 \\ 0 & 0 & 0 & -2.7048 & 0 & 0 \\ 0 & 0 & 0 & 0 & -12.314 & 0 \\ 0 & 0 & 0 & 0 & 0 & 0.4557 \end{bmatrix} \quad (\text{A6})$$

$$D_Q \text{ SysID} = \begin{bmatrix} 62.567 & -0.22927 & -0.0075429 & 0.12322 & 0.053898 & -0.010741 \\ 0.18958 & 94.501 & 0.35236 & 0.40868 & -1.1611 & -0.0076908 \\ 0.20154 & -0.22744 & 227.17 & 0.21638 & 0.85851 & -0.017646 \\ -0.58393 & -0.095264 & -1.185 & 111.87 & 1.9665 & -0.0013486 \\ -0.41935 & 0.080463 & -0.83389 & 0.27354 & 387.31 & -0.0036605 \\ -0.47784 & -0.074815 & -0.97334 & 0.052337 & -0.10506 & 94.217 \end{bmatrix} \quad (\text{A7})$$

$$D_Q \text{ Real} = \begin{bmatrix} 62.543 & 0 & 0 & 0 & 0 & 0 \\ 0 & 94.51 & 0 & 0 & 0 & 0 \\ 0 & 0 & 226.83 & 0 & 0 & 0 \\ 0 & 0 & 0 & 111.88 & 0 & 0 \\ 0 & 0 & 0 & 0 & 386.77 & 0 \\ 0 & 0 & 0 & 0 & 0 & 94.219 \end{bmatrix} \quad (\text{A8})$$

$$M_{\text{SysID}} = \begin{bmatrix} 3352.2 & -9.5983 & -70.318 & 1.6161 & -29.045 & -0.23593 \\ 10.131 & 3794 & 14.944 & -165.28 & -7.2984 & -16.693 \\ -60.389 & -9.6142 & 10126 & 2.5499 & 66.962 & -0.435 \\ -31.044 & -203.06 & -51.351 & 1087.7 & 13.327 & -171.39 \\ -49.693 & 2.5612 & 111.87 & 3.5186 & 2437.4 & -0.44325 \\ -25.298 & -22.089 & -42.812 & -170.51 & -0.70015 & 691.78 \end{bmatrix} \quad (\text{A9})$$

$$M + M_A \text{ Real} = \begin{bmatrix} 3350.9 & 0 & -69.74 & 0 & -29.37 & 0 \\ 0 & 3795.3 & 0 & -169.3 & 0 & -16.02 \\ -71.01 & 0 & 10111 & 0 & 61.56 & 0 \\ 0 & -198.7 & 0 & 1087.6 & 1 & -171.39 \\ -27.45 & 0 & 148.2 & 1 & 2434 & 0 \\ 0 & -19.36 & 0 & -171.14 & 0 & 691.9 \end{bmatrix} \quad (\text{A10})$$

Appendix D: Additional Result from System Identification, Simulation C (HIL)

$$M_{SysID} = \begin{bmatrix} 753.13 & -0.22302 & 2.7704 & -0.77488 & 55.385 & -0.16991 \\ -0.0070344 & 762.01 & 0.0029101 & -55.2 & -0.0013956 & 5.993 \\ -0.0070282 & -0.014989 & 785.98 & 0.0090292 & -0.0052505 & 0.0011768 \\ -0.15519 & -55.392 & 1.1971 & 163.58 & -0.016551 & -0.063149 \\ 55.184 & 0.036388 & 0.042707 & 0.0019989 & 162.62 & 0.0022245 \\ -0.10451 & 5.9785 & 0.47612 & -0.35933 & -0.021643 & 107.34 \end{bmatrix} \quad (A11)$$

$$M + M_{A Real} = \begin{bmatrix} 753 & 0 & 0 & 0 & 55.2 & 0 \\ 0 & 762 & 0 & -55.2 & 0 & 0 \\ 0 & 0 & 786 & 0 & 0 & 0 \\ 0 & -55.2 & 0 & 163.8 & 0 & 0 \\ 55.2 & 0 & 0 & 0 & 162.64 & 0 \\ 0 & 0 & 0 & 0 & 0 & 107.31 \end{bmatrix} \quad (A12)$$

$$D_L SysID = \begin{bmatrix} 28.275 & -0.72149 & 14.421 & -1.1162 & 0.36356 & 2.0394 \\ 0.0084246 & 40.815 & -0.061632 & -0.061007 & 0.011452 & 0.17328 \\ 0.0085587 & 0.049732 & 254.03 & -0.098716 & 0.074358 & -0.023671 \\ -0.26764 & 0.3951 & 8.4689 & 34.039 & -0.19079 & 0.21771 \\ 0.017334 & -0.077592 & 0.040454 & -0.028473 & 59.018 & 0.092465 \\ 0.076789 & -0.024082 & 1.0985 & 0.55797 & -0.39982 & 45.067 \end{bmatrix} \quad (A13)$$

$$D_L Real = \begin{bmatrix} 29 & 0 & 0 & 0 & 0 & 0 \\ 0 & 41 & 0 & 0 & 0 & 0 \\ 0 & 0 & 254 & 0 & 0 & 0 \\ 0 & 0 & 0 & 34 & 0 & 0 \\ 0 & 0 & 0 & 0 & 59 & 0 \\ 0 & 0 & 0 & 0 & 0 & 45 \end{bmatrix} \quad (A14)$$

$$D_Q SysID = \begin{bmatrix} 311.33 & 1.7644 & -507.38 & 13.875 & 3.793 & -12.479 \\ -0.034523 & 613.07 & 6.2339 & 0.41142 & 0.067419 & -1.0803 \\ -0.059579 & -0.24803 & 633.83 & 0.81673 & -0.75173 & 0.18324 \\ 9.434 & -3.6464 & -315.59 & 81.723 & 4.234 & -1.2992 \\ -0.032039 & 15.295 & -1.4377 & 1.1797 & 147.94 & -0.59641 \\ -0.10974 & 0.14275 & -46.541 & -3.7681 & 3.152 & 99.644 \end{bmatrix} \quad (A15)$$

$$D_Q Real = \begin{bmatrix} 292 & 0 & 0 & 0 & 0 & 0 \\ 0 & 584 & 0 & 0 & 0 & 0 \\ 0 & 0 & 635 & 0 & 0 & 0 \\ 0 & 0 & 0 & 84 & 0 & 0 \\ 0 & 0 & 0 & 0 & 148 & 0 \\ 0 & 0 & 0 & 0 & 0 & 100 \end{bmatrix} \quad (A16)$$

Appendix E: Illustration of effect of magnetometer calibration error

Figure A1 presents a simple sketch showing how the effect of a heading error from the magnetometer calibration will affect the along track and cross track error.

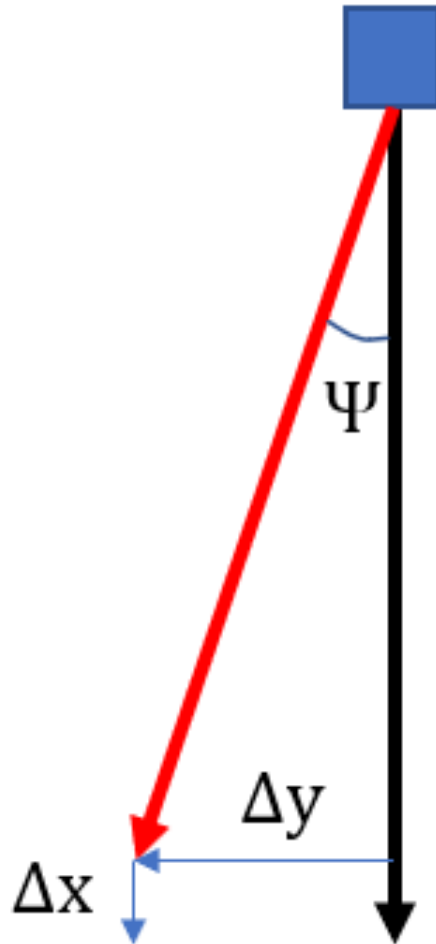


Figure A3: Illustration of the effect of a small heading angle with respect to cross track error Δy and alongtrack error Δx

Appendix F: Damping for ROV Minerva

The damping matrices found for ROV Minerva from [11]

$$D_L = \begin{bmatrix} 29 & 0 & 0 & 0 & 0 & 0 \\ 0 & 41 & 0 & 0 & 0 & 0 \\ 0 & 0 & 254 & 0 & 0 & 0 \\ 0 & 0 & 0 & 34 & 0 & 0 \\ 0 & 0 & 0 & 0 & 59 & 0 \\ 0 & 0 & 0 & 0 & 0 & 45 \end{bmatrix} \quad (\text{A17})$$

$$D_Q = \begin{bmatrix} 292 & 0 & 0 & 0 & 0 & 0 \\ 0 & 584 & 0 & 0 & 0 & 0 \\ 0 & 0 & 635 & 0 & 0 & 0 \\ 0 & 0 & 0 & 84 & 0 & 0 \\ 0 & 0 & 0 & 0 & 148 & 0 \\ 0 & 0 & 0 & 0 & 0 & 100 \end{bmatrix} \quad (\text{A18})$$

Appendix G: Additional plots from the Experimental test

Figure A4 presents a plot of the forces measured by the two sensors during the test of the yaw motion of the model of the ROV. A substantial level of noise is observed in the experiment.

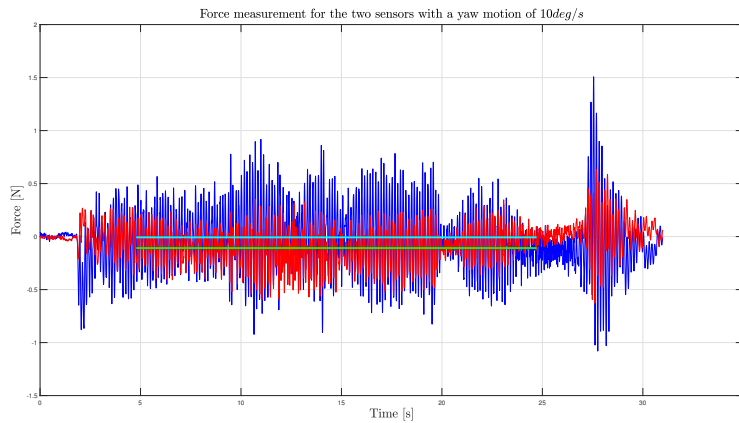


Figure A4: Figure of the sensor measurements during yaw motion of the model of the ROV. The figure shows substantial level of noise, compared to the magnitude of the average value of the force.

Appendix F: System identification code

The system identification program reads an "Input.mat" file, containing relevant constants and parameters, and a "Data.mat" containing the forces, positions, velocities and accelerations in the simulation. This program uses functions defined in the Marine systems simulator toolbox.

```

1 %-----
2 %                               SystemIdentification.m
3 %-----
4 % This program reads an inputmatrix containing known data for the program,
5 % and a file containing the data that will be used in the system
6 % identification program. The program calculate the system parameter for an
7 % underwater vehicle, on the basis of the motion and forces acting on the
8 % vessel.
9 %-----
10 % Written by : Erik Bjrklund Holven
11 % Date 10.05.2018
12 %-----
13 %% Load Data
14 load('Input.mat')           % Reads the input file, containg known
15                             % costants and parameters.
16 load('Data.mat')           % Load data
17
18 %% Account for nonlinear terms
19
20 % The folowing code calculate the restoring force, and the rigid body and
21 % added mass Coriolis and centripetal force. This is done on the assumed
22 % mass matrix M and added mass matix Ma
23 for i =1:length(time(1:end-100))
24     CA=m2c(Ma,nu(i,:))';
25     C_RB=m2c(M,nu(i,:))';
26
27
28
29 Ca(i,:)=(CA+C_RB)*nu(i,:);
30
31 phi=eta(i,4);
32 theta=eta(i,5);
33 psi=eta(i,6);
34
35 sth = sin(theta); cth = cos(theta);
36 sph = sin(phi);   cphi = cos(phi);
37
38 G(i,:) = [(W-B)*sth;
39           -(W-B)*cth*sphi;
40           -(W-B)*cth*cphi;
41           -(r_g(2)*W-r_b(2)*B)*cth*cphi + (r_g(3)*W-r_b(3)*B)*cth*sphi;
42           (r_g(3)*W-r_b(3)*B)*sth + (r_g(1)*W-r_b(1)*B)*cth*cphi;
43           -(r_g(1)*W-r_b(1)*B)*cth*sphi + (r_g(2)*W-r_b(2)*B)*sth];
44
45 end
46
47
48 %% Define Matrices
49 % The measurement vector Y and input vecotr X is defined
50 Y=nu_d(1:end-100,:)+(M_i*(Ca)')'+(M_i*G)';
51
52 X=[f(1:end-100,:) nu(1:end-100,:) nu(1:end-100,:).*abs(nu(1:end-100,:))];
53
54 %% Calculate System parameters
55 % The system parameters are found by applying least square method.
56 Theta=inv(X'*X)*X'*Y;
57
58 ThetaM=Theta(1:6,:);
59 M=inv(ThetaM)';           % Mass matrix
60
61 ThetaDl=Theta(7:12,:);
62 Dl=-M.calc*ThetaDl';     % Linear Damping matrix
63
64 ThetaDq=Theta(13:18,:);
65 Dq=-M.calc*ThetaDq';     % Quadratic Damping matrix

```